

1 **Air pollution trends measured from Terra:**

2 **CO and AOD over industrial, fire-prone, and background regions**

3 Buchholz, Rebecca R.*¹, Helen M. Worden¹, Mijeong Park¹, Gene Francis¹, Merritt N. Deeter¹,
4 David P. Edwards¹, Louisa K. Emmons¹, Benjamin Gaubert¹, John Gille¹, Sara Martínez-Alonso¹,
5 Wenfu Tang^{1,2}, Rajesh Kumar³, James R. Drummond⁴, Cathy Clerbaux^{5,6}, Maya George⁵, Pierre-
6 François Coheur⁶, Daniel Hurtmans⁶, Kevin W. Bowman^{7,8}, Ming Luo⁷, Vivienne H. Payne⁷, John
7 R Worden⁷, Mian Chin⁹, Robert C Levy⁹, Juying Warner¹⁰, Zigang Wei¹¹, Susan S Kulawik¹².

8
9 1. Atmospheric Chemistry Observations & Modeling Laboratory, National Center for
10 Atmospheric Research, Boulder, CO, USA.

11 2. Advanced Study Program, National Center for Atmospheric Research, Boulder, CO, USA.

12 3. Research Applications Laboratory, National Center for Atmospheric Research, Boulder, CO,
13 USA.

14 4. University of Toronto, Canada and Dalhousie University, Canada.

15 5. LATMOS/IPSL, Sorbonne Université, UVSQ, CNRS, Boite 102, 4 place Jussieu, 75252 Paris
16 cedex 05, France.

17 6. Université libre de Bruxelles (ULB), Service de Chimie Quantique et Photophysique,
18 Atmospheric Spectroscopy, Brussels, Belgium.

19 7. NASA Jet Propulsion Laboratory (JPL), 4800 Oak Grove Drive, MS 233-208j, Pasadena, CA
20 91109, USA.

21 8. Joint Institute for Regional Earth System Science and Engineering (JIFRESSE), University of
22 California, Los Angeles, USA.

23 9. NASA/Goddard Space Flight Center (GSFC), Greenbelt MD 20771, USA.

24 10. Dept. of Atmospheric & Oceanic Science, University of Maryland, College Park, MD 20742,
25 USA

26 11. IMMSG, Inc. at NOAA/NESDIS Center for Satellite Applications and Research (STAR),
27 College Park, MD 20740, USA

28 12. NASA Ames Research Center, Moffett Field, CA, 94035, USA

29

30 * Corresponding author: Rebecca Buchholz, buchholz@ucar.edu

31

32

33

34 **Research Highlights**

35 1. The global decreasing trend in CO has shown a recent slowdown.

36 2. Fire emissions in NH boreal regions counteract decreasing CO in late summer.

37 3. AOD helps interpret CO trends and variability.

38 4. Trends in four industrial regions show impact from varying air quality controls.

39

40 **Keywords**

41 Carbon monoxide; AOD; NASA/Terra satellite; trend; interannual variability

42 **Abstract**

43 Following past studies to quantify decadal trends in global carbon monoxide (CO) using satellite
44 observations, we update estimates and find a CO trend in column amounts of about -0.50 % per
45 year between 2002 to 2018, which is a deceleration compared to analyses performed on shorter
46 records that found -1 % per year. Aerosols are co-emitted with CO from both fires and
47 anthropogenic sources but with a shorter lifetime than CO. A combined trend analysis of CO and
48 aerosol optical depth (AOD) measurements from space helps to diagnose the drivers of regional
49 differences in the CO trend. We use the long-term records of CO from the Measurements of
50 Pollution in the Troposphere (MOPITT) and AOD from the Moderate Resolution Imaging
51 Spectroradiometer (MODIS) instrument. Other satellite instruments measuring CO in the thermal
52 infrared, AIRS, TES, IASI, and CrIS, show consistent hemispheric CO variability and
53 corroborate results from the trend analysis performed with MOPITT CO. Trends are examined
54 by hemisphere and in regions for 2002 to 2018, with uncertainties quantified. The CO and AOD
55 records are split into two sub-periods (2002 to 2010 and 2010 to 2018) in order to assess trend
56 changes over the 16 years. We focus on four major population centers: Northeast China, North
57 India, Europe, and Eastern USA, as well as fire-prone regions in both hemispheres. In general,
58 CO declines faster in the first half of the record compared to the second half, while AOD trends
59 show more variability across regions. We find evidence of the atmospheric impact of air quality
60 management policies. The large decline in CO found over Northeast China is initially associated
61 with an improvement in combustion efficiency, with subsequent additional air quality
62 improvements from 2010 onwards. Industrial regions with minimal emission control measures
63 such as North India become more globally relevant as the global CO trend weakens. We also
64 examine the CO trends in monthly percentile values to understand seasonal implications and find
65 that local changes in biomass burning are sufficiently strong to counteract the global downward

66 trend in atmospheric CO, particularly in late summer.

67 **1. Introduction**

68 Carbon monoxide (CO) is an atmospheric tracer for incomplete combustion, with major primary
69 sources from fossil fuels and fires and secondary production from hydrocarbon oxidation. CO is
70 destroyed through photochemical oxidation and is the dominant sink for the hydroxyl radical
71 (OH), thus impacting the self-cleansing capacity of the atmosphere (e.g., Lelieveld et al., 2016)
72 and methane (CH₄) lifetime (Prather, 2007; Gaubert et al., 2017a). CO is a short-lived climate
73 pollutant (SLCP) via its impact on carbon dioxide and ozone formation, and the methane budget,
74 with a radiative forcing of 0.23 Wm⁻² (Myhre et al, 2013) but whose impact is sensitive to
75 emission location (Bowman and Henze, 2012). The moderate CO lifetime of weeks to months
76 (e.g., Holloway, et al., 2000) allows for observation of distinct pollution plumes that gradually
77 succumb to atmospheric mixing, making it useful for studying both pollution sources and
78 atmospheric background loadings.

79

80 Tropospheric CO is accessible to remote sensing through its absorption of infrared radiation and
81 is observed by several satellite instruments. The longest running satellite instrument is the
82 Measurements Of Pollution In The Troposphere (MOPITT), aboard the NASA Terra satellite,
83 which has been observing CO since 2000 (Drummond et al., 2010). A consistent record
84 combined with recent algorithm improvements that minimize bias drift (Deeter et al., 2019)
85 ensure that MOPITT CO is suitable for atmospheric trend calculations.

86

87 Atmospheric CO has been decreasing globally for the last two decades, primarily due to
88 improvements in the combustion efficiency of anthropogenic sources, in addition to a global
89 decline in tropical fires (Novelli et al., 2003; Zeng et al., 2012; Worden et al., 2013; Schultz et al.

90 2015; Yin et al., 2015; Jiang et al., 2017; Gaubert et al., 2017; Andela et al., 2017; Tang et al.,
91 2019; Zheng et al., 2019). Recently, positive fire trends in Northern Hemisphere boreal regions
92 (e.g., for the USA, Dennison et al., 2014) may have counteracted the globally decreasing CO.
93 While trends in CO over fire-prone regions such as the Amazon and Southern Africa are more
94 difficult to determine due to the large source interannual variability (Strode and Pawson, 2013),
95 the CO record from MOPITT is potentially long enough to determine trends within this
96 variability. Inverse modeling studies to estimate CO emissions and trends using MOPITT
97 observations confirm reductions from fossil fuel combustion and tropical biomass burning (Jiang
98 et al., 2017, Zheng et al., 2018b, 2019). Strode et al. (2016) show that accurate emissions and
99 ozone chemistry are critical for model simulations that agree with observations and to interpret
100 trends in CO concentrations. Additionally, changing air quality policies, such as the 2010 China
101 Clean Air Policy (Zheng et al., 2018), can reduce or increase pollution emissions with impacts on
102 trends in atmospheric composition..

103

104 Atmospheric aerosols are also a marker of pollution processes. Fine particulate matter (diameter
105 $< 2.5 \mu\text{m}$; PM_{2.5}) has a significant negative impact on human health (e.g., McClure and Jaffe,
106 2018). Depending on type, aerosols can have either cooling or warming radiative forcing on
107 climate (e.g., Ramanathan and Carmichael, 2008). Through impacting photolysis rates, aerosols
108 can impact other pollutants such as ozone (Li et al., 2019). Previous studies have demonstrated
109 that satellite observations of atmospheric aerosol along with CO can provide additional
110 information in determining CO sources and understanding CO spatial and temporal variability
111 (e.g., Edwards et al., 2004). The most reliable satellite observations are of bulk aerosol total
112 column optical depth (AOD), and these are also available on Terra from the Moderate Resolution
113 Imaging Spectroradiometer (MODIS) instrument. Of particular interest here are the organic

114 carbon and black carbon aerosols that are directly emitted along with CO during the incomplete
115 combustion of fossil fuels and biomass (e.g., Edwards et al., 2004; Arellano et al., 2010).
116 However, distinguishing carbonaceous aerosol from other different aerosol types that contribute
117 to the AOD, and especially the component from fine mode aerosol, is challenging. Aerosols are
118 also formed from secondary reactions of pollutant precursor gases, and these may or may not
119 originate from the same combustion sources as CO. For example, sulfate aerosol results from the
120 oxidation of sulfur dioxide (SO₂), although the SO₂ emissions are not necessarily associated with
121 CO sources. (e.g., Unger et al., 2006). Spatial correlation of MODIS AOD with short-lived
122 species SO₂, nitrogen dioxide (NO₂) and formaldehyde has been used to suggest dominant
123 aerosol types for different global regions (Veefkind et al., 2011).

124

125 The shorter lifetime of aerosols, ~ 4 to 12 days (e.g., Kanakidou et al., 2005) means that they are
126 not observed as far away from sources as CO, so AOD trends are more indicative of local and
127 regional behavior in air pollution. The economically developing regions of the Asian landmass
128 and surrounding oceanic regions are reported to show increasing AOD from satellite-based
129 measurements using MODIS and Multi-angle Imaging SpectroRadiometer (MISR) AOD,
130 whereas North America, South America, and Europe show decreasing AOD (Mehta et al. 2016).
131 Ground-based analysis also shows increases over India, for example, at a rate of 2.3% per year
132 between 1985 and 2012 and at 4% per year since 2000 (Krishna Moorthy et al., 2013). In the US,
133 air quality related to surface-measured aerosols (PM_{2.5}) has been improving, as shown by a
134 decreasing trend, except where there are fires in the northwest (McClure and Jaffe, 2018).

135

136 This paper presents the trends in CO measured from space between 2002 and 2018 and uses
137 satellite-measured AOD to help understand CO variability. We split the records into two time

138 periods to measure the trend temporal stability, as well as examine trends over different source
139 and outflow regions, and analyze monthly percentile values. In Section 2 we present the CO and
140 AOD satellite-based measurements and describe the trend analysis methodology. Section 3
141 shows the CO and AOD records across different spatial and temporal scales, including regional
142 trends (Section 3.4). Section 4 discusses potential impacts on atmospheric trends by investigating
143 the co-variation of CO and AOD, as well as monthly CO percentile data. Conclusions are
144 presented in Section 5.

145

146 **2. Methods**

147 **2.1 Long-term CO and AOD measured from space**

148 The NASA/Terra satellite, launched in December 1999, carries two key instruments for the work
149 of this paper, MOPITT and MODIS. Terra follows a sun-synchronous orbit with equator crossing
150 times of $\sim 10:30$ local solar time (LST).

151

152 **2.1.1 MOPITT CO**

153 MOPITT is a nadir-viewing instrument that began measuring CO in 2000 and provides global
154 coverage about every three days. The cross-track scanning angle is ± 26 degrees to yield a swath
155 width of ~ 640 km. Pixel resolution is ~ 22 km \times 22 km at nadir. MOPITT uses gas correlation
156 spectrometry to complete broadband measurements in the thermal infrared (TIR) near 2140 cm^{-1}
157 and the near infrared (NIR) near 4275 cm^{-1} (Drummond et al., 2010). The MOPITT retrieval
158 algorithm is described in detail elsewhere (Deeter et al., 2019; Worden et al., 2013). Briefly, an
159 optimal estimation algorithm is applied to upwelling radiances that have gone through CO filled

160 gas cells of varying lengths to retrieve CO profiles of volume mixing ratio (VMR) on 10 vertical
161 layers, which are integrated to provide reported column amounts. The recent version 8 (V8)
162 algorithm includes: updates to the N₂ and H₂O spectroscopic data; accounting for temporal bias
163 drift and water vapor in the radiance bias correction; and updating to MODIS cloud Collection
164 version 6.1 to determine clear conditions. Validation covers a range of locations and shows
165 minimal bias drift for column amounts (Buchholz et al. 2017; Deeter et al., 2019). Improvements
166 in retrieval stability for the V8 daytime retrievals result in a negligible drift of $-0.015 \pm 0.061\%$
167 per year relative to NOAA airborne flask-sampling for CO total column over the MOPITT
168 mission (Deeter et al., 2019).

169 While including NIR channel information in the retrievals enhances MOPITT sensitivity to CO
170 in the lower troposphere, we use the TIR-only product in order to compare with other TIR
171 instruments (AIRS, TES, IASI, CrIS, introduced below). We use V8, TIR, daytime retrievals
172 over land and/or ocean scenes, depending on the region of interest. Level-2 total column CO
173 retrievals are used for regional trend analysis and monthly statistics (doi:
174 [10.5067/TERRA/MOPITT/MOP02T_L2.008](https://doi.org/10.5067/TERRA/MOPITT/MOP02T_L2.008)), while Level-3 monthly averaged total column CO
175 is used for the global gridded trend and zonal average analyses (doi:
176 [10.5067/TERRA/MOPITT/MOP03TM_L3.008](https://doi.org/10.5067/TERRA/MOPITT/MOP03TM_L3.008)). We filter Level-2 retrievals in the same way as
177 Level-3, that is: anomaly diagnostics all must be false to remove negative Averaging Kernel
178 elements and thermal anomalies; signal-to-noise in the 5A channel must be greater than 1000;
179 and pixel 3 is removed because of the large noise variability (Deeter et al., 2015). Filtering in this
180 way reduces inter-pixel differences (Hedelius et al., 2019). Data from 2002 onwards are used for
181 trend analysis to avoid discontinuities with the early 2000-2001 data taken before the MOPITT
182 cooler failure and instrumental reconfiguration that occurred in 2001 (Deeter et al., 2004).

183

184 2.1.2 MODIS AOD

185 As a passive imaging radiometer, MODIS measures reflected solar and thermal radiation in 36
186 bands with a 2330 km wide viewing swath, achieving near global coverage each day. At nadir
187 view, spatial resolution is 1 km or finer, depending on band. The calibration has been updated
188 over time, mitigating an observed drift in radiance and reflectance due to sensor degradation.

189 To derive aerosol, the observed spectral reflectances are inverted to AOD values from look-up-
190 tables that have been created with radiative transfer code that include different assumptions about
191 surface properties and aerosol types. The DT algorithm (Levy et al., 2013) retrieves aerosol over
192 open ocean and dark vegetated land surfaces while the DB retrieval algorithm adds retrievals
193 over bright surfaces (Hsu et al., 2013). Both sets of algorithms report AOD at 0.55 m along with
194 quality assurance. Based upon selection of retrievals that pass recommended quality assurance
195 (QA=3, see Sayer et al., 2014), the merged Dark Target / Deep Blue (DTDB) product (Levy et al.,
196 2013; Gupta et al., 2020), yields a single AOD value (at 10 km spatial resolution) in non-
197 cloudy, non-ice/snow scenes. Aggregations of such ‘Level 2’ products onto daily and monthly
198 1°x1° grids lead to ‘Level 3’ products. MODIS Collection 6.1 (C6.1) represents a consistent
199 reprocessing of all MODIS products, including original geolocation, calibration, aerosol
200 retrieval, and Level 3 aggregation.

201 In this work, we have used the C6.1 monthly aggregations from MODIS-Terra known as
202 MOD08_M3 (https://dx.doi.org/10.5067/MODIS/MOD08_M3.061, Platnick et al., 2017). We
203 use C6.1 because the previous Collection 6 (C6) showed some artifact trends (Levy et al., 2018)
204 when compared to MODIS on Aqua (King et al., 2013). Since the calibration has been made
205 consistent, C6.1 appears to be largely free of artificial drifts, which we have confirmed via
206 comparisons with MODIS trends on Aqua (Supplementary Figure C2). Wei et al., (2019a) also

207 found C6.1 products were improved relative to C6. Wei et al., (2019b) found MODIS C6.1
 208 performed best at capturing temporal variations and was closest to ground-based observations.

209 2.2 Other nadir-viewing, TIR satellite CO measurements

210 To assess the consistency of the hemispheric temporal variability of CO in Section 3.3, we
 211 compare data from a number of different nadir-viewing satellite instruments that make
 212 measurements in the TIR band of CO. All these satellites have sun-synchronous orbits and,
 213 besides AIRS, use optimal estimation approaches to retrieve CO columns from measured
 214 radiances. Northern Hemisphere (NH) and Southern Hemisphere (SH) monthly averages are
 215 collated from each instrument. A summary of instrument specific details are given in Table 1.

216

217 Table 1: Data selection criteria and specifications by instrument.

	MOPITT	AIRS	TES	IASI-A and IASI-B	CrIS
Instrument type	Gas filter correlation radiometer (GFCR)	Grating spectrometer	Fourier Transform Spectrometer (FTS)	FTS	FTS
Spectral range and resolution for CO	2140-2192 cm^{-1} (0.04 cm^{-1} effective)	2170-2200 cm^{-1} ($\sim 1.8 \text{ cm}^{-1}$)	2086.06 -2176.66 cm^{-1} (0.1 cm^{-1} apodized)	2143–2181.25 cm^{-1} (0.5 cm^{-1} apodized)	2185.25-2200 cm^{-1} unapodized (0.625 cm^{-1})
Data version	V8T (TIR-only)	V006	V007 Lite	FORLI 20151001	MUSES
Cloud screening	Clear sky conditions from MODIS Collection 6.1 and MOPITT Signal	Cloud-cleared radiances	Eff. cloud OD <0.4	< 25% clouds in pixel	Cloud effective optical depth < 0.1
Data quality	5A SNR > 1000; Remove Pixel #3; Retrieval Anomaly Diagnostics OK	QF = 0	Master QF = 1 DFS > 0.9	SQF=0; COTC<20x10 ¹⁸ molec./cm ² ; RMS<=2.7e-9 W/(cm ² sr cm ⁻¹); -0.15e-9<=bias<=0.25e-9 W/ (cm ² sr cm ⁻¹)	Master QF=1
Ground resolution	22x22 km	50 km x 50 km	8x5 km	12 km diameter	14 km radius
Daytime Global	~ 3 days	Daily	Sparse sampling; 16 day orbit track	Daily	Daily (sub-sampled in this

coverage			repeat		study)
Column uncertainty for single obs.	5–6 %	10 %	6–7 %	A & B: 5–7 %	6–7 % (??)
Time range used	03/2000–12/2018	09/2002–12/2018	01/2005–12/2009	A: 01/2008–12/2018 B: 01/2013–12/2018	11/2015–3/2019
Instr. operation gaps	8–9/2009	20160924	4–6/2005 1–3/2010	none	May 2019
Avg. ret. per month	NH: 684520 SH: 627344	NH: 1419165 SH: 1359028	NH: 6249 SH: 3672	NH: A-2216361, B-2417436 SH: A-1905719, B-1976112	NH: 13071 SH: 12293
Data source	https://doi.org/10.5067/TERRA/MOPITT/MOP02T_L2.008	https://doi.org/10.5067/Aqua/AIRS/DATA202	NASA Langley Atmospheric Science Data Center. https://doi.org/10.5067/AURA/TES/TL2COLN.007	A: https://doi.org/10.2532/6/16 B: https://doi.org/10.2532/6/17	JPL MUSES team (tes.jpl.nasa.gov)

218

219 2.2.1 AIRS

220 The Atmospheric Infrared Sounder (AIRS), on board NASA/Aqua was launched in 2002 and
221 crosses the equator at ~13:15 LST (Aumann et al., 2003). Ground-pixel size is nominally 13.5
222 km × 13.5 km, but is degraded to 45 km × 45 km as a trade-off to increase global coverage using
223 a cloud-clearing algorithm (Susskind et al., 2003). The 1650 km AIRS swath provides near
224 global coverage twice daily. Radiance spectra from the AIRS grating spectrometer are used to
225 determine cloud and surface properties along with vertical profiles of atmospheric trace gases
226 (including CO at 4.6 μm) and temperature. Previous comparisons of AIRS and MOPITT CO
227 showed good agreement in horizontal spatial variability, but found AIRS CO to be higher than
228 MOPITT (V3) (Warner et al., 2007). However, the comparison in Worden et al. (2013), found
229 better agreement using more recent versions of the retrieval algorithms for both instruments. We
230 use the Level 2 V006 AIRS retrievals here, (AIRS2RET, AIRS Science Team, 2013), which has
231 50 km x 50 km spatial resolution. The AIRS2RET Level 2 product was created Level-2 using

232 AIRS IR-Only retrievals. NH and SH monthly average values were computed for daytime
233 retrievals (SZA<90).

234

235 2.2.2 IASI

236 There are three Infrared Atmospheric Sounding Interferometer (IASI) TIR Fourier Transform
237 Spectrometer (FTS) instruments currently in orbit: IASI-A, B, and C onboard the Eumetsat
238 satellites Metop-A, B and C, launched in 2006, 2012, and 2018, respectively. They fly in the
239 same orbit, crossing the equator at ~9:30 a.m. LST. IASI observations comprise 4 pixels that
240 each have a 12 km ground resolution at nadir. A 2200 km swath provides global coverage twice
241 daily (Clerbaux et al., 2009). CO profiles are retrieved with the Fast Optimal Retrievals on
242 Layers for IASI (FORLI, version 20151001) algorithm (Hurtmans et al., 2012), using invariant a
243 priori information. IASI CO has been validated against ground-based observations
244 (Kerzenmacher et al., 2012), aircraft data (Pommier et al., 2010, Klonecki et al., 2012) and other
245 satellite measurements (George et al., 2009). Comparison between MOPITT and IASI CO
246 records found that, while a priori was the dominant source of between-instrument bias, timing
247 and vertical sensitivity differences also contribute to CO differences (George et al., 2015). While
248 the IASI-A record is long enough to determine trends, it is worth noting that this CO record is
249 not currently retrieved using homogeneous temperature, humidity and cloud information. This
250 causes a few discontinuities in the IASI-A CO record, which could affect the long-term trend and
251 it is therefore not suited for trend studies at this time. Different versions of these IASI auxiliary
252 parameters (distributed by Eumetsat) have been improved over time (from V5 to V6 in Sept.
253 2014, and from V6 to V6.1 in Sept. 2015). Reprocessing of these data with homogeneous
254 auxiliary data is in progress at Eumetsat but they are not yet available at the time of this analysis

255 (Oct. 2019). Despite this, IASI data are still useful for confirming the hemispheric CO
256 seasonality and interannual variability observed by the other satellites. NH and SH monthly
257 average values for daytime ($SZA < 80$), were computed after filtering for Super Quality Flag
258 (SQF)=0 (see https://iasi.aeris-data.fr/CO_readme/), CO total column $< 20 \times 10^{18}$ molecules/cm²,
259 Root Mean Square (RMS) $\leq 2.7 \times 10^{-9}$ W/(cm² sr cm⁻¹) and $-0.15 \times 10^{-9} \leq \text{bias} \leq 0.25 \times 10^{-9}$ W/(cm² sr cm⁻¹).

260

261 2.2.3 TES

262 The Tropospheric Emission Spectrometer (TES) was launched on the NASA/Aura satellite in
263 2004 and crosses the equator at 13:40 LST, 25 minutes after the NASA/Aqua satellite. TES
264 measures radiance spectra of Earth's surface and atmosphere, with relatively fine spectral
265 resolution (0.10 cm^{-1} at nadir, apodized) (Beer, 2006), and retrieves trace gases, temperature
266 (Bowman et al., 2006) as well as cloud top pressure and cloud optical depth (Kulawik et al.,
267 2006). TES CO profiles and total column amounts have been validated with respect to in situ
268 measurements (Luo et al., 2007, 2015).

269

270 For this study, we use V007 Level 2 data and select daytime retrievals filtered with master
271 quality flag = 1 (good) that accounts for variations in retrieval performance, e.g., residual
272 radiance mismatch, and the degrees of freedom for signal (DFS) ≥ 0.9 . The TES algorithm
273 retrieves on both clear and cloudy scenes, but for this work, only clear scenes are considered in
274 month averages. Cloud-free retrieval criteria are defined as an effective cloud optical depth
275 (OD) ≤ 0.4 . Prior to December 2005, the TES instrument was in a different configuration for CO
276 (Rinsland et al., 2006), resulting in a land bias for filtered data, especially over the fire-prone
277 regions of South America and Africa. After 2005, sampling footprints are nearly uniformly

278 distributed over land and ocean when filtered. Consequently, we use TES data after December
279 2005. Also, in order to conserve the instrument lifetime, from 2010 onwards routine sampling
280 was spatially limited. Therefore, TES data acquired after 2009 are not included in our analysis.

281

282 2.2.4 CrIS

283 The Cross-track Infrared Sounder (CrIS) was launched in October 2011 on the Suomi National
284 Polar-Orbiting Partnership (S-NPP) satellite (NOAA-19) with an equator-crossing time of
285 $\sim 13:30$ LST. The CrIS scan pattern consists of nine detectors (each called a Field of View: FOV)
286 in a 3×3 pattern (collectively named a Field of Regard: FOR). At nadir, each FOV diameter is
287 ~ 14 km. The CrIS cross-track scan consists of thirty Earth-view FORs, plus additional
288 calibration FORs. CrIS is a FTS operating in three spectral bands between 648 cm^{-1} and 2555 cm^{-1} ,
289 including the CO TIR R-branch above 2155 cm^{-1} . CrIS achieves daily coverage of over 95% of
290 Earth's surface. The full-spectral-resolution retrieval of CO (0.625 cm^{-1}) has been operational
291 since late 2015, with significant improvements in sensitivity to CO compared to the original 2.5
292 cm^{-1} resolution (Gambacorta et al., 2014). Here we use CrIS retrievals processed by the MUlti-
293 SpEctra, MUlti-SpEcies, MUlti-SEnsors (MUSES) algorithm (Fu et al., 2016), which performs
294 single pixel (FOV) retrievals, and has heritage in the TES algorithm (e.g., Worden et al, 2007;
295 Luo et al, 2013), using the same Kulawik et al. (2006) approach for retrievals of cloud.
296 Retrievals presented here use the NASA v2 L1B Full Spectral Resolution (FSR) radiances
297 (Revercomb and Strow, 2018), which are available from November 2015 onward. CO retrievals
298 from FSR radiances offer significant improvements in sensitivity compared to retrievals using
299 the nominal spectral resolution (NSR) radiances ($\delta = 2.5 \text{ cm}^{-1}$ in the CO region) (Gambacorta et
300 al., 2014).

301

302 In order to expedite analysis, sub-sampling of observations was tested to ensure that the NH and
303 SH CrIS monthly averages were insensitive to the sub-sampling employed (Appendix A1.2).
304 Like TES, the MUSES algorithm retrieves in all-sky conditions. Cloud-screening was performed,
305 using an effective cloud optical threshold of 0.1. While there are operational CrIS CO products
306 available for the FOR from NUCAPS (NOAA Unique Combined Atmospheric Processing
307 System, Gambacorta et al., 2013), we instead use the MUSES single pixel (FOV) retrievals to
308 take advantage of the full CrIS CO spatial resolution and error characterization derived from
309 optimal estimation.

310 **2.3 Analysis methodology**

311 In order to compare timeseries in total column CO retrievals from different satellite instruments,
312 we convert to column average VMR (X_{CO}) by dividing by the reported dry air column for each
313 retrieval. Trends are reported as relative trends (%) by dividing by the dataset mean value.
314 Relative (%) trends in X_{CO} are equivalent to relative trends in total column CO, but using X_{CO}
315 removes the dependence on surface topography that varies for the different instruments with
316 different horizontal footprints.

317

318 The first step in trend determination is to remove the seasonal variability, which can obscure any
319 linear trend. For the global map plots of column CO and AOD trends (Sect. 3.2), we remove
320 seasonal variations using a 12-month running average prior to computing the linear trend. The
321 endpoints are truncated, effectively removing the first and last 6 months for all the time series.
322 This determines our bounds for the long-term trend as July 2002 - June 2018. For hemispheric
323 and regional time series analysis (Sect. 3.3. and 3.4), we remove the seasonal variations in X_{CO}

324 and AOD by subtracting the dataset mean annual cycle with monthly resolution to produce an
 325 anomaly time series in monthly averages.

326

327 Trend analysis on deseasonalized data proceeds by calculating the slope of a line for the linear
 328 equation:

$$y = mt + b + \epsilon(t) \quad (1)$$

329 where y is the dependent variable (e.g. CO amounts), t is time in fractional years, m is the slope
 330 (or linear trend), b is a constant and $\epsilon(t)$ is the noise, or residual. Weighted Least Squares (WLS)
 331 linear regression, weighted by the monthly variance, is used to calculate hemispheric and
 332 regional trends by estimating the linear slope via equation 2:

$$m = \frac{\sum_{i=1}^n \frac{1}{\sigma_i^2} \sum_{i=1}^n \frac{t_i y_i}{\sigma_i^2} - \sum_{i=1}^n \frac{t_i}{\sigma_i^2} \sum_{i=1}^n \frac{y_i}{\sigma_i^2}}{\sum_{i=1}^n \frac{1}{\sigma_i^2} \sum_{i=1}^n \frac{t_i^2}{\sigma_i^2} - \left(\sum_{i=1}^n \frac{t_i}{\sigma_i^2} \right)^2} \quad (2)$$

333 for y_i with σ_i standard deviation associated with time t_i , where n is the total number of data
 334 points. Standard error in the slope is calculated two ways: using the WLS calculations or creating
 335 an estimate that compensates for first-order autocorrelation in the noise (Appendix A3,
 336 Weatherhead et al., 1998). The greater of the two error values is recorded as a conservative
 337 estimate of the standard error in the slope. A significant trend is defined as being outside one
 338 standard error.

339

340 Monthly statistics in MOPITT CO are determined by collecting all X_{CO} within a region (filtered
 341 as described in Section 2.1.1) for a particular month and year followed by calculations of the
 342 mean, standard deviation, median, 25th and 75th percentiles. The Theil-Sen method (Theil,

346 1950; Sen, 1968) is used to analyze the long-term trends in X_{CO} regional percentiles separated by
 347 month (Sect. 4.2). Theil-Sen analysis is a non-parametric trend estimation technique that
 348 calculates all the slopes between pairs of points and takes the median of these slopes (eq. 3):

$$m = \left(\frac{\widetilde{y_j - y_i}}{t_j - t_i} \right) \quad (3)$$

349 for all y_j, y_i dependent variable values associated with the t_j, t_i times, for $j > i$. Significance of a
 350 Theil-Sen trend is determined using the Mann-Kendall test for p values $< 0.05, 0.01$ and 0.001
 351 (Mann, 1954; Kendall, 1975). We show in Appendix B1 that Theil-Sen results for the whole time
 352 series are consistent with the WLS method. Note that because the lifetime of CO is ~ 2 months
 353 and consecutive values are a year apart the autocorrelation is not significant and is not
 354 considered for trends calculated by month (Appendix A3).

355

356 A full description of the uncertainty analysis on the X_{CO} trend calculations is provided in
 357 Appendix A. Systematic sampling uncertainty is approximated by performing trend analysis on a
 358 priori (Appendix A1.1) and random sampling uncertainty by using bootstrap analysis (Appendix
 359 A1.2). Systematic uncertainty from changes in instrument sensitivity over the MOPITT record is
 360 explored using averaging kernels applied to a reanalysis climatology (Appendix A2).

361 Autocorrelation is analyzed for each region (Appendix A3). We also assess the consistency
 362 between trend determination methods (Appendix B1) as well as the robustness of the trend to
 363 removing the influence of outliers such as the large El Niño fires in 2015 (Appendix B2).

364

365

366 **3. Results**

367 **3.1 Zonal average time series of CO and AOD**

368 We show the latitudinal and seasonal dependence of column CO and AOD using the zonal
369 average time record (Figures 1a and 1b). The annual cycle of CO (Supplementary Figure C3) is
370 determined by a combination of source seasonality and removal by reaction with OH.
371 Photochemically produced OH depends on incoming solar radiation, leading to lower reactivity
372 in winter and higher reactivity in summer. In the background atmosphere, the OH sink
373 dominates the seasonal behavior of CO. Consequently, the build-up of CO over the winter
374 months produces an early spring peak, and destruction during summer leads to a late summer
375 minimum. Since removal of aerosols is mainly by dry and wet deposition (e.g., Kanakidou, et al.,
376 2005), there is no corresponding winter accumulation, and AOD seasonality is determined
377 mainly by production processes. Production by photochemical oxidation again depends on OH
378 availability, and peaks in summer for secondary aerosol types such as sulfate aerosols (e.g.,
379 Edwards et al., 2004) and secondary organic aerosols (SOA) (e.g., Lack et al., 2004). Direct fire
380 emissions of carbonaceous aerosols follow the annual cycles of dry season burning.

381

382 Due to pollution sources, both CO and AOD show higher mean values in the Northern
383 Hemisphere (NH) compared to the Southern Hemisphere (SH). Peak CO at 30° to 50° N occurs
384 at higher latitudes than the peak AOD (15° to 25° N). Enhanced CO columns are mainly
385 influenced by fire and anthropogenic emissions, while AOD additionally experiences strong
386 contribution of dust at lower latitudes that combines with the anthropogenic and fire aerosol
387 sources. The lifetime of CO allows it to be transported to higher latitudes by dominant poleward
388 flow, while aerosols with shorter lifetimes produce AOD enhancements closer to source regions.

389 Peak NH AOD is shifted equatorward in this study when compared to Edwards et al. (2004),
390 which is a result of including the Deep Blue AOD retrieval over dust source regions, such as the
391 Sahara, Middle East, Gobi, Taklamakan and India deserts. This algorithm was not available in
392 the Edwards et al. (2004) study which used MODIS Collection 4. Additionally, Levy et al.
393 (2013) found that AOD in MODIS C6 is generally lower than Collection 5 for Europe and North
394 America, but higher over Eastern Asia.

395

396 The SH peak and interannual variability for both CO and AOD in the tropics are mainly driven
397 by biomass burning in South America, Africa, Maritime Southeast Asia (SEA) and Australia
398 (Edwards et al., 2004). The impact of CO and aerosol lifetime differences is also apparent as
399 evidenced by the smearing of fire enhanced CO poleward (Fig. 1a) compared to AOD (Fig. 1b).
400 The consistent feature of relatively large AOD at temperate southern latitudes (40° to 60° S, Fig.
401 1b) is due to maritime aerosols such as sea salt (e.g., Witek et al., 2016), ocean biogenics, or
402 transported smoke.

403

404 The anomaly plots show the percent anomaly relative to the monthly means (Fig. 1c and 1d). In
405 general, relative interannual variability for CO shows similar strength between hemispheres,
406 while for AOD, the SH interannual variability appears weaker than the NH (less saturated
407 colors). Several large anomalies are consistent between CO and AOD. For example, the 2003
408 high northern latitude enhancement is a response to the large boreal fires in Western Russia (e.g.,
409 Edwards et al., 2004); and the 2015 El Niño driven large Maritime SEA fire season emissions in
410 September and October (Huijnen et al., 2016; Field et al., 2016) had a widespread impact
411 producing the CO and AOD positive anomalies at the end of 2015 and the beginning of 2016.
412 These examples highlight the direct co-emission of CO and aerosol from fire events. In contrast,

413 AOD includes many anomalies that are absent in the CO record, for example, the AOD anomaly
 414 in 2018 at about 20° N that was mainly due to dust emissions over the Arabian peninsula,
 415 combined with exported dust from the Sahara (Voss and Evan, 2020).

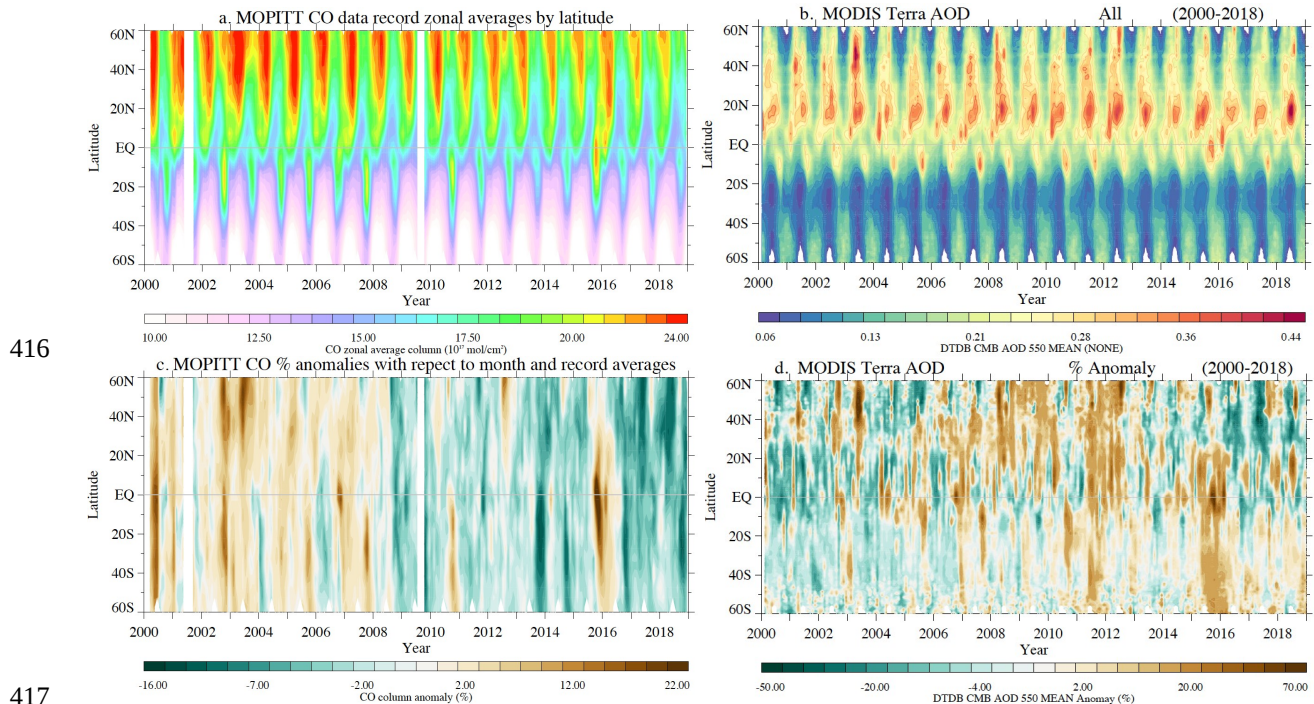


Fig 1. Zonal average plot of monthly average (a) MOPITT column CO and (b) MODIS AOD.

419 Percent anomalies in (c) MOPITT CO and (d) MODIS AOD. Percent anomalies are calculated
 420 relative to the climatological month averages within each 2° zonal average box. White stripes in
 421 panel a and c during 2001 and 2009 represent missing MOPITT data due to instrumental
 422 diagnostic operations. White pixels at NH and SH high latitudes represent missing data for both
 423 instruments due to polar night.

424

425 The large positive anomalies in Figures 1c and 1d illustrate the substantial interannual variability
 426 in both the CO and AOD records. However, we can also see that the background CO shows an
 427 overall global downward trend as observed by more widespread cool colors in later years
 428 compared to earlier years. In contrast, AOD shows a general upward trend in the SH while the

429 NH seems to increase between 2008 and 2012, followed by decrease. We investigate these trend
430 behaviors in more depth in the following sections.

431 **3.2 Spatial analysis of trends in CO and AOD**

432 Figures 2a and 2b show the 2000-2018 global average maps of CO and AOD, respectively.

433 Regions of high values for both constituents are apparent over Northeast China, North India and

434 Central Africa. Trends in CO and AOD from 2002-2018 are shown in Figures 2c and 2d, globally

435 gridded at $2^{\circ} \times 4^{\circ}$. The overall decline in CO coincides with the improvements in combustion

436 efficiency for anthropogenic sources (Zheng et al., 2018), as well as the decrease in global fire

437 emissions, e.g. from 1997 to 2009 as shown in the Global Fire Emissions Database, Version 3

438 (GFED3) inventory (van der Werf et al., 2010) and the negative trend in global burned area in

439 Andela et al. (2017) from 1998 to 2015. Since fire emissions account for about 33% of global

440 CO emissions (Yin et al., 2015), a trend in fires can have substantial effect on atmospheric CO.

441 AOD trends are more regionally variable and reflect changes in the different sources.

442

443 Burning regions around the South Atlantic show different trend results (Fig. 2c and 2d). South

444 America has seen a strong decrease in both CO and AOD over the whole record due to the long-

445 term decrease in burning there (Andela et al., 2017; Deeter et al., 2018). However, recent

446 increases in Amazon deforestation burning over the last few years may alter trends in that region,

447 especially for the recent decade. In contrast, southern Africa shows no trends in CO and AOD.

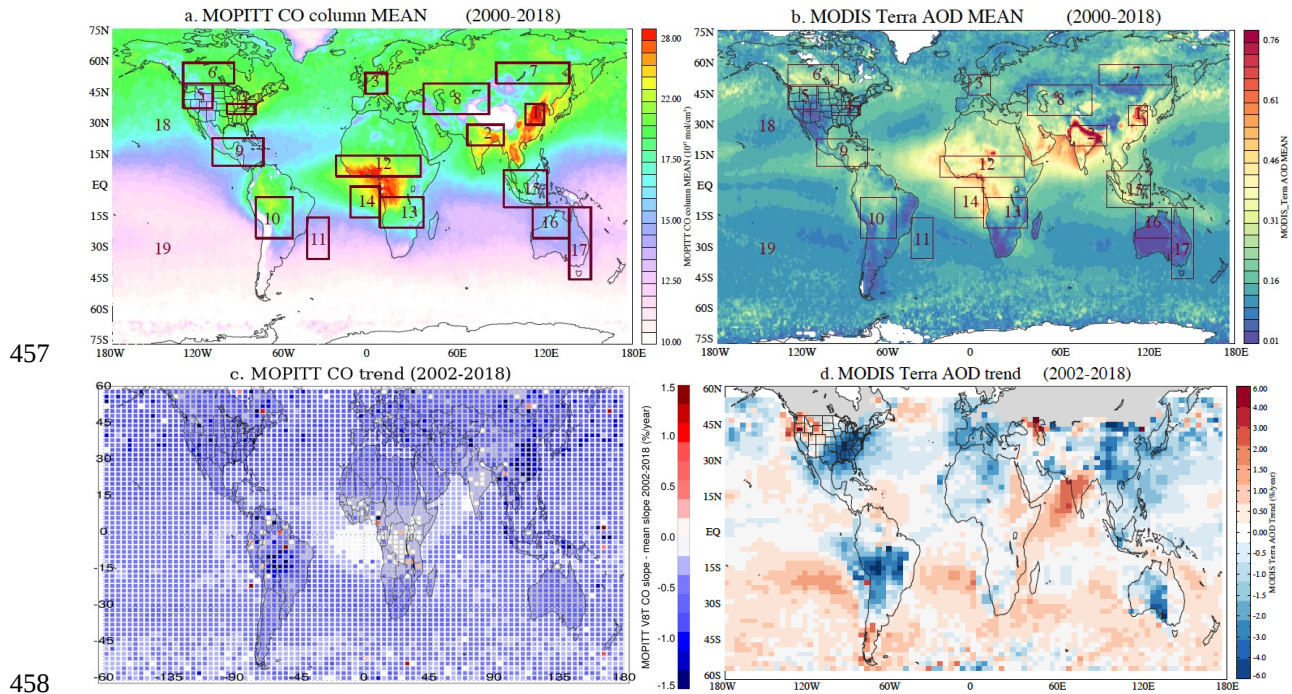
448 Increasing burning in this region (Andela et al., 2017) might be counteracting transported

449 decreasing trends. In addition, Zheng et al. (2019) find an increasing trend in anthropogenic

450 sources in Central Africa that could also counteract the global downward CO trend. The AOD

451 trend may be further confounded by dust and anthropogenic variability. In comparison, the

452 Pacific Northwest (PNW) has less interference from dust or anthropogenic aerosol sources and
 453 consequently sees a positive AOD trend due to climate driven changes in fire (McClure and
 454 Jaffe, 2018). The CO trend in the PNW is lower than the global average, but local behavior is
 455 combined with strong downward trends in transported CO from Asia. Therefore, CO is still
 456 decreasing in the PNW.

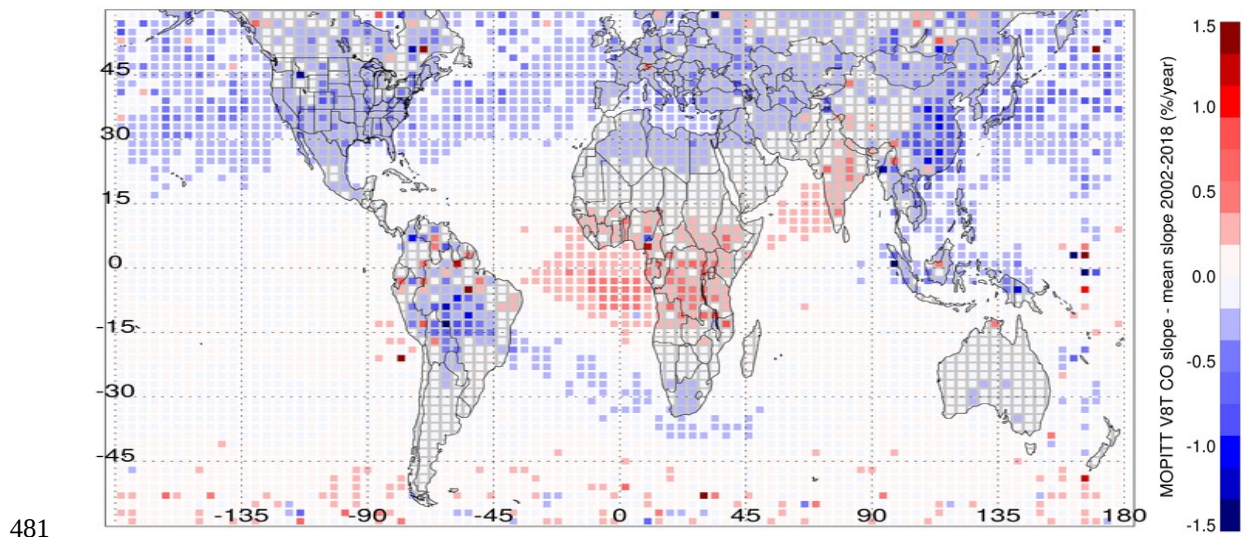


459 Fig 2: Global average (a) column CO and (b) AOD between 2000 and 2018. Boxes outline the
 460 sub-regions used for regional trend analysis, numbered 1 to 19, discussed in section 3.4. Trends
 461 in (c) CO from MOPITT and (d) AOD from MODIS between 2002 and 2018, gridded to $2^\circ \times 4^\circ$.

462

463 To help interpret regional CO trends, we calculate CO residual trends. The lifetime of CO (~ 2
 464 months) is such that a global mean trend can be detected in well-mixed background air. We find
 465 the global mean CO trend ($\pm 60^\circ$ latitude) between 2002 and 2018 to be $-0.50 (\pm 0.3) \%$ per year,
 466 which is a slow-down relative to the $\sim -1 \%$ per year trend between 2000 and 2011 found by
 467 Worden et al. (2013) using MOPITT V5 retrievals. This difference reflects an atmospheric

468 response because both MOPITT versions saw negligible drift in column amounts from TIR
 469 retrievals (Deeter et al., 2013, 2019). The slow-down potentially reflects diminishing returns
 470 from improvements in combustion efficiency and emission controls, as has been suggested by
 471 McDonald et al. (2013). In addition, emissions from economic production and transport have
 472 returned to pre-recession levels following the 2008-2009 global economic crisis (e.g., de Ruyter
 473 de Wildt, 2012). The residual trend in CO was calculated by subtracting the global mean trend
 474 from the total trend within 2° by 4° gridboxes. The result is a map of residual trends that enables
 475 interpretation of local behavior relative to the global mean trend (Fig. 3) and reveals regions that
 476 are decreasing faster than the global average (blue colors), and regions that are decreasing slower
 477 than the global average trend (red colors), suggesting increasing regional emissions that
 478 counteract the global trend. Light colors show where the trend is close to the global average. A
 479 global average trend for AOD is not very meaningful due to the shorter lifetime (~ 8 days) of
 480 aerosols.



481
 482 Fig 3: Residual trend in CO columns from MOPITT calculated relative to the global average
 483 trend (-0.5% per year, $\pm 60^\circ$) from 2002 to 2018.

484

485

486 The different response in the two Atlantic fire-prone regions (South America and
487 Central/Southern Africa) is immediately clear in the CO residual trend map. Residual trends from
488 these regions extend into their respective outflow paths over the Atlantic Ocean. Different
489 patterns are also clear for industrial regions. Northeast China experiences the most negative CO
490 trends globally, resulting from rapid improvements in combustion efficiency and a recent focus
491 on air quality control (Zheng et al., 2018a,b; Tang et al., 2019). However, AOD decreases in
492 Northeast China are weaker than in Eastern USA, reflecting the relatively new air quality
493 policies in China compared to a longer-term focus in USA. India, on the other hand, shows
494 strong increases in AOD and the CO residual trends are positive suggesting local pollution
495 sources counteract any transported or background decreases in CO.

496

497 In the following sections we examine regional trends in more detail, including calculations of
498 trend significance.

499 **3.3 Hemispheric CO record across different instruments**

500 Figure 4 shows the hemispheric monthly mean X_{CO} time series from all satellite instruments
501 (MOPITT, AIRS, TES, IASI and CrIS) available between January 2001 and December 2018.
502 Overall, X_{CO} magnitude, seasonal patterns, and interannual variability are consistent between
503 instruments. Some differences in X_{CO} values arise because we have not accounted for differences
504 in sampling coverage, horizontal resolution or vertical sensitivity between instruments.
505 Although column results are less sensitive than profile retrievals to differences in vertical
506 sensitivity, the different averaging kernels between instruments could give rise to slightly
507 different results when applied to the same atmospheric state (George et al., 2009; 2015).

508 Comparisons of MOPITT, AIRS, TES, and IASI were previously conducted by George et al.
509 (2009) and Warner et al. (2010), who found that biases are due to differences in spatial sampling,
510 instrument spectral resolution and retrieval methodology, including different a priori information.
511 Additionally, the number of TES observations is 2 orders of magnitude lower than the other
512 instruments, so we would expect the non-colocation of TES observations with other instrument
513 footprints to contribute to the CO differences. The SH high bias previously found when using
514 AIRS V5 (Warner et al., 2010, Worden et al., 2013) has been removed in the comparison using
515 updated retrievals from both instruments.

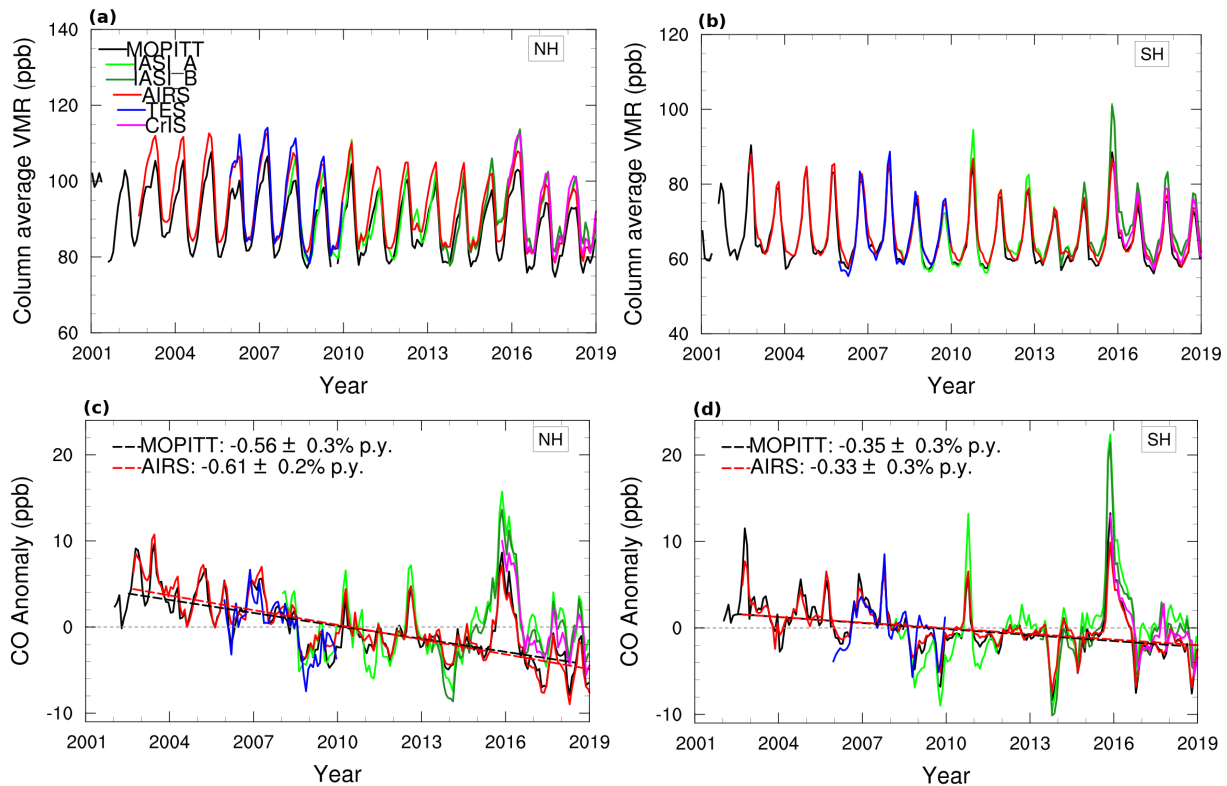
516

517 Figures 4c and 4d show the NH and SH anomaly records for all satellite instruments computed
518 by subtracting the respective instrument record climatological monthly means. Anomalies reflect
519 interannual variability due to changes in fire emissions that are in turn linked with climate
520 variability (Buchholz et al., 2018), such as the 2015 El Niño influenced fire emissions from
521 Maritime SEA (Huijnen et al., 2016) that impacted both hemispheres. There is also a relationship
522 of lower X_{CO} with lower anthropogenic emissions due to the global financial crisis starting in late
523 2008, particularly for the NH (e.g., de Ruyter de Wildt et al., 2012).

524

525 Trend values from linear fits (July 2002-June 2018) are shown for MOPITT and AIRS in Figs. 4c
526 and 4d, with standard errors. While IASI-A has a long enough record to determine trends, it
527 currently does not have a fully harmonized record across the whole time period and is not yet
528 suited for trend analysis (see discussion in Section 2.2.2). The instruments with shorter time
529 records, IASI-B, TES and CrIS, do not show significant trends. However, all instruments show
530 similar variability, lending confidence to the use of MOPITT and AIRS records for trend
531 determination. MOPITT and AIRS X_{CO} trends are consistent within $<1\sigma$. The SH trend is less

532 negative than the NH trend, and both hemispheres have a reduced trend compared to Worden et
 533 al. (2013). Although it does have some impact, we find that the large emissions in 2015 are not
 534 the main reason for the CO trend slow down (Appendix B2).



535

536

537 Fig 4: Multi-instrument time series of month average X_{CO} for (a) NH (0° to 60° N) and (b) SH

538 (60° S to 0°). Lower panels show the monthly anomalies relative to each dataset mean annual

539 cycle, for (c) NH and (d) SH. Weighted least squares trends on the anomalies are indicated with

540 standard error in percent per year for MOPITT and AIRS. The grey dashed line is the zero line

541 for reference.

542 3.4 Regional trends in CO and AOD

543 In addition to hemispheric trend analysis, we select a number of regions for more detailed

544 consideration (Fig 2a). Four industrial regions were chosen to align with Worden et al. (2013):

545 Northeast China, North India, Europe and Eastern United States. Other regions are selected

546 based on the residual trend patterns from Fig. 2, combined with the burned area trends in Andela
547 et al., 2017. Due to the shorter lifetime of aerosols, it was not relevant to calculate hemispheric
548 trends for AOD, so only regional trends are shown.

549

550 CO trends (in X_{CO}) and AOD trends, determined for the different sub-regions are shown in Table
551 2, for the full 16-year period (July 2002-June 2018), as well as for two 8-year sub-periods (1st
552 half: July 2002-June 2010 and 2nd half: July 2010-June 2018). CO trends in the first half of the
553 record are consistent with those found in Worden et al. (2013). Significant negative CO trends in
554 the 1st half of the record shift to slower, non-significant trends in the 2nd half. This leads to an
555 overall slowdown in the CO downward trends for the full time period in every region.

556 Exceptions are Southern Africa and South America, which show no significant CO trend for any
557 time period. This is consistent with Strode and Pawson (2013) who found more than 20 years of
558 data are necessary to find CO trends over highly variable regions. AOD is more regionally
559 variable and generally shows more positive AOD trends in the 1st half of the record compared to
560 the 2nd half.

561

562 Northeast China has the strongest negative CO trend across all time periods, at more than -1%
563 per year. AOD in China moves from a positive to negative trend between first and second halves
564 of the record, coinciding with the clean air policy implementation in 2010. The CO trend in India
565 is substantially lower than the other industrial regions and the full time period shows a positive
566 trend in AOD, reflecting the minimal emission controls in that region. While in the first half of
567 the record, both Europe and Eastern USA CO are decreasing at similar rates, in the second half,
568 the Eastern USA CO trend is stronger than in Europe. This may be due to stronger local focus on
569 air quality improvements in the USA than in Europe, as supported by the coinciding large

570 downward trend in Eastern USA AOD and the stronger reductions in USA anthropogenic CO
571 emissions since 2010 compared to Europe as found by Jiang et al. (2017). Additionally, Eastern
572 USA may be more influenced by CO transport from China than Europe, and consequently
573 reflects the negative trend in transported CO.

574

575

576 Table 2: Summary of Weighted Least Square (WLS, Eq. 2) trends in CO (X_{CO}) and AOD for the
 577 monthly anomaly values over different time periods for 19 regions. Standard error in the slopes
 578 are also shown. Systematic error is shown where it was found to be significant (Appendix A).
 579 Colors define the trend type, determined significant relative to one standard error. Red
 580 background colors denote positive trends, blue denotes negative trends and yellow denotes no
 581 significant trend. Region numbers correspond with regions in Fig. 2.

	Trend % per year (\pm standard error + systematic error)					
	CO			AOD		
	Full	1st half	2nd half	Full	1st half	2nd half
	July 2002- June 2018	July 2002- June 2010	July 2010- June 2018	July 2002- June 2018	July 2002- June 2010	July 2010- June 2018
Industrial						
1. NE China	-1.18 (0.3-0.1)	-1.94 (0.8)	-1.02 (0.7)	-0.97 (0.5)	1.70 (1.5)	-5.15 (1.5)
2. N India	-0.28 (0.2)	-0.56 (0.5)	-0.17 (0.5)	1.34 (0.7)	1.45 (1.9)	1.50 (2.2)
3. Europe	-0.89 (0.1+0.04)	-1.58 (0.3)	-0.47 (0.3)	-0.97 (0.4)	0.26 (1.2)	-1.51 (1.1)
4. E USA	-0.85 (0.1+0.03)	-1.59 (0.3)	-0.73 (0.4 ^a)	-2.06 (0.3)	-0.89 (1.7 ^a)	-3.84 (1.5 ^a)
Fire-prone						
5. NW USA	-0.85 (0.2+0.1)	-1.44 (0.5+0.1)	-0.67 (0.4)	0.26 (0.6)	2.85 (1.7)	-0.19 (2.7 ^a)
6. NW Canada	-0.60 (0.1+0.04)	-1.35 (0.4 ^a +0.05)	-0.51 (0.3+0.03)	-1.63 (0.3)	-4.21 (1.0)	-4.74 (1.2)
7. Siberia	-0.59 (0.2 ^a)	-1.34 (0.6 ^a -0.03)	-0.32 (0.4-0.03)	0.78 (1.0 ^a)	2.47 (3.6 ^a)	-2.51 (1.2)
8. Russia	-0.80 (0.1+0.1)	-1.38 (0.4+0.1)	-0.66 (0.3+0.1)	0.90 (0.9)	2.23 (2.3)	-3.35 (3.3)
9. Central America	-0.46 (0.1)	-1.05 (0.4)	-0.23 (0.4)	0.18 (0.4)	0.12 (1.1)	-0.03 (1.1)
10. S America	-0.31 (0.4 ^a)	-0.47 (1.0 ^a)	0.02 (1.0 ^a)	-0.43 (1.3 ^a)	-2.18 (3.7 ^a)	1.22 (3.2 ^a)
11. SAM Transport	-0.39 (0.2)	-0.77 (0.5)	-0.03 (0.8 ^a)	0.59 (0.3)	1.11 (0.7)	0.16 (0.8 ^a)
12. Central Africa	-0.22 (0.2)	-0.55 (0.5)	-0.12 (0.5)	-0.10 (0.5)	0.06 (1.4)	0.92 (1.4)
13. Sthrn Africa	-0.17 (0.3)	-0.63 (0.7)	-0.09 (0.7)	-0.12 (0.6)	-0.79 (1.8)	-0.77 (1.8)
14. SAf Transport	-0.07 (0.2)	-0.46 (0.6)	0.14 (0.6)	0.16 (0.4)	-0.30 (1.2)	-0.72 (1.1)
15. Maritime SEA	-0.51 (0.4 ^a -0.1)	-1.08 (1.0 ^a -0.2)	-0.14 (1.3 ^a)	-0.29 (1.0 ^a)	-0.73 (2.3 ^a)	0.07 (3.4 ^a)
16. NW Australia	-0.25 (0.3 ^a)	-0.79 (0.7 ^a)	0.03 (0.7 ^a)	0.31 (1.0)	1.23 (2.8)	-0.88 (3.1)
17. E Australia	-0.32 (0.2)	-0.90 (0.5)	0.16 (0.6 ^a)	0.47 (0.8)	1.02 (2.2)	-0.56 (2.5)
Background						
18. NH (0 to 60)	-0.57 (0.3)	-1.12 (0.9)	-0.43 (0.8)	Inconclusive due to land/ocean and mix of regions		
19. SH (-60 to 0)	-0.35 (0.3)	-0.9 (1)	-0.1 (1)			

582 *Cardinal directions are abbreviated (e.g. Northeast = NE), SAM = South America, SAf = Southern Africa
 583 ^aStandard error is taken from the estimate including autocorrelation where it is larger than the WLS estimate
 584 (Appendix A3)

585 **4. Discussion**

586 **4.1 Covariation of CO and AOD**

587 Co-variability analysis of CO and AOD provides further insights into trend behavior. Cloud
588 masking may contribute to some monthly variability, but quantifying this contribution is beyond
589 the scope of this study. However, we expect the main source of seasonal variability to be driven
590 by chemical and physical processes, as discussed in section 3.1. Additionally, because both
591 MOPITT and MODIS use the MODIS cloud detection, differences between their variability is
592 expected to be due to source or chemistry differences. Co-variability in the industrial regions,
593 (Fig. 5 and annual cycles in Supplementary Figure C3), ranges from little correlation between
594 peak CO and peak AOD (e.g. North India) to a strong relationship (e.g. Northeast China).

595

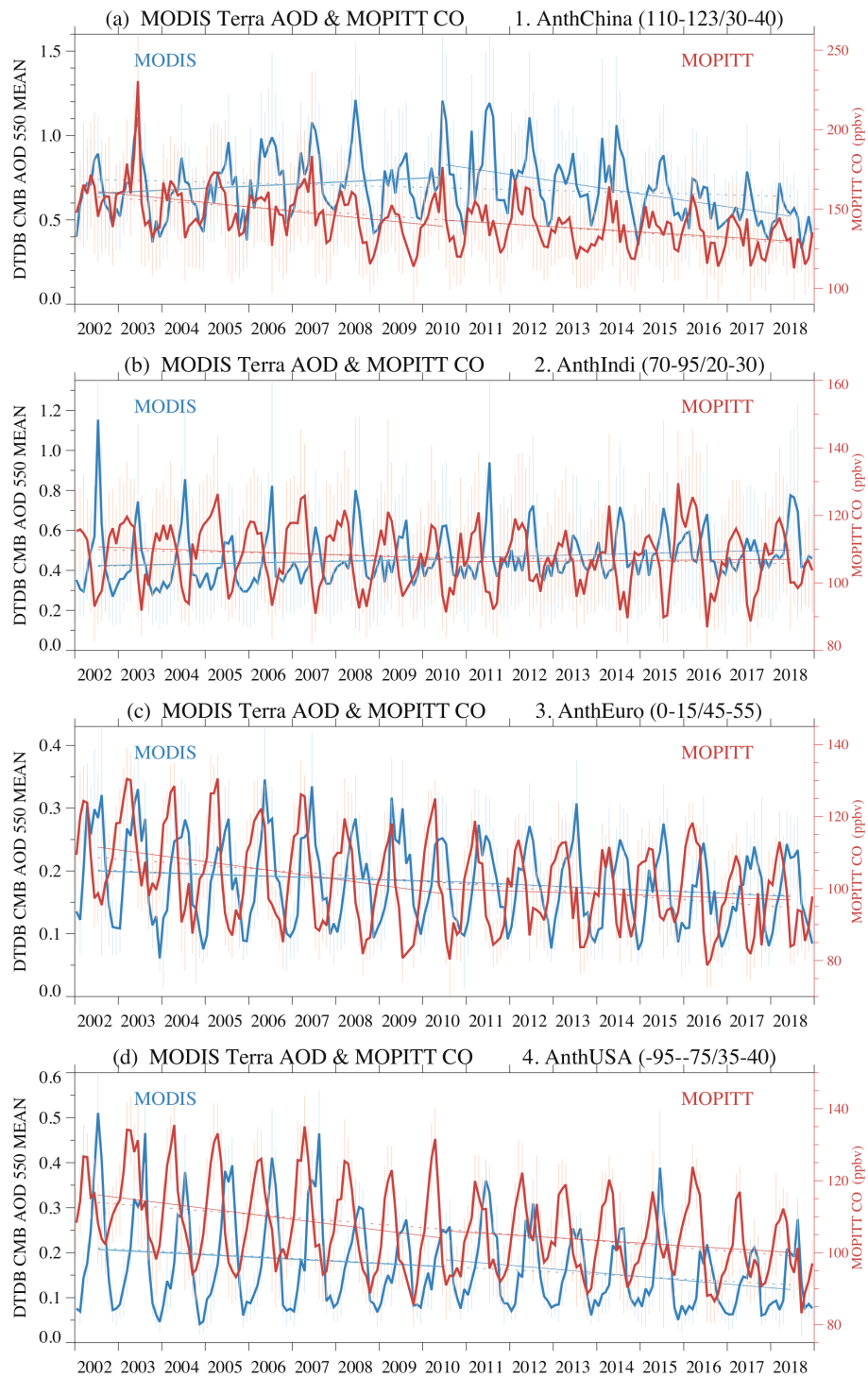
596 In Northeast China (Fig. 5a, Supplementary Figure C3), both CO and AOD peak in late
597 spring/early summer, but AOD remains high while CO rapidly decreases. This reflects the
598 opposite effects of OH photochemistry on CO and sulfate aerosols, as well as the impact of dust
599 aerosols on AOD during the dry summer months (Luo et al., 2014, Proestakis et al., 2018). The
600 residential, industrial, and transportation sectors dominate CO emissions in China (Streets et al.,
601 2006; Li et al., 2017). Residential CO emissions include biomass and coal burning (Wang and
602 Hao, 2012) and are generally higher in winter and spring than in summer (Liu et al., 2016). In
603 addition, agricultural burning usually peaks in June in this region (Wu et al., 2017; Li et al.,
604 2018) and may also contribute to high CO in June. The decline in Northeast China CO during the
605 first half of the record does not correspond with a decline in AOD. This reflects the move to
606 centralized energy production that improved combustion efficiency by replacing residential coal
607 use with electricity and natural gas. This change in energy production had relatively large

608 impacts on emissions of CO, but not on aerosols. In 2010, China implemented Clean Air Policies
609 (van der A et al., 2017; Zheng et al., 2018a) and as a result, AOD started decreasing along with
610 the continued decrease in CO, as seen at the inflection point around 2010 in Fig. 5a. This
611 inflection point is consistent with results found by Filonchyk et al. (2019) for the whole of China
612 using MODIS and MISR. The AOD decrease past 2010 is also consistent with reductions in
613 anthropogenically emitted aerosol precursors SO₂ and NO₂ since 2012 (Kroktov et al., 2016; Qu
614 et al. 2019; Wang and Wang, 2020).

615

616 Over North India, CO and AOD variability are out of phase (Fig. 5b, Supplementary Figure C3)
617 with CO peaking in early spring and AOD peaking in summer. The spring peak in North India
618 CO is related to the peak biomass burning activity (Bhardwaj et al. 2016). In India, mineral dust
619 makes a large contribution to total AOD during the pre-monsoon season (Apr-Jun) while at other
620 times of the year anthropogenic fine-mode aerosols are optically dominant (Sayer et al., 2014). A
621 positive trend in AOD over the full time period (Table 2) is due to several anthropogenic factors
622 including increased SO₂ and NO₂ emissions from coal-powered power plants (Kroktov et al.,
623 2016; Li et al., 2017; Qu et al. 2019; Wang and Wang, 2020), more frequent fog events near the
624 Indo-Gangetic Plain (Ghude et al., 2017), increased vehicular emissions (Manoj et al. 2019), and
625 increasing crop-residue burning activity (Jethva et al., 2019). This region also shows the least
626 negative CO trend, suggesting local emissions are offsetting the decreases in the global CO
627 background. India's CO emissions were increasing from 1996-2015 mainly due to increases in
628 residential and agricultural sources (Pandey et al. 2014) as well as due to power production and
629 transport activities (Sadavarte and Venkataraman 2014).

630

631
632
633634 Fig 5: Regional time series of month average X_{CO} (red) and AOD (blue) over industrial regions,

635 Region numbers correspond with numbers in Table 2 and Figure 2. Vertical bars are monthly
636 standard deviation. General tendencies from linear regression (WLS) are shown for the whole
637 record (July 2002-June 2018, dotted line), as well as the 1st half and 2nd half of the record (solid
638 lines). Slope values are described in Table 2.

639

640 In both Europe and Eastern USA, the peak CO occurs before the peak AOD (Fig 5c and 5d,
641 Supplementary Figure C3). This offset of several months is due to OH oxidation mainly driving
642 seasonality, which maximizes in summer to remove CO and concurrently produce sulfate aerosol
643 (Edwards et al., 2004). Both regions also show concomitant reductions in AOD and CO for the
644 whole time period, reflecting the implementation of strong air quality and climate-related
645 policies, as has been observed by reductions in anthropogenically emitted aerosol precursors SO₂
646 and NO₂ (Kroktov et al., 2016). Additionally, CO and AOD seasonal variability in both these
647 regions appear larger in the 1st half than the 2nd half of the record, suggesting reductions in the
648 peak emission months and potential impacts on the chemical oxidation environment.

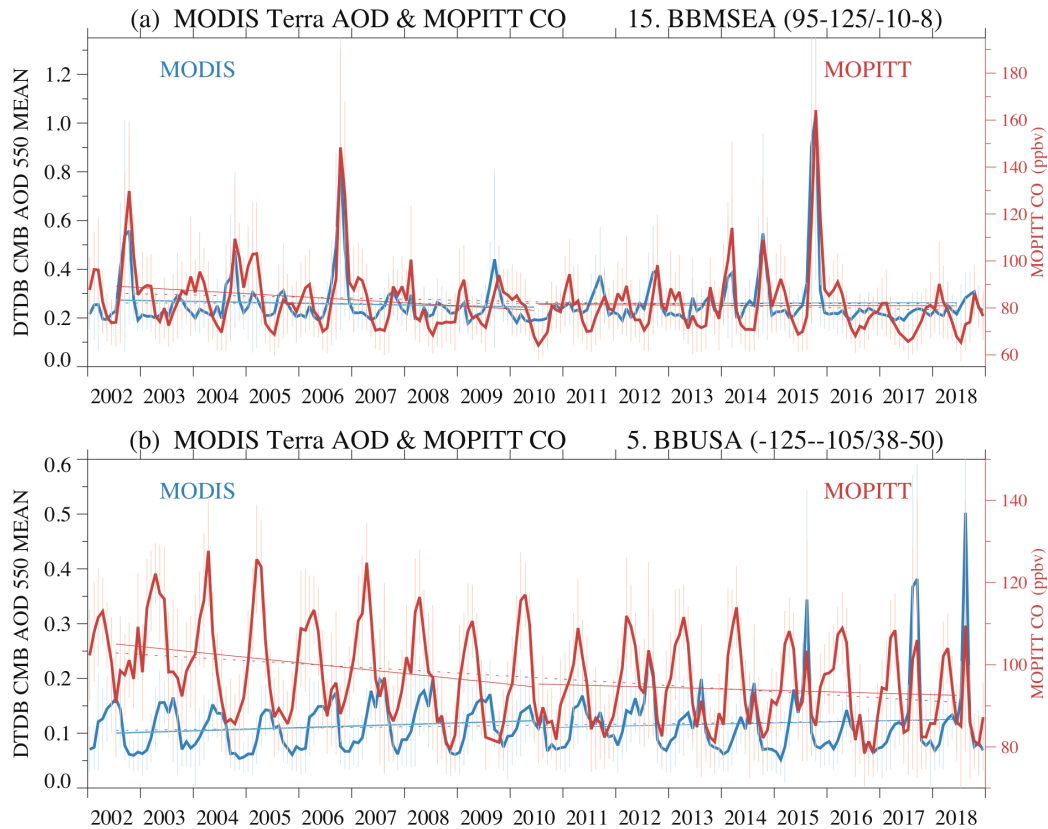
649

650 Fire-prone regions often experience strong correlation between CO and AOD (Fig. 6a,
651 Supplementary Figure C3). The longer lifetime of CO is also clear in these regions, as observed
652 by the peak AOD diminishing faster than CO, for example over Maritime SEA (Fig 6a). Over
653 northwest USA in the first half of the record, the CO seasonal cycle is dominated by a single
654 spring-time peak (Fig. 6b). A significant secondary CO peak shows up in late summer in the
655 second half of the record, and in some years is as large as the spring-time peak CO, for example
656 in 2017 and 2018. This coincides with a strengthening of the aerosol peak shoulder from about
657 2012 onwards. This pattern suggests a regime shift associated with increasing fire in the region.
658 Similar patterns are seen for the Canada and Siberia fire-prone regions (not shown).

659

660

661



663 Fig 6: Regional time series of X_{CO} (red) and AOD (blue) over (a) Maritime Southeast Asia and
 664 (b) the northwest USA example fire-prone regions. Vertical bars are monthly standard deviation.
 665 General tendencies from linear regression (WLS) are shown for July 2002-June 2018 (dotted
 666 line), as well as the 1st and 2nd half of the record (solid lines). Slope values are described in
 667 Table 2.

668 4.2 Separating CO trends by monthly percentiles

669 Trend analysis separated by month is used to determine the seasonal implications and potential
 670 sources of the long-term trend. Trends are calculated on the monthly means and percentiles
 671 (25th, median, 75th) between January, 2002, and December, 2018. Theil-Sen is used for trend

672 calculation to minimize the impact of outliers.

673

674 Resulting trend arrays show a range of information useful for interpreting trends (Fig.7, Fig. 8
675 and Appendix C). The size of the circle relates to the trend significance, with larger circles
676 indicating a higher significance level. The color of the circles denotes the strength of the trend,
677 with darker blues indicating stronger negative trends. The climatological annual cycle of column
678 average VMR is displayed in colored squares on the left-hand side of the graph, where the size of
679 the square represents the coefficient of variation - a larger square corresponds to higher
680 variability. Finally, the mean number of monthly retrievals are indicated on the right-hand side of
681 the plot.

682

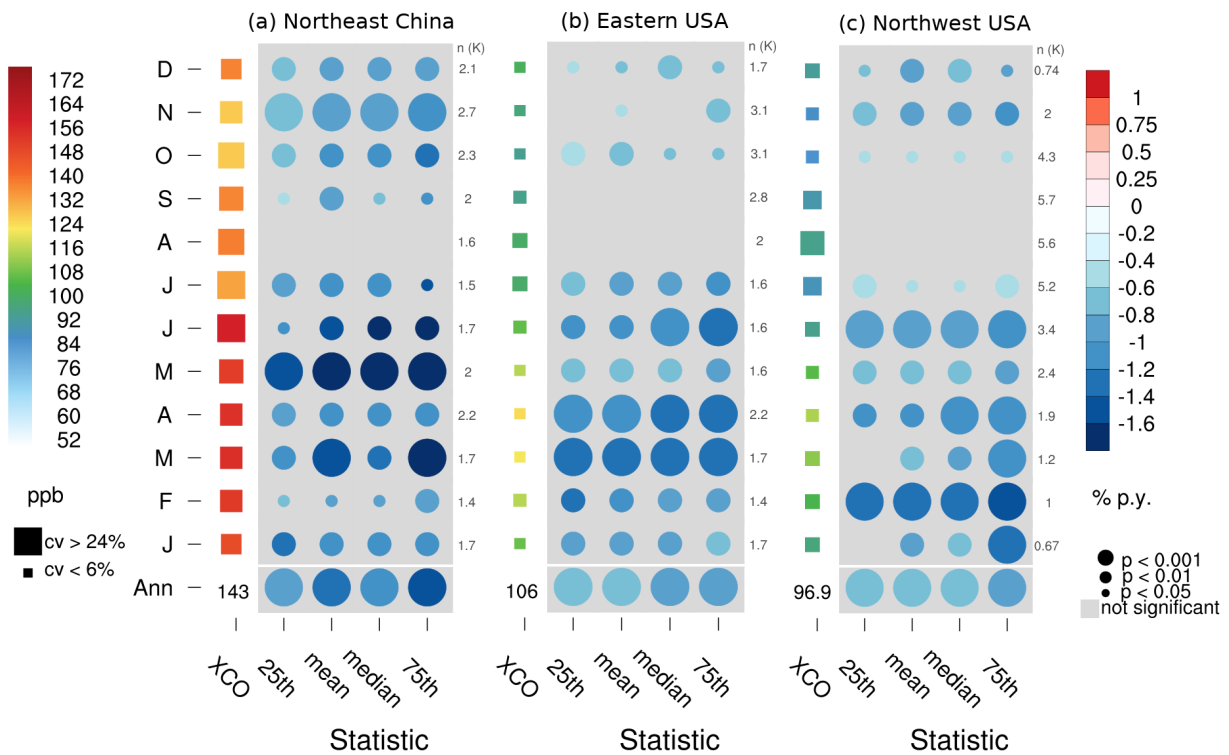
683 It is apparent from the trend arrays which months and percentiles have strong and weak trends.
684 Northeast China (Fig. 7a), experiences the strongest negative trends when compared to all other
685 regions. Spring months (March, May and June) in Northeast China experience the strongest
686 trends overall, at over -1.5 % per year for most of the percentiles in these months, which is
687 consistent with the trend results found by Zhang et al. (2020). The downward trend is likely to be
688 strongest in spring because the impact of residential emissions of CO is greatest. This is
689 supported by the downward trend in Northeast China CO being stronger in the 75th percentile
690 compared to the 25th percentile, suggesting the trend is driven by a reduction in highly polluted
691 events that would likely result from local sources.

692

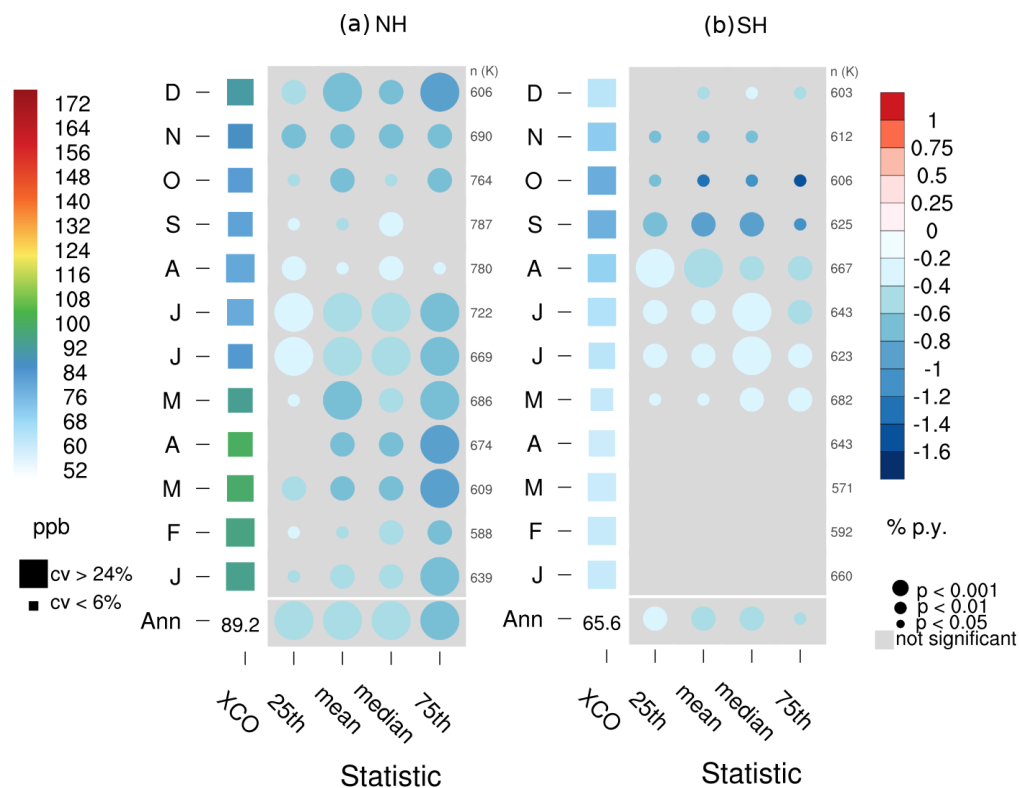
693 Eastern USA (Fig 7c) and Europe (Appendix C), also see stronger trends in the 75th vs. the 25th
694 percentile, albeit smaller in magnitude compared to Northeast China, implicating local emission
695 reductions. In contrast, the trend array for North India (Appendix C) shows few significant

696 trends, reflecting that high variability or a positive trend locally counteracts any reductions in
 697 transported CO. Where they are significant, trends occur more frequently in the 25th percentile,
 698 representing a trend in background CO.

699



710 Many regions of the NH do not see significant trends in late summer and early autumn, i.e.
 711 August and September (e.g. Fig. 7). This leads to small trends with low significance for the
 712 whole NH during these months (Fig. 8a). Several factors may be influencing the CO trend in
 713 these months. The large summer sink may effectively process any sources independent of the
 714 magnitude, smoothing out any trend behavior. Additionally, variability is relatively large in these
 715 months (see c.v. for Northeast China and Northwest USA in Fig 7a and c, respectively), which
 716 impacts the determination of significant trends. Finally, the recent upward trend in peak CO for
 717 boreal fire-prone regions described in Section 4.1 (e.g. Fig. 6b) likely counteracts a downward
 718 trend. Fire emissions in these boreal regions impact not only the local atmosphere, but also
 719 downwind regions through atmospheric transport, and may be responsible for a hemispheric
 720 weakening of the CO trend in these months. A modeling study would be required to quantify the
 721 contributions of each of these processes to trend determination.



722

723 Fig 8: Same as Fig 7, but for (a) NH and (b) SH.

724

725 While the NH shows negative trends across all months of the year, the SH trends are more
726 confined to one season. The SH sees no significant trends in mid-summer to early autumn (Fig
727 8b), suggesting that sources are in equilibrium with the photochemical sink at this time of year.
728 The downward CO trend is dominant in the fire season (Aug-Nov), which is consistent with the
729 Andela et al. (2017) global decrease in burned area, and considering biomass burning is the
730 major source of CO emissions in the SH (Holloway et al., 2000). Small CO trends prior to the
731 SH burning season (May-July) may reflect a trend in transported air from the NH (Zeng et al.,
732 2012; Yang et al., 2019). Overall, the SH trend is mainly determined by the trend from fires,
733 while the NH trend also reflects improvements in combustion efficiency.

734

735 **5. Conclusions**

736 We use long-term measurements of MOPITT CO and MODIS AOD, taken from the Terra
737 satellite, launched in December, 1999, to estimate global and regional trends in atmospheric
738 pollution. Our study principal results are summarized below:

739 1) We find a decreasing global trend in CO total column: $-0.50 (\pm 0.3) \%$ per year over
740 2002 to 2018. This trend represents a global slowdown in the CO decline as compared to
741 CO trends from earlier studies over shorter periods that found a trend of -1% per year. We
742 attribute the slow-down to a reduced negative trend in recent years by comparing trends
743 for 2002-2010 with 2010-2018.

744 2) All the TIR CO satellite records from MOPITT, AIRS, TES, IASI and CrIS observe the
745 same hemispherical seasonality and interannual variations. This provides confidence in
746 the MOPITT record for our subsequent detailed trend estimates. The AIRS CO NH and
747 SH trends agree with MOPITT, while the other satellite instrument records are of

748 insufficient length or lack processing consistency to allow for confident computation of
749 trends.

750 3) Due to the shorter lifetime of aerosol, global trends in AOD were not significant.

751 However, significant regional trends in AOD help interpret CO variability for areas with
752 common sources, as in fire-prone regions, or where there are impacts due to air quality
753 regulations. CO and AOD concurrently decrease in North America, Europe, and more
754 recently, China. India has increasing trends in AOD and negligible trends in CO,
755 indicating regional CO emissions are sufficiently large to counteract the global declining
756 CO background.

757 4) Analyses of trends by percentile and month indicate that the strongest (most negative)
758 trends occur in the 75th percentile for the NH and that late summertime CO trends (when
759 CO lifetime is shortest) are the least significant, in both hemispheres.

760

761 Overall, local contributions from human pollution or fire emissions can counteract the global
762 downward trend in CO. In particular, the climate-driven positive fire trend in the NH boreal fire-
763 prone regions during summer locally counteracts the global downward CO trend and may also
764 have hemispheric impacts through subsequent transport. Monitoring changes in regions with
765 high local emissions will be critical for diagnosing future air quality and informing mitigation
766 efforts.

767

768 **DATA STATEMENT**

769 All satellite data are publicly available. Please see Table 1 and section 2.1.2 for links to data
770 sources. NH and SH month average CO from all the instruments are available at NCAR RDA
771 (doi in progress). The regional month average CO for each region (along with statistics and

772 metadata) can also be found at NCAR RDA (doi in progress).

773

774 **AUTHOR CONTRIBUTIONS**

775 RRB led the design of the study and performed the CO trend analysis, HMW helped design the
776 study, interpret results and computed CO trend maps. MP performed the AOD trend analysis, GF
777 worked on trend error estimation and CrIS monthly means, MD, DPE, LKE, BG, JG, SMA and
778 JRD provided guidance with MOPITT data and interpretation of results. WT led the discussion
779 of trends in China. RK led the discussion of trends in India. JW and ZW provided the AIRS data.
780 CC, MG, PFC and DH provided the IASI data. KWB, ML, VHP, JW and SK provided the TES
781 and CrIS data. MC and RL advised on the use of MODIS AOD data and the interpretation of
782 AOD distributions and trends. All authors contributed to the review and editing of the
783 manuscript.

784

785 **ACKNOWLEDGEMENTS**

786 The National Center for Atmospheric Research (NCAR) is sponsored by the National Science
787 Foundation. The NCAR MOPITT project is supported by the National Aeronautics and Space
788 Administration (NASA) Earth Observing System (EOS) Program. The MOPITT team also
789 acknowledges support from the Canadian Space Agency (CSA), the Natural Sciences and
790 Engineering Research Council (NSERC) and Environment Canada, and the contributions of
791 COMDEV (the prime contractor) and ABB BOMEM. This work was funded by NASA ROSES
792 TASNPP, contract 80NSSC18K0687. Part of this research was carried out at the Jet Propulsion
793 Laboratory, California Institute of Technology, under a contract with NASA. TES data are
794 available from the NASA Langley Research Center Atmospheric Science Data Center. IASI is a

795 joint mission of EUMETSAT and the Centre National d'Etudes Spatiales (CNES, France). The
796 IASI L1 and L2 input data are distributed in near real time by EUMETSAT through the
797 EumetCast system distribution. The IASI team also acknowledges the French AERIS atmospheric
798 database (<https://iasi.aeris-data.fr/>) for providing the IASI L1C data and L2 data disseminated via
799 EUMETcast, as well as CNES and CNRS for financial support. This work is also part of the
800 EUMETSAT/AC SAF project. The research on IASI was also supported by BELSPO and ESA
801 (Prodex arrangement IASI.Flow). MODIS is a sensor aboard NASA's Terra and Aqua satellite
802 missions. Native resolution L1B, L2 aerosol retrievals, and the gridded L3 atmospheric product
803 used here (MOD08_M3) are all distributed via the LAADS DAAC
804 (<https://ladsweb.modaps.eosdis.nasa.gov/>). We thank NCAR internal reviewers William Randel
805 and Douglas Kinnison for their valuable suggestions.

806

807

808 **REFERENCES**

- 809 AIRS Science Team/Joao Teixeira, (2013), **AIRS/Aqua L2 Standard Physical Retrieval**
810 **(AIRS-only) V006**, Greenbelt, MD, USA, Goddard Earth Sciences Data and Information
811 Services Center (GES DISC), Accessed: [31 October, 2019],
812 <https://doi.org/10.5067/Aqua/AIRS/DATA202>.
- 813 Andela, N., D. C. Morton, L. Giglio, Y. Chen, G. R. van der Werf, P. S. Kasibhatla, R. S.
814 DeFries, G. J. Collatz, S. Hantson, S. Kloster, D. Bachelet, M. Forrest, G. Lasslop, F. Li, S.
815 Mangeon, J. R. Melton, C. Yue, J. T. Randerson, (2017). **A human-driven decline in global**
816 **burned area**, Science, 356(6345): 1356-1362, <https://doi.org/10.1126/science.aal4108>.
- 817 Arellano, A. F., P. G. Hess, D. P. Edwards, D. Baumgardner, (2010). **Constraints on black**
818 **carbon aerosol distribution from Measurement of Pollution in the Troposphere (MOPITT)**
819 **CO**, Geophys. Res. Lett., 37(17): 17801, <https://doi.org/10.1126/science.aal4108>.
- 820 Aumann, H. H., M. T. Chahine, C. Gautier, M. D. Goldberg, E. Kalnay, L. M. McMillin, H.
821 Revercomb, P. W. Rosenkranz, W. L. Smith, D. H. Staelin, L. L. Strow, J. Susskind, (2003).
822 **AIRS/AMSU/HSB on the Aqua mission: design, science objectives, data products, and**
823 **processing systems**, IEEE Trans. Geosci. Remote Sens., 41 (2): 253-264,
824 <https://doi.org/10.1109/TGRS.2002.808356>.
- 825 Beer, R, (2006). **TES on the Aura Mission: Scientific Objectives, Measurements, and**
826 **Analysis Overview**, IEEE Trans. Geosci. Remote Sensing, 44: 1102- 1105,
827 <https://doi.org/10.1109/TGRS.2005.863716>.
- 828 Bhardwaj, P., M. Naja, R. Kumar, H. C. Chandola, (2016). **Seasonal, interannual and long**
829 **term variabilities in biomass burning activity over South Asia**, Environ. Sci. Pollut. R., 23:
830 4397-4410, <https://doi.org/10.1007/s11356-015-5629-6>.

831 Bowman, K. W., C. D. Rodgers, S. S. Kulawik, J. Worden, E. Sarkissian, G. Osterman, T.
832 Steck, M. Lou, A. Eldering, M. Shephard, H. Worden, M. Lampel, S. Clough, P. Brown, C.
833 Rinsland, M. Gunson, R. Beer, (2006). **Tropospheric Emission Spectrometer: Retrieval**
834 **Method and Error Analysis**, IEEE Trans. Geosci. Remote Sensing, 44: 1297-1307,
835 <https://doi.org/10.1109/TGRS.2006.871234>.

836 Bowman, K., D. K. Henze, (2012). **Attribution of direct ozone radiative forcing to**
837 **spatially resolved emissions**. Geophys. Res. Lett., 39(22): L22704,
838 <https://doi.org/10.1029/2012GL053274>.

839 Buchholz, R.R., M. N. Deeter, H. M. Worden, J. Gille, D. P. Edwards, J. W. Hannigan, N. B.
840 Jones, C. Paton-Walsh, D. W. T. Griffith, D. Smale, J. Robinson, K. Strong, S. Conway, R.
841 Sussmann, F. Hase, T. Blumenstock, E. Mahieu, B. Langerock, (2017). **Validation of MOPITT**
842 **Carbon Monoxide Using Ground-Based Fourier Transform Infrared Spectrometer Data**
843 **from NDACC**, Atmos. Meas. Tech. 10 (5): 1927-56. <https://doi.org/10.5194/amt-10-1927-2017>.

844 Buchholz, R. R., D. Hammerling, H. M. Worden, M. N. Deeter, L. K. Emmons, D. P.
845 Edwards, S. A. Monks, (2018). **Links Between Carbon Monoxide and Climate Indices for the**
846 **Southern Hemisphere and Tropical Fire Regions**, J. Geophys. Res.-Atmos. 123 (17): 9786-
847 9800, <https://doi.org/10.1029/2018JD028438>.

848 Clerbaux, C., A. Boynard, L. Clarisse, M. George, J. Hadji-Lazaro, H. Herbin, D. Hurtmans,
849 M. Pommier, A. Razavi, S. Turquety, C. Wespes, P.-F. Coheur, (2009). **Monitoring of**
850 **atmospheric composition using the thermal infrared IASI/MetOp sounder**, Atmos. Chem.
851 Phys., 9: 6041-6054. <https://doi.org/10.5194/acp-9-6041-2009>.

852 de Ruyter de Wildt, M., H. Eskes, K. F. Boersma, (2012). **The global economic cycle and**
853 **satellite-derived NO2 trends over shipping lanes**, Geophys. Res. Lett., 39: L01802,

854 <https://doi.org/10.1029/2011GL049541>.

855 Deeter, M. N., D. P. Edwards, G. L. Francis, J. C. Gille, D. Mao, S. Martinez-Alonso, H. M.
856 Worden, D. Ziskin, and M. O. Andreae (2019), **Radiance-based retrieval bias mitigation for**
857 **the MOPITT instrument: the version 8 product**, *Atmos. Meas. Tech.*, 12(8): 4561–4580,
858 <https://doi.org/10.5194/amt-12-4561-2019>.

859 Deeter, M. N., S. Martínez-Alonso, M. O. Andreae, H. Schlager, (2018). **Satellite-based**
860 **analysis of CO seasonal and interannual variability over the Amazon Basin**, *J. Geophys.*
861 *Res.-Atmos.*, 123: 5641–5656, <https://doi.org/10.1029/2018JD028425>.

862 Deeter, M. N., D. P. Edwards, J. C. Gille, H. M. Worden (2015), **Information content of**
863 **MOPITT CO profile retrievals: Temporal and geographical variability**, *J. Geophys. Res.*
864 *Atmos.*, 120(12): 723–12,738, <https://doi.org/10.1002/2015JD024024>.

865 Deeter, M. N., Martínez-Alonso, S., Edwards, D. P., Emmons, L. K., Gille, J. C., Worden, H.
866 M., Pittman, J. V., Daube, B. C., and Wofsy, S. C., (2013), **Validation of MOPITT Version 5**
867 **thermal-infrared, near-infrared, and multispectral carbon monoxide profile retrievals for**
868 **2000–2011**, *J. Geophys. Res. Atmos.*, 118, 6710– 6725, doi:[10.1002/jgrd.50272](https://doi.org/10.1002/jgrd.50272).

869 Deeter, M. N., L. K. Emmons, G. L. Francis, D. P. Edwards, J. C. Gille, J. X. Warner, B.
870 Khattatov, D. Ziskin, J.-F. Lamarque, S. P. Ho, V. Yudin, J. L. Attie, D. Packman, J. Chen, D.
871 Mao, J. R. Drummond, P. Novelli, G. Sachse, (2004). **Evaluation of operational radiances for**
872 **the Measurements of Pollution in the Troposphere (MOPITT) instrument CO thermal**
873 **band channels**, *J. Geophys. Res.*, 109: D03308, <https://doi.org/10.1029/2003JD003970>.

874 Dennison, P. E., S. C. Brewer, J. D. Arnold, M. A. Moritz, (2014). **Large wildfire trends in**
875 **the western United States, 1984–2011**, *Geophys. Res. Lett.*, 41: 2928–2933,
876 <https://doi.org/10.1002/2014GL059576>.

- 877 Drummond, J. R., J. Zou, F. Nichitiu, J. Kar, R. Deschambaut, J. Hackett, (2010). **A review**
878 **of 9-year performance and operation of the MOPITT instrument**, Advances in Space
879 Research, 45(6): 760-774, <https://doi.org/10.1016/j.asr.2009.11.019>.
- 880 Edwards, D. P., L. K. Emmons, D. A. Hauglustaine, D. A. Chu, J. C. Gille, Y. J. Kaufman, G.
881 Pétron, L. N. Yurgano, v L. Giglio, M. N. Deeter, V. Yudi, n D. C. Ziskin, J. Warner, J.-F.
882 Lamarque, G. L. Francis, S. P. Ho, D. Mao, J. Chen, E. I. Grechk, o J. R. Drummond, (2004).
883 **Observations of Carbon Monoxide and Aerosols from the Terra Satellite: Northern**
884 **Hemisphere Variability**, J. Geophys. Res.-Atmos., 109 (D24),
885 <https://doi.org/10.1029/2004JD004727>.
- 886 Edwards, D. P., L. K. Emmons, J. C. Gille, A. Chu, J.-L. Attié, L. Giglio, S. W. Wood, J.
887 Haywood, M. N. Deeter, S. T. Massie, D. C. Ziskin, J. R. Drummond, (2006). **Satellite-observed**
888 **pollution from Southern Hemisphere biomass burning**, J. Geophys. Res., 111: D14312,
889 <https://doi.org/10.1029/2005JD006655>.
- 890 Efron, B. (1979). **Bootstrap Methods: Another Look at the Jackknife**, Ann. Statist. 7 (1):
891 1-26. <https://doi.org/10.1214/aos/1176344552>.
- 892 Field, R. D., G. R. van der Werf, T. Fanin, E. J. Fetzer, R. Fuller, H. Jethva, R. Levy, N. J.
893 Livesey, M. Luo, O. Torres, H. M. Worden, (2016). **Indonesian fire activity and smoke**
894 **pollution in 2015 show persistent nonlinear sensitivity to El Nino-induced drought**, Proc.
895 Natl. Acad. Sci. USA, 113(33): 9204-9209, <https://doi.org/10.1073/pnas.1524888113>.
- 896 Filonchyk, M., H. Yan, Z. Zhang, S. Yang, W. Li, Y. Li, (2019). **Combined use of satellite**
897 **and surface observations to study aerosol optical depth in different regions of China**, Sci.
898 Rep., 9, 6174, <https://doi.org/10.1038/s41598-019-42466-6>.
- 899 Fu, D., K. W. Bowman, H. M. Worden, V. Natraj, J. R. Worden, S. Yu, P. Veeffkind, I. Aben, J.

- 900 Landgraf, L. Strow, Y. Han, (2016). **High-resolution tropospheric carbon monoxide profiles**
901 **retrieved from CrIS and TROPOMI**, Atmos. Meas. Tech., 9(6): 2567-2579,
902 <http://dx.doi.org/10.5194/amt-9-2567-2016>.
- 903 Gambacorta, A., (2013) The NUCAPS algorithm theoretical basis documentation 2013.
904 [Online].
905 [https://www.ospo.noaa.gov/Products/atmosphere/soundings/nucaps/docs/NUCAPS_ATBD_2013](https://www.ospo.noaa.gov/Products/atmosphere/soundings/nucaps/docs/NUCAPS_ATBD_2013_0821.pdf)
906 [0821.pdf](https://www.ospo.noaa.gov/Products/atmosphere/soundings/nucaps/docs/NUCAPS_ATBD_2013_0821.pdf)
- 907 Gambacorta, A., C. Barnet, W. Wolf, T. King, E. Maddy, L. Strow, X. Xiong, N. Nalli, M.
908 Goldberg, (2014). **An experiment using high spectral resolution CrIS measurements for**
909 **atmospheric trace gases: carbon monoxide retrievals impact study**, IEEE Geosci. Remote S.,
910 11: 1639-1643, <https://doi.org/10.1109/LGRS.2014.2303641>.
- 911 Gaubert, B., A. F. Arellano, J. Barré, H. M. Worden ,L. K. Emmons, S. Tilmes, R. R.
912 Buchholz, F. Vitt, K. Raeder, N. Collins, J. L. Anderson, C. Wiedinmyer, S. Martinez Alonso, D.
913 P. Edwards, M. O. Andreae, J. W. Hannigan, C. Petri, K. Strong, N. Jones, (2016). **Toward a**
914 **chemical reanalysis in a coupled chemistry-climate model: An evaluation of MOPITT CO**
915 **assimilation and its impact on tropospheric composition**, J. Geophys. Res. Atmos., 121: 7310-
916 7343, <https://doi.org/10.1002/2016JD024863>.
- 917 Gaubert, B., H. M. Worden, A. F. J. Arellano, L. K. Emmons, S. Tilmes, J. Barré, S. Martinez
918 Alonso, F. Vitt, J. L. Anderson, F. Alkemade, S. Houweling, D. P. Edwards (2017a). **Chemical**
919 **feedback from decreasing carbon monoxide emissions**, Geophysical Research Letters, 44:
920 9985-9995, <https://doi.org/10.1002/2017GL074987>.
- 921 Gaubert, B., H. Worden, (2017b). **NCAR/MOPITT Reanalysis**, Research Data Archive at
922 the National Center for Atmospheric Research, Computational and Information Systems

923 Laboratory. <https://doi.org/10.5065/D6SB44GZ>, Accessed 13 Sep 2019.

924 George, M., C. Clerbaux, D. Hurtmans, S. Turquety, P.-F. Coheur, M. Pommier, J. Hadji-
925 Lazaro, D.P. Edwards, H. Worden, M. Luo, C. Rinsland, W. McMillan, (2009). **Carbon**
926 **monoxide distributions from the IASI/METOP mission: evaluation with other space-borne**
927 **remote sensors**, Atmos. Chem. Phys., 9: 8317-8330, <https://doi.org/10.5194/acp-9-8317-2009>.

928 George, M., C. Clerbaux, I. Bouarar, P.-F. Coheur, M. N. Deeter, D. P. Edwards, G. Francis,
929 J. C. Gille, J. Hadji-Lazaro, D. Hurtmans, A. Inness, D. Mao, H. M. Worden, (2015). **An**
930 **examination of the long-term CO records from MOPITT and IASI: comparison of retrieval**
931 **methodology**, Atmos. Meas. Tech., 8(10): 4313-4328, <https://doi.org/10.5194/amt-8-4313-2015>.

932 Ghude, S. D., G. S. Bhat, T. Prabhakaran, R. K. Jenamani, D. M. Chate, P. D. Safai, A. K.
933 Karipot, M. Konwar, P. Pithani, V. Sinha, P. S. P. Rao, S. A. Dixit, S. Tiwari, K. Todekar, S.
934 Varpe, A. K. Srivastava, D. S. Bisht, P. Murugavel, K. Ali, U. Mina, M. Dharua, Y. Jaya Rao, B.
935 Padmakumari, A. Hazra, N. Nigam, U. Shende, D. M. Lal, B. P. Chandra, A. K. Mishra, A.
936 Kumar, H. Hakkim, H. Pawar, P. Acharja, R. Kulkarni, C. Subharthi, B. Balaji, M. Varghese, S.
937 Bera, M. Rajeevan, (2017). **Winter Fog Experiment Over the Indo-Gangetic Plains of India**,
938 Current Science, 112: 767-784, <https://doi.org/10.18520/cs/v112/i04/767-784>.

939 Gupta, P., L. A. Remer, F. Patadia, R. C. Levy, S. A. Christopher, (2020). **High-Resolution**
940 **Gridded Level 3 Aerosol Optical Depth Data from MODIS**, Remote Sens., 12, 2847,
941 <https://doi.org/10.3390/rs12172847>.

942 Hedelius, J. K., T. -L. He, D. B. A. Jones, B. C. Baier, R. R. Buchholz, M. De Mazière, N. M.
943 Deutscher, M. K. Dubey, D. G. Feist, D. W. T. Griffith, F. Hase, L. T. Iraci, P. Jeseck, M. Kiel, R.
944 Kivi, C. Liu, I. Morino, J. Notholt, Y. -S. Oh, H. Ohyama, D. F. Pollard, M. Rettinger, S. Roche,
945 C. M. Roehl, M. Schneider, K. Shiomi, K. Strong, R. Sussmann, C. Sweeney, Y. T^v{e}, O.

- 946 Uchino, V. A. Velazco, W. Wang, T. Warneke, P. O. Wennberg, H. M. Worden, D. Wunch, (2019).
947 **Evaluation of MOPITT Version 7 joint TIR-NIR XCO retrievals with TCCON**, Atmos.
948 Meas. Tech., 12(10): 5547-5572, <https://doi.org/10.5194/amt-12-5547-2019>.
- 949 Holloway, T., H. Levy II, P. Kasibhatla, (2000). **Global distribution of carbon monoxide**, J.
950 Geophys. Res., 105(D10): 12,123-12,147, <https://doi.org/10.1029/1999JD901173>.
- 951 Huijnen, V., M. J. Wooster, J. W. Kaiser, D. L. A. Gaveau, J. Flemming, M. Parrington, A.
952 Inness, D. Murdiyarsa, B. Main, M. van Weele, (2016). **Fire carbon emissions over maritime**
953 **southeast Asia in 2015 largest since 1997**, Sci. Rep. 6: 26886,
954 <https://doi.org/10.1038/srep26886>.
- 955 Hurtmans, D., P.-F. Coheur, C. Wespes, L. Clarisse, O. Scharf, C. Clerbaux, J. Hadji-Lazaro,
956 M. George, S. Turquety, (2012). **FORLI radiative transfer and retrieval code for IASI**, J.
957 Quant. Spectrosc. Ra., 113: 1391-1408, <https://doi.org/10.1016/j.jqsrt.2012.02.036>.
- 958 Hsu, N. C., M.-J. Jeong, C. Bettenhausen, A. M. Sayer, R. Hansell, C. S. Seftor, J. Huang,
959 C.-C. Tsay, (2013), **Enhanced Deep Blue aerosol retrieval algorithm: The second generation**,
960 J. Geophys. Res. Atmos., 118: 9296-9315, <https://doi.org/10.1002/jgrd.50712>.
- 961 Jiang, Z., D. B. A. Jones, J. Worden, H. M. Worden, D. K. Henze, Y. X. Wang, (2015).
962 **Regional Data Assimilation of Multi-Spectral MOPITT Observations of CO over North**
963 **America**, Atmos. Chem. Phys. 15(12): 6801-14. <https://doi.org/10.5194/acp-15-6801-2015>.
- 964 Jiang, Z., J. R. Worden, H. Worden, M. Deeter, D. B. A. Jones, A. F. Arellano, D. K. Henze,
965 (2017). **A 15-Year Record of CO Emissions Constrained by MOPITT CO Observations**,
966 Atmos. Chem. Phys. 17(7): 4565–83. <https://doi.org/10.5194/acp-17-4565-2017>.
- 967 Jiang, Z., B. C. McDonald, H. Worden, J. R. Worden, K. Miyazaki, Z. Qu, D. K. Henze, D.

968 B. A. Jones, A. F. Arellano, E. V. Fischer, L. Zhu, K. F. Boersma, (2018). **Unexpected slowdown**
969 **of US pollutant emission reduction in the past decade**, PNAS, 115(20): 5099-5104,
970 <https://doi.org/10.1073/pnas.1801191115>.

971

972

973 Kanakidou, M., J. H. Seinfeld, S. N. Pandis, I. Barnes, F. J. Dentener, M. C. Facchini, R. Van
974 Dingenen, B. Ervens, A. Nenes, C. J. Nielsen, E. Swietlicki, J. P. Putaud, Y. Balkanski, S. Fuzzi,
975 J. Horth, G. K. Moortgat, R. Winterhalter, C. E. L. Myhre, K. Tsigaridis, E. Vignati, E. G.
976 Stephanou, J. Wilson, (2005). **Organic aerosol and global climate modelling: a review**, Atmos.
977 Chem. Phys., 5: 1053-1123, <https://doi.org/10.5194/acp-5-1053-2005>.

978 Kendall, M. G., (1975). **Rank Correlation Methods**, 4th edition, Charles Griffin, London.

979 Kerzenmacher, T., B. Dils, N. Kumps, T. Blumenstock, C. Clerbaux, P.-F. Coheur, P.

980 Demoulin, O. García, M. George, D.W.T. Griffith, F. Hase, J. Hadji-Lazaro, D. Hurtmans, N.

981 Jones, E. Mahieu, J. Notholt, C. Paton-Walsh, U. Raffalski, T. Ridder, M. Schneider, C. Servais,

982 M. De Mazière, (2012). **Validation of IASI FORLI carbon monoxide retrievals using FTIR**

983 **data from NDACC**, Atmos. Meas. Tech., 5, 2751–2761, <https://doi.org/10.5194/amt-5-2751->

984 [2012](https://doi.org/10.5194/amt-5-2751-2012).

985 King, M. D., S. Platnick, W. P. Menzel, S. A. Ackerman, P. A. Hubanks, (2013). **Spatial and**
986 **temporal distribution of clouds observed by MODIS onboard the Terra and Aqua satellites**,
987 IEEE Trans. Geosci. Remote Sens., 51: 3826-3852, <https://doi.org/10.1109/TGRS.2012.2227333>.

988 Klonecki, A., M. Pommier, C. Clerbaux, G. Ancellet, J.-P. Cammas, P.-F. Coheur, A. Cozic,

989 G.S. Diskin, J. Hadji-Lazaro, D.A. Hauglustaine, D. Hurtmans, B. Khattatov, J.-F. Lamarque,

- 990 K.S. Law, P. Nedelec, J.-D. Paris, J.R. Podolske, P. Prunet, H. Schlager, S. Szopa, S. Turquety,
991 (2012). **Assimilation of IASI satellite CO fields into a global chemistry transport model for**
992 **validation against aircraft measurements**, *Atmos. Chem. Phys.*, 12: 4493-4512,
993 <https://doi.org/10.5194/acp-12-4493-2012>.
- 994 Krishna Moorthy, K., S. Suresh Babu, M. R. Manoj, S. K. Satheesh, (2013). **Buildup of**
995 **aerosols over the Indian Region**, *Geophys. Res. Lett.*, 40: 1011-1014,
996 <https://doi.org/10.1002/grl.50165>.
- 997 Krotkov, N. A., C. A. McLinden, C. Li, L. N. Lamsal, E. A. Celarier, S. V. Marchenko, W. H.
998 Swartz, E. J. Bucsela, J. Joiner, B. N. Duncan, K. F. Boersma, J. P. Veefkind, P. F. Levelt, V. E.
999 Fioletov, R. R. Dickerson, H. He, Z. Lu, D. G. Streets, (2016). **Aura OMI observations of**
1000 **regional SO₂ and NO₂ pollution changes from 2005 to 2015**, *Atmos. Chem. Phys.*, 16, 4605-
1001 4629, <https://doi.org/10.5194/acp-16-4605-2016>.
- 1002 Kulawik, S. S., J. Worden, A. Eldering, K. Bowman, M. Gunson, G. B. Osterman, L. Zhang,
1003 S. Clough, M. W. Shephard, R. Beer, (2006). **Implementation of cloud retrievals for**
1004 **Tropospheric Emission Spectrometer (TES) atmospheric retrievals: part 1. Description and**
1005 **characterization of errors on trace gas retrievals**, *J. Geophys. Res.*, 111: D24204,
1006 <https://doi.org/10.1029/2005JD006733>.
- 1007 Lack, D. A., X. X. Tie, N. D. Bofinger, A. N. Wiegand, S. Madronich, (2004). **Seasonal**
1008 **variability of secondary organic aerosol: A global modelling study**, *J. Geophys. Res.*, 109:
1009 D03203 <https://doi.org/10.1029/2003JD003418>.
- 1010 Lelieveld, J., S. Gromov, A. Pozzer, D. Taraborrelli, (2016). **Global tropospheric hydroxyl**
1011 **distribution, budget and reactivity**, *Atmos. Chem. Phys.*, 16: 12477-12493,
1012 <https://doi.org/10.5194/acp-16-12477-2016>.

- 1013 Levy, R. C., S. Mattoo, V. Sawyer, Y. Shi, P. R. Colarco, A. I. Lyapustin, Y. Wang, L. A.
1014 Remer, (2018). **Exploring systematic offsets between aerosol products from the two MODIS**
1015 **sensors**, Atmos. Meas. Tech., 11: 4073-4092, <https://doi.org/10.5194/amt-11-4073-2018>.
- 1016 Levy, R. C., S. Mattoo, L. A. Munchak, L. A. Remer, A. M. Sayer, F. Patadia, N. C. Hsu,
1017 (2013). **The Collection 6 MODIS Aerosol Products over Land and Ocean**, Atmos. Meas.
1018 Tech. 6 (11): 2989-3034, <https://doi.org/10.5194/amt-6-2989-2013>.
- 1019 Li, C., C. McLinden, V. Fioletov, N. Krotkov, S. Carn, J. Joiner, D. Streets, H. He, X. Ren, Z.
1020 Li, R. R. Dickerson, (2017). **India Is Overtaking China as the World's Largest Emitter of**
1021 **Anthropogenic Sulfur Dioxide**, Sci. Rep., 7: 14304, [https://doi.org/10.1038/s41598-017-14639-](https://doi.org/10.1038/s41598-017-14639-8)
1022 [8](https://doi.org/10.1038/s41598-017-14639-8).
- 1023 Li, K., D. J. Jacob, H. Liao, L. Shen, Q. Zhang, K. H. Bates, (2019). **Anthropogenic drivers**
1024 **of 2013–2017 trends in summer surface ozone in China**. Proc. Natl. Acad. Sci. USA, 116:
1025 422-427, <https://doi.org/10.1073/pnas.1812168116>.
- 1026 Li, M., T. Wang, M. Xie, S. Li, B. Zhuang, P. Chen, X. Huang, Y. Han, (2018). **Agricultural**
1027 **fire impacts on ozone photochemistry over the Yangtze River Delta region, East China**, J.
1028 Geophys. Res.-Atmos., 123(12): 6605-6623, <https://doi.org/10.1029/2018JD028582>.
- 1029 Liu, J., D. L. Mauzerall, Q. Chen, Q. Zhang, Y. Song, W. Peng, Z. Klimont, X. Qiu, S. Zhang,
1030 M. Hu, W. Lin, K. R. Smith, T. Zhu, (2016). **Air pollutant emissions from Chinese**
1031 **households: A major and underappreciated ambient pollution source**, P. Natl. Acad. Sci.
1032 USA, 113(28): 7756-7761, <https://doi.org/10.1073/pnas.1604537113>.
- 1033 Luo, M., C. Rinsland, B. Fisher, G. Sachse, G. Diskin, J. Logan, H. Worden, S. Kulawik, G.
1034 Osterman, A. Eldering, R. Herman, M. Shephard, (2007). **TES carbon monoxide validation**
1035 **with DACOM aircraft measurements during INTEX-B 2006**, J. Geophys. Res., 112: D24S48,

1036 <https://dx.doi.org/doi:10.1029/2007JD008803>.

1037 Luo, M., W. Read, S. Kulawik, J. Worden, N. Livesey, K. Bowman, R. Herman, (2013).

1038 **Carbon monoxide (CO) vertical profiles derived from joined TES and MLS measurements,**

1039 J. Geophys. Res.-Atmos., 118(18): 10,601-10,613.

1040 Luo, M., M. W. Shephard, K. E. Cady-Pereira, D. K. Henze, L. Zhu, J. O. Bash, R. W.

1041 Pinder, S. L. Capps, J. T. Walker, and M. R. Jones, (2015). **Satellite observations of**

1042 **tropospheric ammonia and carbon monoxide: Global distributions, regional correlations**

1043 **and comparisons to model simulations.** Atmospheric Environment, 106(0):262–277, 4.

1044 Luo, Y., X. Zheng, T. Zhao, J. Chen, J. (2014). **A climatology of aerosol optical depth over**

1045 **China from recent 10 years of MODIS remote sensing data,** Int. J. Climatol., 34(3): 863-870

1046 <https://doi.org/10.1002/joc.3728>.

1047 Mann, H. B., (1945). **Non-parametric test against trend.** Econometrica 13, 245-259,

1048 <https://doi.org/10.2307/1907187>.

1049 Manoj, M. R., S. K. Satheesh, K. K. Moorthy, M. M. Gogoi, S. S. Babu, (2019). **Decreasing**

1050 **trend in black carbon aerosols over the Indian region,** Geophys. Res. Lett., 46: 2903-2910,

1051 <https://doi.org/10.1029/2018GL081666>.

1052 McClure, C. D., D. A. Jaffe, (2018). **US Particulate Matter Air Quality Improves except**

1053 **in Wildfire-Prone Areas,** P. Natl. Acad. Sci. USA, 115(31): 7901-6,

1054 <https://doi.org/10.1073/pnas.1804353115>.

1055 McDonald B. C., D. R. Gentner, A. H. Goldstein, R. A. Harley, (2013). **Long-term trends in**

1056 **motor vehicle emissions in U.S. urban areas,** Environ. Sci. Technol., 47:10022-10031,

1057 <https://doi.org/10.1021/es401034z>.

1058 Mehta, M., R. Singh, A. Singh, N. Singh, Anshumali, (2016). **Recent global aerosol optical**
1059 **depth variations and trends - A comparative study using MODIS and MISR level 3**
1060 **datasets**, Remote Sensing of Environment, 181: 137-150,
1061 <https://doi.org/10.1016/j.rse.2016.04.004>.

1062 Myhre, G., D. Shindell, F.-M. Bréon, W. Collins, J. Fuglestedt, J. Huang, D. Koch, J.-F.
1063 Lamarque, D. Lee, B. Mendoza, T. Nakajima, A. Robock, G. Stephens, T. Takemura, H. Zhang,
1064 (2014). **Climate Change 2013: The Physical Science Basis**. Contribution of Working Group I
1065 to the Fifth Assessment Report of the Intergovernmental Panel on Climate Change, chapter
1066 Anthropogenic and Natural Radiative Forcing, Cambridge University Press, 659-740.

1067 Novelli, P. C., K. A. Masarie, P. M. Lang, B. D. Hall, R. C. Myers, J. W. Elkins, (2003),
1068 **Reanalysis of tropospheric CO trends: Effects of the 1997–1998 wildfires**, J. Geophys. Res.-
1069 Atmos., 108: 4464, <https://doi.org/10.1029/2002jd003031>.

1070 Pandey A., P. Sadavarte, A. B. Rao, C. Venkataraman, (2014). **Trends in multi-pollutant**
1071 **emissions from a technology-linked inventory for India: II. Residential, agricultural and**
1072 **informal industry sectors**, Atmos. Environ., 99: 341-352,
1073 <https://doi.org/10.1016/j.atmosenv.2014.09.080>.

1074 Platnick, S., M. King, P. Hubanks, (2017). MODIS Atmosphere L3 Monthly Product. NASA
1075 MODIS Adaptive Processing System, Goddard Space Flight Center,
1076 https://doi.org/10.5067/MODIS/MOD08_M3.006

1077 Pommier, M., K.S. Law, C. Clerbaux, S. Turquety, D. Hurtmans, J. Hadji-Lazaro, P.-F.
1078 Coheur, H. Schlager, G. Ancellet, J.-D. Paris, P. Nédélec, G.S. Diskin, J.R. Podolske, J.S.
1079 Holloway, P. Bernath, (2010). **IASI carbon monoxide validation over the Arctic during**
1080 **POLARCAT spring and summer campaigns**, Atmos. Chem. Phys., 10, 10655–10678,

1081 <https://doi.org/10.5194/acp-10-10655-2010>.

1082 Prather, M. J. (2007). **Lifetimes and time scales in atmospheric chemistry**, Philosophical
1083 Transactions of the Royal Society A, 365, 1,705–1,726. <https://doi.org/10.1098/rsta.2007.2040>.

1084 Proestakis, E., V. Amiridis, E. Marinou, A. K. Georgoulas, S. Solomos, S. Kazadzis., J.
1085 Chimot, H. Che, G. Alexandri, I. Biniotoglou, V. Daskalopoulou, K. A. Kourtidis, G. de Leeuw,
1086 R. J. van der A, (2018). **Nine-year spatial and temporal evolution of desert dust aerosols over**
1087 **South and East Asia as revealed by CALIOP**, Atmos. Chem. Phys., 18(2): 1337-1362,
1088 <https://doi.org/10.5194/acp-18-1337-2018>.

1089 Qu, Z., D. K. Henze, C. Li, N. Theys, Y. Wang, J. Wang, W. Wang, J. Han, C. Shim, R. R.
1090 Dickerson, X. Ren, (2019). **SO₂ emission estimates using OMI SO₂ retrievals for 2005–2017**,
1091 *J. Geophys. Res.-Atmos.*, 124, 8336-8359, <https://doi.org/10.1029/2019JD030243>.

1092 Rakitin, V. S., N. F. Elansky, P. Wang, G. Wang, N. V. Pankratova, Y. A. Shtabkin, A. I.
1093 Skorokhod, A. N. Safronov, M. V. Makarova, E. I. Grechko, (2018). **Changes In Trends Of**
1094 **Atmospheric Composition Over Urban And Background Regions Of Eurasia: Estimates**
1095 **Based On Spectroscopic Observations**, Geography, Environment, Sustainability, 11(2): 84-96,
1096 <https://doi.org/10.24057/2071-9388-2018-11-2-84-96>.

1097 Ramanathan, V., G. Carmichael, (2008). **Global and regional climate changes due to black**
1098 **carbon**, Nature Geosci., 1: 221-227, <https://doi.org/10.1038/ngeo156>.

1099 Reuter M., M. Buchwitz, A. Hilboll, A. Richter, O. Schneising, M. Hilker, J. Heymann, H.
1100 Bovensmann, J. P. Burrows (2014). **Decreasing emissions of NO_x relative to CO₂ in East Asia**
1101 **inferred from satellite observations**. Nature Geosci., 7: 792–795,
1102 <https://doi.org/10.1038/ngeo2257>.

1103 Revercomb, H. and L. Strow, (2018). **Suomi NPP CrIS Level 1B Full Spectral Resolution**
1104 **V2**, Accessed from GES DISC February 2019, <https://doi.org/10.5067/9NPOTPIPLMAW>.

1105 Rinsland, C. P., M. Luo, J. A. Logan, R. Beer, H. Worden, S. S. Kulawik, D. Rider, G.
1106 Osterman, M. Gunson, A. Eldering, A. Goldman, M. Shephard, S. A. Clough, C. Rodgers, M.
1107 Lampel, L. Chiou, (2006). **Nadir measurements of carbon monoxide distributions by the**
1108 **Tropospheric Emission Spectrometer instrument onboard the Aura Spacecraft: Overview**
1109 **of analysis approach and examples of initial results**, Geophys. Res. Lett., 33: L22806,
1110 <https://doi.org/10.1029/2006GL027000>.

1111 Sadavarte, P. and C. Venkataraman, (2014). **Trends in multi-pollutant emissions from a**
1112 **technology-linked inventory for India: I. Industry and transport sectors**, Atmos. Environ.
1113 99: 353-364, <https://doi.org/10.1016/j.atmosenv.2014.09.081>.

1114 Sayer, A. M., L. A. Munchak, N. C. Hsu, R. C. Levy, C. Bettenhausen, M. -J. Jeong, (2014).
1115 **MODIS Collection 6 aerosol products: comparison between Aqua's e-Deep Blue, Dark**
1116 **Target, and “merged” data sets, and usage recommendations**, J. Geophys. Res.-Atmos., 119:
1117 13965-13989, <https://doi.org/10.1002/2014JD022453>.

1118 Shine, K. P., J. J. Barnett, W. J. Randel (2008), **Temperature trends derived from**
1119 **Stratospheric Sounding Unit radiances: The effect of increasing CO2 on the weighting**
1120 **function**, Geophys. Res. Lett., 35: L02710, <https://doi.org/10.1029/2007GL032218>.

1121 Schultz, M.G., H. Akimoto, J. Bottenheim, B. Buchmann, I. E. Galbally, S. Gilge, D. Helmig,
1122 H. Koide, A. C. Lewis, P. C. Novelli, C. Plass-Dülmer, T. B. Ryerson, M. Steinbacher, R.
1123 Steinbrecher, O. Tarasova, K. Tørseth, V. Thouret, C. Zellweger, 2015. **The Global Atmosphere**
1124 **Watch reactive gases measurement network**. Elem Sci Anth, 3: p.000067,
1125 <http://doi.org/10.12952>.

- 1126 Sen, P. K., (1968). **Estimates of regression coefficient based on Kendall's tau**, J. Am. Stat.
1127 Assoc., 63: 324
- 1128 Streets, D. G., Q. Zhang, L. Wang, K. He, J. Hao, Y. Wu, Y. Tang, G. R. Carmichael, (2006).
1129 **Revisiting China's CO emissions after the Transport and Chemical Evolution over the**
1130 **Pacific (TRACE-P) mission: Synthesis of inventories, atmospheric modeling, and**
1131 observations. J. Geophys. Res. Atmos., 111(D14), <https://doi.org/10.1029/2006JD007118>.
- 1132 Strode, S. A., H. M. Worden, M. Damon, A. R. Douglass, B. N. Duncan, L. K. Emmons, J.
1133 -F. Lamarque, M. Manyin, L. D. Oman, J. M. Rodriguez, S. E. Strahan, S. Tilmes, (2016).
1134 **Interpreting space-based trends in carbon monoxide with multiple models**, Atmos. Chem.
1135 Phys., 16: 7285-7294, <https://doi.org/10.5194/acp-16-7285-2016>.
- 1136 Strode, S. A., Pawson, S. (2013). **Detection of carbon monoxide trends in the presence of**
1137 **interannual variability**, J. Geophys. Res. Atmos., 118, 12,257-12,273,
1138 <https://doi.org/10.1002/2013JD020258>.
- 1139 Susskind, J., C. D. Barnet and J. M. Blaisdell, (2003). **Retrieval of atmospheric and**
1140 **surface parameters from AIRS/AMSU/HSB data in the presence of clouds**, IEEE Trans.
1141 Geosci. Remote Sens., 41(2): 390-409, <https://doi.org/10.1109/TGRS.2002.808236>.
- 1142 Tang, W., A. F. Arellano, B. Gaubert, K. Miyazaki, H. M. Worden, (2019). **Satellite data**
1143 **reveal a common combustion emission pathway for major cities in China**, Atmos. Chem.
1144 Phys., 19: 4269-4288, <https://doi.org/10.5194/acp-19-4269-2019>.
- 1145 Theil, H., (1950). **A rank invariant method of linear and polynomial regression analysis,**
1146 **i, ii, iii**, Proc. Koninklijke Nederl. Akad. Wet. Ser. A Math. Sci., 53: 1397-1412.
- 1147 Unger, N, D. T. Shindell, D. M. Koch, D. G. Streets, (2006). **Cross influences of ozone and**

1148 **sulfate precursor emissions changes on air quality and climate.** Proc Natl Acad Sci USA.,
1149 103(12): 4377-4380, <https://doi.org/10.1073/pnas.0508769103>.

1150 van der A, R. J., B. Mijling, J. Ding, M. E. Koukouli, F. Liu, Q. Li, H. Mao, N. Theys,
1151 (2017). **Cleaning up the air: effectiveness of air quality policy for SO₂ and NO_x emissions**
1152 **in China**, Atmos. Chem. Phys., 17: 1775-1789, <https://doi.org/10.5194/acp-17-1775-2017>.

1153 van der Werf, G. R., J. T. Randerson, L. Giglio, G. J. Collatz, M. Mu, P. S. Kasibhatla, D. C.
1154 Morton, R. S. DeFries, Y. Jin, Y., T. T. van Leeuwen, (2010). **Global fire emissions and the**
1155 **contribution of deforestation, savanna, forest, agricultural, and peat fires (1997-2009)**,
1156 Atmos. Chem. Phys., 10, 11707–11735, <https://doi.org/10.5194/acp-10-11707-2010>.

1157 Veefkind, J. P., K. F. Boersma, J. Wang, T. P. Kurosu, N. Krotkov, K. Chance, P. F. Levelt,
1158 (2011). **Global satellite analysis of the relation between aerosols and short-lived trace gases**,
1159 Atmos. Chem. Phys., 11, 1255-1267, <https://doi.org/10.5194/acp-11-1255-2011>.

1160 Voss, K. K., A. T. Evan, (2020). **A New Satellite-Based Global Climatology of Dust**
1161 **Aerosol Optical Depth.** *J. Appl. Meteor. Climatol.*, 59: 83-102, [https://doi-](https://doi-org.cuucar.idm.oclc.org/10.1175/JAMC-D-19-0194.1)
1162 [org.cuucar.idm.oclc.org/10.1175/JAMC-D-19-0194.1](https://doi-org.cuucar.idm.oclc.org/10.1175/JAMC-D-19-0194.1)

1163 Wang, S., J. Hao, (2012). **Air quality management in China: Issues, challenges, and**
1164 **options**, J. Environ. Sci., 24: 2-13, [https://doi.org/10.1016/S1001-0742\(11\)60724-9](https://doi.org/10.1016/S1001-0742(11)60724-9).

1165 Wang, Y., J. Wang, (2020). **Tropospheric SO₂ and NO₂ in 2012–2018: Contrasting views**
1166 **of two sensors (OMI and OMPS) from space**, Atmospheric Environment, 223, 117214,
1167 <https://doi.org/10.1016/j.atmosenv.2019.117214>.

1168 Warner, J. X., M. McCourt Comer, C. Barnet, W. W. McMillan, W. Wolf, E. Maddy, G.
1169 Sachse, (2007). **A Comparison of Satellite Tropospheric Carbon Monoxide Measurements**

- 1170 **from AIRS and MOPITT During INTEX-NA**, *J. Geophys. Res.*, 112: D12S1,
1171 <https://doi.org/10.1029/2006JD007925>.
- 1172 Warner, J. X., Z. Wei, L. L. Strow, C. D. Barnet, L. C. Sparling, G. Diskin, G. Sachse, (2010).
1173 **Improved Agreement of AIRS Tropospheric Carbon Monoxide Products with other EOS**
1174 **Sensors Using Optimal Estimation Retrievals**, *Atmos. Chem. Phys.*, 10: 9521–9533,
1175 <https://doi.org/10.5194/acp-10-9521-2010>.
- 1176 Weatherhead, E. C., G. C. Reinsel, G. C. Tiao, X.-L. Meng, D. Choi, W.-K. Cheang, T. Keller,
1177 J. DeLuisi, D. J. Wuebbles, J. B. Kerr, A.J. Miller, S. J. Oltmans, J. E. Frederick, (1998), **Factors**
1178 **affecting the detection of trends: Statistical considerations and applications to**
1179 **environmental data**, *J. Geophys. Res.*, 103(D14), 17149- 17161,
1180 <https://doi.org/10.1029/98JD00995>.
- 1181 Wei, J., Y. Peng, J. Guo, L. Sun, (2019a). **Performance of MODIS Collection 6.1 Level 3**
1182 **aerosol products in spatial-temporal variations over land**, *Atmos. Environ.*, 206: 30-44,
1183 <https://doi.org/10.1016/j.atmosenv.2019.03.001>.
- 1184 Wei, J., Y. Peng, R. Mahmood, L. Sun, J. Guo, (2019b). **Intercomparison in spatial**
1185 **distributions and temporal trends derived from multi-source satellite aerosol products**,
1186 *Atmos. Chem. Phys.*, 19: 7183-7207, <https://doi.org/10.5194/acp-19-7183-2019>.
- 1187 Witek, M. L., D. J. Diner, M. J. Garay (2016), **Satellite assessment of sea spray aerosol**
1188 **productivity: Southern Ocean case study**, *J. Geophys. Res. Atmos.*, 121: 872–894,
1189 <https://doi.org/10.1002/2015JD023726>.
- 1190 Worden, H. M., M. N. Deeter, C. Frankenberg, M. George, F. Nichitiu, J. Worden, I. Aben, K.
1191 W. Bowman, C. Clerbaux, P. F. Coheur, A. T. J. de Laat, R. Detweiler, J. R. Drummond, D. P.
1192 Edwards, J. C. Gille, D. Hurtmans, M. Luo, S. Martínez-Alonso, S. Massie, G. Pfister, J. X.

- 1193 Warner, (2013). **Decadal Record of Satellite Carbon Monoxide Observations**, Atmos. Chem.
1194 Phys. 13: 837–50, <https://doi.org/10.5194/acp-13-837-2013>.
- 1195 Worden, J., X. Liu, K. Bowman, K. Chance, R. Beer, A. Eldering, M. Gunson, H. Worden
1196 (2007). **Improved tropospheric ozone profile retrievals using OMI and TES radiances**.
1197 Geophys. Res. Lett., 34: L01809, <https://doi.org/10.1029/2006GL027806>.
- 1198 Wu, Y., Y. Han, A. Voulgarakis, T. Wang, M. Li, Y. Wang, M. Xie, B. Zhuang, S. Li, (2017).
1199 **An agricultural biomass burning episode in eastern China: Transport, optical properties,**
1200 **and impacts on regional air quality**, J. Geophys. Res.-Atmos., 122(4): 2304-2324,
1201 <https://doi.org/10.1002/2016JD025319>.
- 1202 Yang, H., D. W. Waugh, C. Orbe, P. K. Patra, P. Jöckel, J. -F. Lamarque, S. Tilmes, D.
1203 Kinnison, J. W. Elkins, E. J. Dlugokencky, (2019). **Evaluating simulations of interhemispheric**
1204 **transport: Interhemispheric exchange time versus SF6 age**, Geophysical Research Letters,
1205 46: 1113-1120, <https://doi.org/10.1029/2018GL080960>.
- 1206 Yin, Y., F. Chevallier, P. Ciais, G. Broquet, A. Fortems-Cheiney, I. Pison, M. Saunois, (2015).
1207 **Decadal Trends in Global CO Emissions as Seen by MOPITT**, Atmos. Chem. Phys. Discuss.,
1208 15 (10): 14505-47. <https://doi.org/10.5194/acpd-15-14505-2015>.
- 1209 Yoon, J., A. Pozzer, P. Hoor, D. Y. Chang, S. Beirle, T. Wagner, S. Schloegl, J. Lelieveld, H.
1210 M. Worden, (2013). **Technical Note: Temporal change in averaging kernels as a source of**
1211 **uncertainty in trend estimates of carbon monoxide retrieved from MOPITT**, Atmos. Chem.
1212 Phys., 13: 11307-11316, <https://doi.org/10.5194/acp-13-11307-2013>.
- 1213 Zeng, G., S. W. Wood, O. Morgenstern, N. B. Jones, J. Robinson, D. Smale (2012). **Trends**
1214 **and variations in CO, C₂H₆, and HCN in the Southern Hemisphere point to the declining**
1215 **anthropogenic emissions of CO and C₂H₆**, Atmos. Chem. Phys., 12: 7543-7555,

1216 <https://doi.org/10.5194/acp-12-7543-2012>.

1217 Zhang, X., J. Liu, H. Han, Y. Zhang, Z. Jiang, H. Wang, L. Meng, Y. C. Li, Y. Liu, (2020).

1218 **Satellite-Observed Variations and Trends in Carbon Monoxide over Asia and Their**

1219 **Sensitivities to Biomass Burning**, *Remote Sens.*, 12, 830, <https://doi.org/10.3390/rs12050830>.

1220 Zheng, B., D. Tong, M. Li, F. Liu, C. Hong, G. Geng, H. Li, X. Li, L. Peng, J. Qi, L. Yan, Y.

1221 Zhang, H. Zhao, Y. Zheng, K. He, Q. Zhang, (2018a). **Trends in China's anthropogenic**

1222 **emissions since 2010 as the consequence of clean air actions**, *Atmos. Chem. Phys.*, 18: 14095-

1223 14111, <https://doi.org/10.5194/acp-18-14095-2018>

1224 Zheng, B., F. Chevallier, P. Ciais, Y. Yin, M. N. Deeter, H. M. Worden, Y. Wang, Qiang

1225 Zhang, K. He, (2018b). **Rapid decline in carbon monoxide emissions and export from East**

1226 **Asia between years 2005 and 2016**, *Environ. Res. Lett.*, 13(4): 044007,

1227 <https://doi.org/10.1088/1748-9326/aab2b3>.

1228 Zheng, B., F. Chevallier, Y. Yin, P. Ciais, A. Fortems-Cheiney, M. N. Deeter, R. J. Parker, Y.

1229 Wang, H. M. Worden, Y. Zhao (2019). **Global atmospheric carbon monoxide budget 2000–**

1230 **2017 inferred from multi-species atmospheric inversions**, *Earth Syst. Sci. Data*, 11: 1411-

1231 1436, <https://doi.org/10.5194/essd-11-1411-2019>.

1232 **List of Figure Captions:**

1233 Fig 1. Zonal average plot of monthly average (a) MOPITT column CO and (b) MODIS AOD.

1234 Percent anomalies in (c) MOPITT CO and (d) MODIS AOD. Percent anomalies are calculated
1235 relative to the climatological month averages within each 2° zonal average box. White stripes in
1236 panel a and c during 2001 and 2009 represent missing MOPITT data due to instrumental
1237 diagnostic operations. White pixels at NH and SH high latitudes represent missing data for both
1238 instruments due to polar night.

1239 Fig 2: Global average (a) column CO and (b) AOD between 2000 and 2018. Boxes outline the
1240 sub-regions used for regional trend analysis, numbered 1 to 19, discussed in section 3.4. Trends
1241 in (c) CO from MOPITT and (d) AOD from MODIS between 2002 and 2018, gridded to 2°x4°.

1242 Fig 3: Residual trend in CO columns from MOPITT calculated relative to the global average
1243 trend (-0.5% per year, +/- 60°) from 2002 to 2018.

1244 Fig 4: Multi-instrument time series of month average X_{CO} for (a) NH (0° to 60°N) and (b) SH
1245 (60°S to 0°). Lower panels show the monthly anomalies relative to each dataset mean annual
1246 cycle, for (c) NH and (d) SH. Weighted least squares trends on the anomalies are indicated with
1247 standard error in percent per year for MOPITT and AIRS. The grey dashed line is the zero line
1248 for reference.

1249 Region numbers correspond with numbers in Table 2 and Figure 2. Vertical bars are monthly
1250 standard deviation. General tendencies from linear regression (WLS) are shown for the whole
1251 record (July 2002-June 2018, dotted line), as well as the 1st half and 2nd half of the record (solid
1252 lines). Slope values are described in Table 2.

1253 Fig 6: Regional time series of X_{CO} (red) and AOD (blue) over (a) Maritime Southeast Asia and
1254 (b) the northwest USA example fire-prone regions. Vertical bars are monthly standard deviation.
1255 General tendencies from linear regression (WLS) are shown for July 2002-June 2018 (dotted

1256 line), as well as the 1st and 2nd half of the record (solid lines). Slope values are described in
1257 Table 2.

1258 Fig 7: Arrays of quantile trend analysis for monthly CO data for different regions: (a) Northeast
1259 China, (b) Eastern USA, and (c) Northwest USA. Trends are shown as circles colored by percent
1260 per year, which is calculated relative to the regional mean column average VMR. The Mann-
1261 Kendall p-value is indicated by the size of the circle. Trends by month for January to December
1262 travel up the page, and trends on annual average values are shown in the bottom row for
1263 comparison. Month average column average VMR is displayed as colored squares on the LHS
1264 with size of the square denoting coefficient of variation (σ/μ). The mean number of retrievals (n)
1265 within a month are displayed on the RHS, in amounts of thousands (K).

1266 Fig 8: Same as Fig 7, but for (a) NH and (b) SH.

1267 Fig A1: MOPITT a priori total column X_{CO} for month averages (top row) and daily averages
1268 (bottom row) comparing October 2002 with October 2018. Note that daily dates were chosen to
1269 display the same MOPITT orbital swaths. The square black box is the Northeast China industrial
1270 region of interest for this study and average X_{CO} within this region is noted on each plot.

1271 Fig A2: Changes in MOPITT monthly mean total column CO and standard error as a function of
1272 sub-sampling reduction factor (2^n). Top three plots show results for NH June 2007 and bottom
1273 three plots show NH December 2007.

1274 Fig A3: Time series of degrees of freedom of signal (DFS) for MOPITT in the NH and SH.

1275 Fig A4: Autocorrelation coefficients in monthly CO residuals for the Northern Hemisphere full
1276 timeseries (left) and autocorrelation for an AR(1) model with $\phi = 0.83$ (right). Blue shaded area
1277 shows the confidence intervals for $p=0.01$.

1278 Fig A5: Autocorrelation coefficients in monthly January residual values for the Northern
1279 Hemisphere. Blue shaded area shows the confidence intervals for $p= 0.01$.

1280 Fig C1: Trend standard error (top) and significance - calculated trend relative to std err (bottom).
1281 Fig C2: Trends in AOD from Aqua/MODIS between 2002 and 2018, gridded to $2^{\circ} \times 4^{\circ}$.
1282 Fig C3: Dataset average annual cycles in month average X_{CO} (red) and AOD (blue) for the
1283 different regions. Region numbers correspond with regions in Fig. 2 and names in Table 2.
1284 Fig C4: Gridded arrays of quantile trend analysis for monthly data for different regions. Trends
1285 are shown as circles colored by percent per year, which is calculated relative to the regional
1286 mean column average VMR. The Mann-Kendall p-value is indicated by the size of the circle.
1287 Trends in annual mean values are shown for comparison in the bottom row. Month average
1288 column average VMR along with the coefficient of variation are displayed as colored squares on
1289 the LHS. The mean number of retrievals (n) within a month are displayed on the RHS, in
1290 amounts of thousands (K).
1291

1292 **List of Equations in LaTeX code:**

1293 Equation 1:

```
1294 \begin{equation}
1295 y=mt + b + \epsilon(t)
1296 \end{equation}
```

1297

1298 Equation 2:

```
1299 \begin{equation}
1300 m=\frac{\sum\limits_{i=1}^n\frac{1}
1301 {\sigma_i^2}\sum\limits_{i=1}^n\frac{t_{iy_i}}{\sigma_i^2} -
1302 \sum\limits_{i=1}^n\frac{t_i}
1303 {\sigma_i^2}\sum\limits_{i=1}^n\frac{y_i}{\sigma_i^2}}
1304 {\sum\limits_{i=1}^n\frac{1}
1305 {\sigma_i^2}\left(\sum\limits_{i=1}^n\frac{t_i^2}
1306 {\sigma_i^2}-\left(\sum\limits_{i=1}^n\frac{t_i}
1307 {\sigma_i^2}\right)^2\right)}
1308 \end{equation}
```

1309

1310 Equation 3:

```
1311 \begin{equation}
1312 m= \widetilde{\left(\frac{y_j-y_i}{t_j-t_i}\right)}
1313 \end{equation}
```

1314

1315 Equation A2:

```
1316 \begin{equation}
1317 \sigma_m \approx \frac{\sigma_\epsilon}{N^{3/2}}\sqrt{\frac{1 + \phi}
1318 {1 - \phi}}
1319 \end{equation}
```

1320

1321

1322 **Appendix A. Uncertainties in MOPITT CO trend analysis**

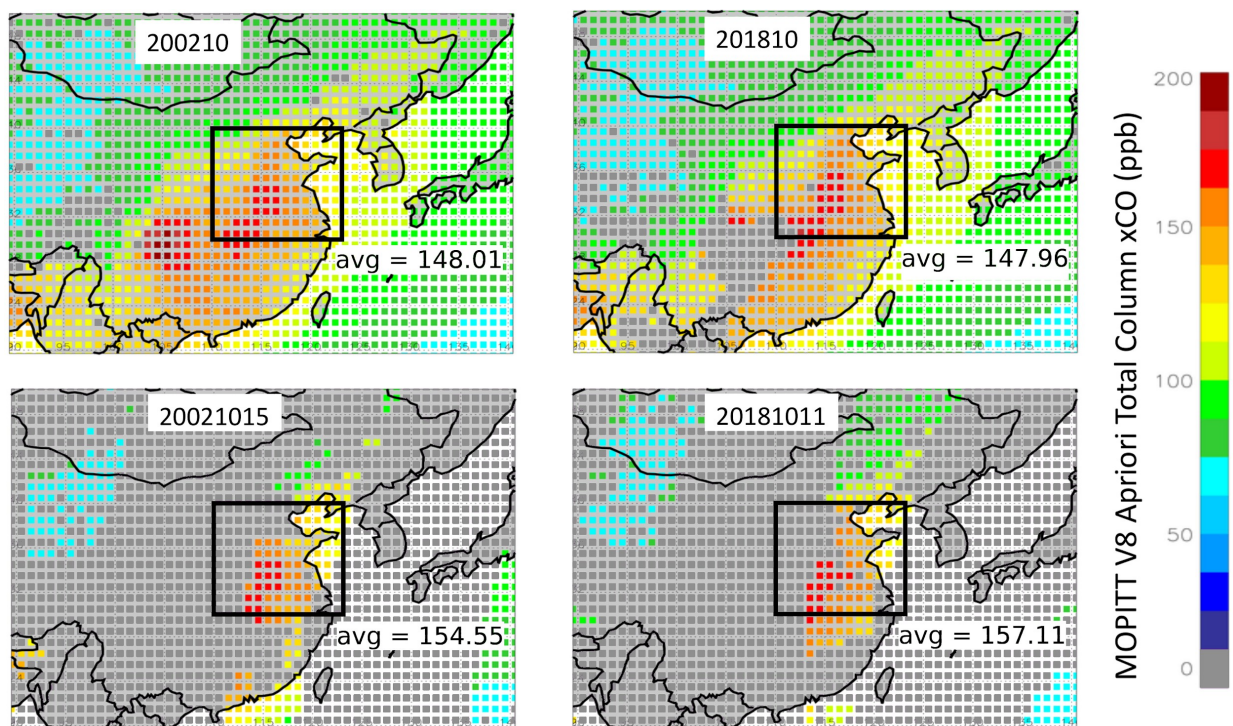
1323 Uncertainties due to the instrument system are investigated in this section. Systematic and
1324 random sampling uncertainty is assessed by determining trends in a priori and using bootstrap
1325 sampling, respectively. Systematic uncertainties due to instrument sensitivity changes are
1326 investigated using the averaging kernels.

1327 **A1 Sampling bias**

1328 **A1.1 Approximating systematic sampling uncertainty**

1329 Sampling changes may occur for the satellite instrument over time, for example, changes due to
1330 physical scene differences such as from cloud screening. Fig A1 shows how sampling differences
1331 on different days and months can affect the mean values in MOPITT a priori, which are taken
1332 from climatology and have no interannual variability. Differences can be seen in the $1^{\circ}\times 1^{\circ}$
1333 gridboxes containing no data (gray) as well as differences in some gridbox colors. For instance,
1334 October 2018 sees persistent clouds over central southern China which is not the case in 2002.
1335 These differences are only due to how the a priori was sampled, corresponding with each
1336 MOPITT observation. While we do not necessarily expect changes in sampling over time, we
1337 use trend analysis on the sampled a priori values to approximate the impact of any systematic
1338 sampling changes within each region. This could be of particular importance for regions with
1339 large CO spatial variability, such as China.

1340



1341 Fig A1: MOPITT a priori total column X_{CO} for month averages (top row) and daily averages

1342 (bottom row) comparing October 2002 with October 2018. Note that daily dates were chosen to

1343 display the same MOPITT orbital swaths. The square black box is the Northeast China industrial

1344 region of interest for this study and average X_{CO} within this region is noted on each plot.

1345

1346 Trends are calculated in the same way as the main text using a priori anomalies and WLS,

1347 weighted by monthly standard deviation within each region (Table A1.1). We also perform Theil-

1348 Sen analysis on year average a priori anomalies from 2002-2018 to determine trend consistency.

1349 Overall, we find no significant trends in the sampled a priori for any of the regions or time

1350 periods. Thus, we can be confident that changes in sampling are not contributing to the trend

1351 analysis performed in the main text.

1352

1353

1354

1356 Table A1.1: Summary of WLS trends in the a priori X_{CO} anomalies for the 19 regions, shown for
 1357 different time periods. Theil Sen trends are also shown for the full time series. Yellow
 1358 backgrounds denote no significant trend for WLS analysis, relative to the slope standard error.
 1359 Orange background indicates $p > 0.05$ in Theil-Sen trends.

	Theil-Sen (p)	WLS Trend % per year (\pm standard error)		
	CO			
	2002-2018	Full July 2002- June 2018	1st half July 2002- June 2010	2nd half July 2010- June 2018
Industrial				
1. NE China	-0.005 (0.84)	0.031 (0.07)	0.07 (0.2)	0.09 (0.2)
2. N India	-0.033 (0.59)	-0.02 (0.1)	0.09 (0.3)	-0.11 (0.3)
3. Europe	-0.006 (0.65)	-0.001 (0.03)	-0.06 (0.1)	0.072 (0.09)
4. E USA	-0.004 (0.71)	0.0003 (0.03)	-0.005 (0.1)	0.02 (0.1)
Fire-prone				
5. NW USA	0.004 (0.59)	0.001 (0.02)	-0.014 (0.07)	0.013 (0.06)
6. NW Canada	-0.0008 (0.90)	-0.0028 (0.006)	0.002 (0.02)	-0.020 (0.02)
7. Siberia	-0.004 (0.71)	-0.012 (0.01)	0.019 (0.03)	-0.001 (0.04)
8. Russia	-0.007 (0.34)	-0.012 (0.05)	-0.01 (0.1)	-0.02 (0.1)
9. Cent. America	0.004 (0.15)	0.005 (0.03)	0.021 (0.08)	-0.002 (0.08)
10. S America	-0.006 (0.97)	0.02 (0.2)	-0.07 (0.5)	0.05 (0.5)
11. SAm Tspt BB	0.002 (0.59)	0.001 (0.04)	-0.01 (0.1)	-0.002 (0.1)
12. Central Africa	-0.001 (0.97)	-0.016 (0.06)	-0.01 (0.2)	0.06 (0.2)
13. Southern Africa	-0.001 (0.97)	0.002 (0.09)	-0.11 (0.2)	0.03 (0.2)
14. SAf Tspt	-0.004 (0.90)	-0.01 (0.1)	0.08 (0.3)	-0.03 (0.4)
15. Maritime SEA	0.014 (0.48)	0.02 (0.1)	0.11 (0.4)	-0.01 (0.4)
16. NW Australia	-0.001 (0.90)	0.011 (0.03)	0.04 (0.1)	0.01 (0.1)
17. E Australia	0.002 (0.59)	0.006 (0.08)	0.01 (0.2)	0.02 (0.2)
Background				
18. NH (0 to 60)	-0.002 (0.59)	-0.001 (0.07)	0.01 (0.2)	0.01 (0.2)
19. SH (-60 to 0)	-0.003 (0.54)	0.001 (0.2)	-0.02 (0.7)	0.01 (0.7)

1360

1361

1362 **A1.2 Approximating random sampling uncertainty**

1363 We estimate random sampling errors in our trend estimate by resampling MOPITT CO within
1364 regions using the bootstrap method of resampling with replacement (Efron, 1979) following the
1365 implementation of Reuter et al. (2014) and Jiang et al. (2018). This procedure randomly creates
1366 one hundred resampled datasets, to produce an ensemble of trends from which we calculate a
1367 mean trend and standard deviation.

1368

1369 Specifically, the method proceeds as follows: beginning with a given MOPITT level 2 dataset for
1370 a particular month and region, which contains N retrievals within the region, we construct a
1371 resampled dataset of N points by uniformly sampling the original data, with replacement.

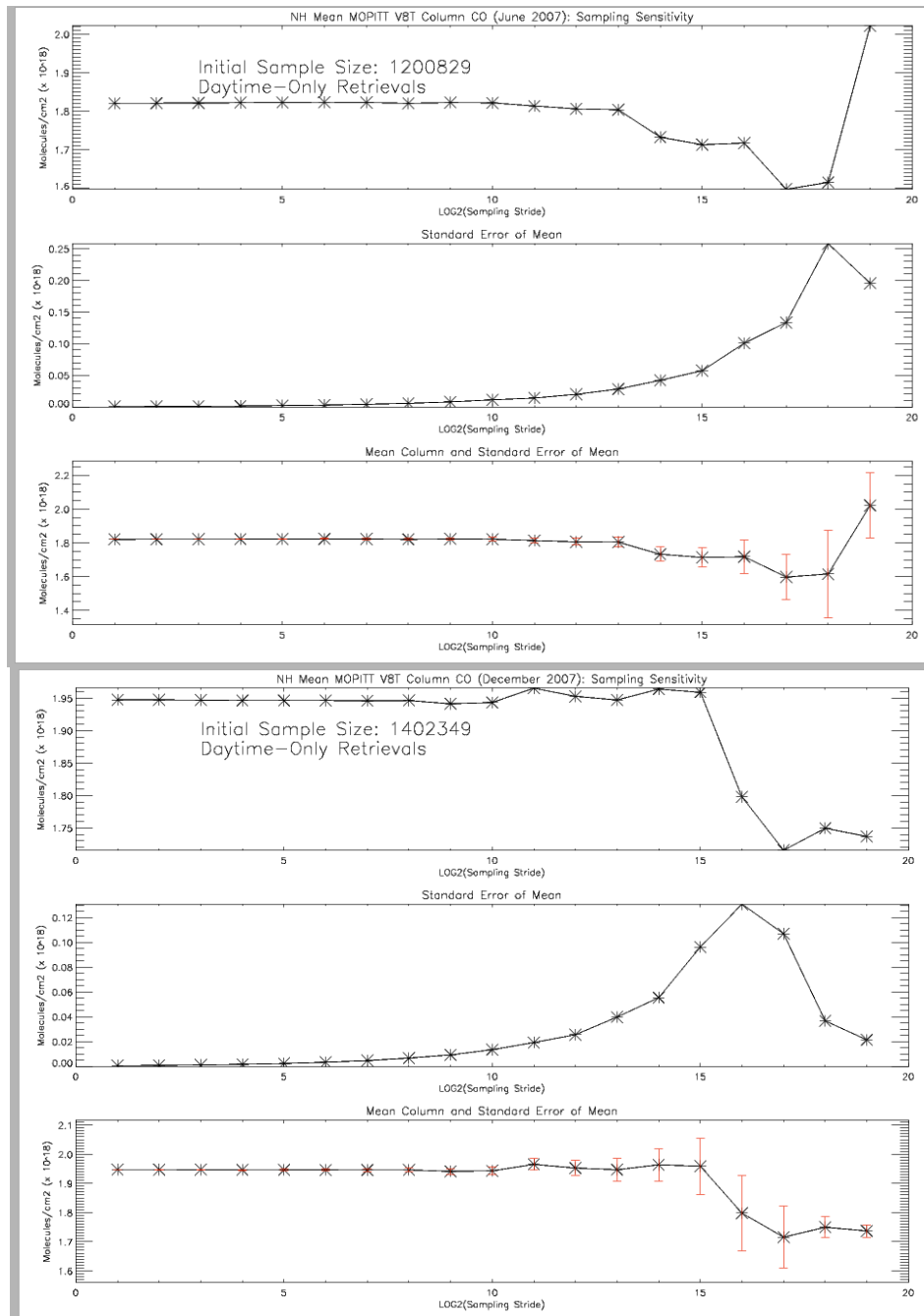
1372 Consequently, there may be multiples of some of the original data within a resampled dataset;
1373 there may also be values in the original dataset that do not appear in the resampled dataset. This
1374 method effectively randomly increases (multiples) and decreases (left out) the weight of
1375 retrievals when contributing to the region mean. Regional means and standard deviation are
1376 calculated from the resampled dataset and time series of monthly means with corresponding
1377 standard deviations are built. We repeat this resampling process on the original data one hundred
1378 times to create an ensemble of one hundred time series, and in turn an ensemble of one hundred
1379 fitted trends for each region. Finally, we calculate a mean trend and a standard deviation over the
1380 ensemble. The standard deviation of the resampled slopes is our measure of the trend uncertainty
1381 due to resampling, which is summarized for all regions over 2002-2018 in Table A3.1.

1382

1383 We have also tested the extent to which MOPITT data can be sub-sampled and still provide
1384 equivalent mean monthly values for the total column. Figure A2 shows that selecting every 2⁸

1385 retrieval within the NH still gives the same values for the monthly mean CO column with
 1386 acceptable standard error. These results informed the sub-sampling used for CrIS data processing
 1387 with the MUSES algorithm.

1388

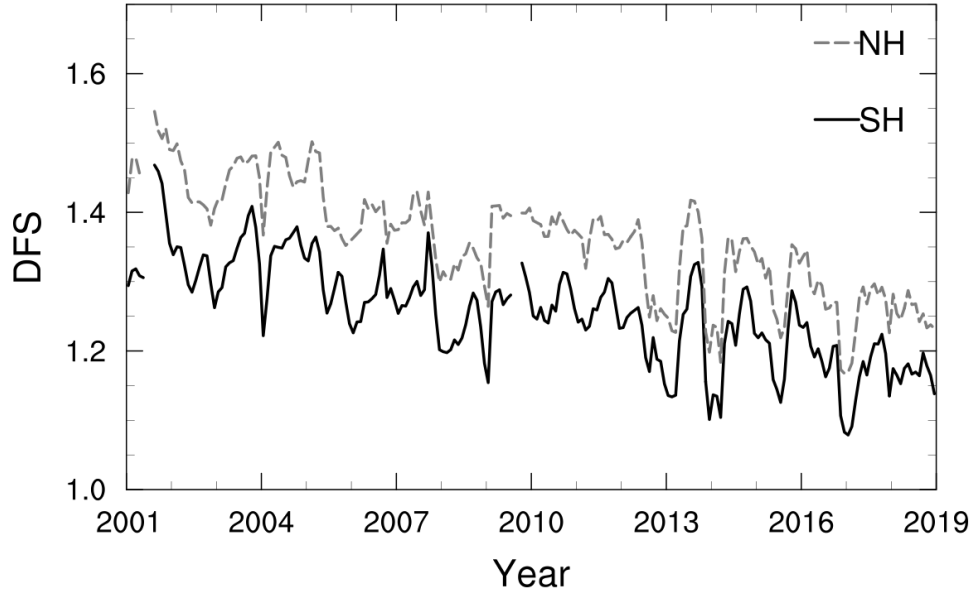


1389

1390 FigA2: Changes in MOPITT monthly mean total column CO and standard error as a function of
 1391 sub-sampling reduction factor (2^n). Top three plots show results for NH June 2007 and bottom
 1392 three plots show NH December 2007.

1393 **A2 Systematic uncertainty due to MOPITT sensitivity changes**

1394 Sampling may also be affected by changes in instrumental sensitivity, such as through
1395 degradation of the instrument over time. Some of this degradation of performance is known (e.g.
1396 cell gas loss) and is accounted for in the retrieval algorithm. Additionally, MOPITT retrieval
1397 sensitivity is related to the amount of atmospheric trace gas, so it would be expected to decline as
1398 CO concentrations decline, similar to changes in sensitivity for satellite temperature retrievals
1399 with increasing CO₂ (Shine et al., 2008). Sensitivity changes will be reflected in the instrument
1400 averaging kernels (AK). The degrees of freedom for signal (DFS) is a measure derived from the
1401 AK. Yoon et al. (2013), show that time varying AKs add uncertainty to trend analysis in
1402 MOPITT surface retrievals and Strode et al. (2016) found that MOPITT AKs impacted simulated
1403 trends. We examine the hemispheric DFS over time (Fig A3) and find trend behavior that
1404 suggests we should quantify the impact of sensitivity changes on trend analysis for column
1405 values. The decreasing trend in DFS corresponds with an increase in instrument noise (Deeter et
1406 al., 2015), whereby changes in instrument signals contribute to a trend in the DFS. However,
1407 although the DFS shows a strong trend over 2001-2018, we do not expect large impacts on X_{CO}
1408 trends because the DFS values remain above 1, and consequently enough information is
1409 available to retrieve column amounts.



1410

1411 Fig A3: Time series of degrees of freedom of signal (DFS) for MOPITT in the NH and SH.

1412

1413 To test the impact of sensitivity changes on X_{CO} we create a global climatology from reanalysis
 1414 (Gaubert et al., 2016, Gaubert et al., 2017b), and convolve with the MOPITT monthly level-3
 1415 AKs and a priori (Eq. 1), before calculating regional averages and standard deviation and
 1416 performing trend analysis. The MOPITT AKs are changing in time, while the climatology has no
 1417 interannual variability. As we saw in Appendix A1.1, the a priori have no significant trends.
 1418 Therefore, any trends found in the smoothed climatology are a result of sensitivity changes.

1419

$$1420 \quad \text{col_vmr_smooth} = (c_a + A(x_r - x_a))/c_d \quad (\text{Eq. A1})$$

1421

1422 Where:

1423 col_vmr_smooth = smoothed climatology column average vmr

1424 c_a = MOPITT a priori column

1425 A = MOPITT column averaging kernel

1426 x_r = reanalysis profile in $\log(\text{vmr})$

1427 x_a = MOPITT a priori profile in $\log(\text{vmr})$

1428 c_d = MOPITT reported column of dry air

1429

1430 Trends on the smoothed reanalysis climatology for each region and time period are shown in
1431 Table A2.1, which have been calculated on anomalies with WLS in the same way as trends in the
1432 main text, weighted by regional monthly standard deviation in the smoothed data. We also
1433 perform Theil-Sen analysis on year average values from 2002-2018. Some regions show
1434 significant trends in the smoothed reanalysis, meaning that instrument sensitivity could have
1435 impacted the trend analysis performed in the main text. Significant trends with $p < 0.05$ for the
1436 Theil-Sen analysis are generally consistent with the trends that are outside one standard error in
1437 the WLS slope.

1438

1439 In particular, the full time series analysis over Northeast China, Europe and Eastern USA, as well
1440 as full and shorter time periods for the NH boreal fire-prone regions and Maritime SEA may
1441 have been impacted by instrument sensitivity. In most of these regions the impact is small
1442 compared to the trend in X_{CO} , however the uncertainty has been noted in section 3.4 as a
1443 systematic error. When reported as systematic errors, they impact the trend in the opposite
1444 direction as shown in Table A2.1. For example, we see a slightly positive trend (+0.145% per
1445 year) in the smoothed reanalysis for China over 2002-2018 that indicates some of the observed
1446 negative trends could be counteracted by instrument sensitivity. Therefore, we report a
1447 systematic error of -0.145 % per year for this effect on the regional trend.

1448

1449

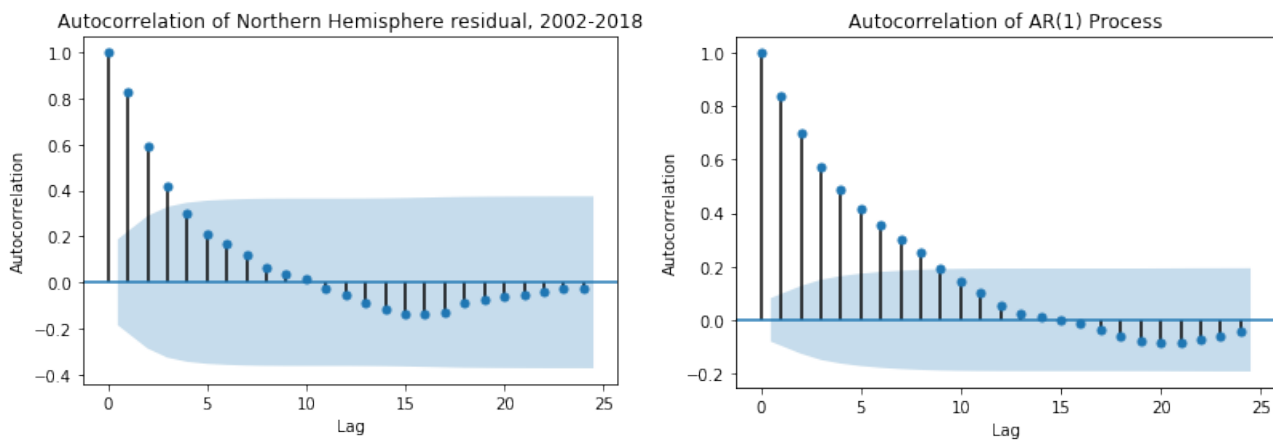
1450 Table A2.1: Summary of estimated CO trends due to changes in MOPIT sensitivity. WLS trends
 1451 in the anomalies of smoothed reanalysis climatology from the 19 regions are shown with
 1452 standard error over the full, 1st half and 2nd half time periods. Theil Sen trends are also shown
 1453 for the full time series. Red background colors denote positive trends, blue denote negative
 1454 trends and yellow background denote no trend for WLS analysis. Orange background indicates
 1455 $p > 0.05$ for Theil-Sen.

	Theil-Sen (p)	WLS Trend % per year (\pm standard error)		
	CO			
	July 2002- June 2018	Full July 2002- June 2018	1st half July 2002- June 2010	2nd half July 2010- June 2018
Industrial				
1. NE China	0.125 (0.0001)	0.145 (0.07)	0.18 (0.2)	0.12 (0.2)
2. N India	0.016 (0.65)	0.04 (0.1)	0.20 (0.4)	0.02 (0.3)
3. Europe	-0.041 (0.02)	-0.047 (0.02)	-0.040 (0.07)	-0.031 (0.07)
4. E USA	0.024 (0.23)	-0.032 (0.02)	0.024 (0.06)	-0.014 (0.06)
Fire-prone				
5. NW USA	-0.063 (0.001)	-0.079 (0.04)	-0.14 (0.1)	-0.072 (0.1)
6. NW Canada	-0.058 (0.003)	-0.0403 (0.007)	-0.049 (0.02)	-0.032 (0.02)
7. Siberia	-0.030 (0.02)	-0.007 (0.01)	0.031 (0.03)	0.031 (0.03)
8. Russia	-0.095 (1.5e-05)	-0.065 (0.03)	-0.104 (0.07)	-0.122 (0.07)
9. Cent. America	-0.003 (0.77)	0.018 (0.03)	0.070 (0.09)	0.014 (0.09)
10. S America	0.105 (0.003)	0.05 (0.1)	0.05 (0.3)	0.09 (0.4)
11. SAm Tspt BB	-0.046 (0.02)	-0.013 (0.08)	-0.02 (0.2)	0.003 (0.2)
12. Central Africa	0.002 (0.84)	0.013 (0.03)	0.02 (0.08)	0.036 (0.09)
13. Southern Africa	-0.016 (0.30)	-0.04 (0.1)	-0.07 (0.3)	-0.02 (0.3)
14. SAf Tspt	-0.001 (1)	-0.008 (0.06)	0.06 (0.2)	-0.05 (0.2)
15. Maritime SEA	0.157 (0.02)	0.135 (0.06)	0.22 (0.2)	0.07 (0.2)
16. NW Australia	-0.005 (0.84)	0.004 (0.03)	0.02 (0.1)	-0.045 (0.09)
17. E Australia	-0.029 (0.13)	-0.001 (0.09)	0.004 (0.3)	0.011 (0.2)
Background				
18. NH (0 to 60)	-0.037 (0.006)	-0.01 (0.1)	-0.0003 (0.3)	-0.01 (0.3)
19. SH (-60 to 0)	-0.019 (0.06)	-0.01 (0.2)	-0.05 (0.6)	0.006 (0.6)

1456

1457 A3 Accounting for Autocorrelation

1458 Autocorrelation in the noise ($\epsilon(t)$ of Equation 1) may impact the precision of the slope
 1459 calculations. We determine autocorrelation in our monthly timeseries by performing ACF
 1460 analysis in the residuals. Residuals generally show autocorrelation indicative of an first-order
 1461 autoregressive, AR(1), model process. For example, the autocorrelation function for CO in the
 1462 Northern Hemisphere (NH) region is shown in Fig A4, and is similar to an AR(1) model example
 1463 with the equivalent coefficient (ϕ).



1464 Fig A4: Autocorrelation coefficients in monthly CO residuals for the Northern Hemisphere full
 1465 timeseries (left) and autocorrelation for an AR(1) model with $\phi = 0.83$ (right). Blue shaded area
 1466 shows the confidence intervals for $p=0.01$.

1467

1468 Consequently, we compensate for an AR(1) noise process by adjusting the standard error to
 1469 account for autocorrelation. According to Weatherhead et al. (1998) the standard error in the
 1470 slope (σ_m) can be accurately approximated by the standard deviation in the noise (σ_ϵ), combined
 1471 with a scaling factor based on the autocorrelation coefficient at lag-1, ϕ :

$$\sigma_m \approx \frac{\sigma_\epsilon}{N^{3/2}} \sqrt{\frac{1 + \phi}{1 - \phi}} \quad (\text{A2})$$

1473 where N is the number of years of data (Weatherhead et al., 1998, equation 2).

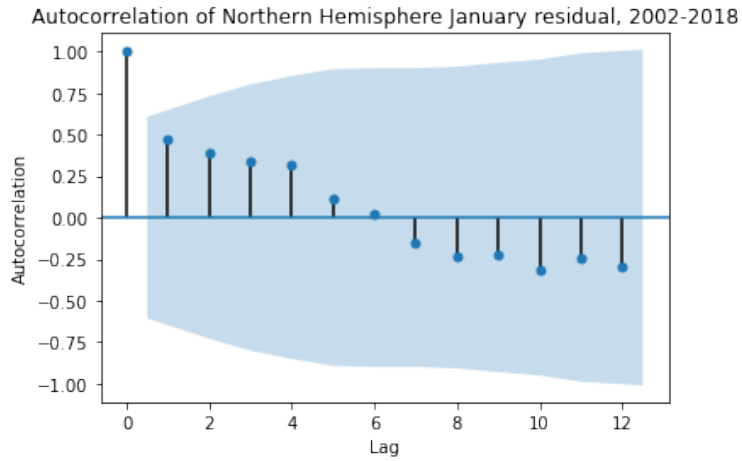
1474

1475 We investigate autocorrelation in the residual for all regions and where it is found to be
 1476 significant outside the 99 % confidence intervals, we calculate the standard errors according to
 1477 equation A2 and collect the results in Table A3.1. The estimated standard error on the slope
 1478 from equation A2 was compared with the WLS standard error and was found to be of
 1479 approximate similar magnitude, and generally smaller than the WLS estimate, but sometimes
 1480 larger. Therefore, as a conservative estimate of the standard error on the slope, we retain the
 1481 larger of the two estimates in the main section of the manuscript.

1482

1483 The Theil-Sen trend estimates in Section 4.2 do not require compensation for autocorrelation in
 1484 the noise, because consecutive values are separated by a year and CO has about a 2 month
 1485 atmospheric lifetime, meaning persistence is not significant. For example, the residuals for
 1486 January trend analysis in the NH region show no autocorrelation (Figure A5), even though the
 1487 NH full timeseries showed the largest autocorrelation coefficient ($\phi = 0.83$) of all datasets.
 1488 Similarly, no significant autocorrelation in the residuals was found in other regions when trend
 1489 analysis is completed in months across different years.

1490



1491 Fig A5: Autocorrelation coefficients in monthly January residual values for the Northern
1492 Hemisphere. Blue shaded area shows the confidence intervals for $p= 0.01$.

1493 Table A3.1: Standard error estimate on the slope accounting for autocorrelation. Yellow
 1494 background indicates higher errors than the WLS estimate.

	Trend % per year (\pm standard error + systematic error)					
	CO			AOD		
	Full July 2002- June 2018	1st half July 2002- June 2010	2nd half July 2010- June 2018	Full July 2002- June 2018	1st half July 2002- June 2010	2nd half July 2010- June 2018
Industrial						
1. NE China	0.1	0.4	0.3	0.4	NS	NS
2. N India	0.1	0.2	0.3	0.3	1.1	0.8
3. Europe	0.1	NS	0.3	NS	NS	0.9
4. E USA	0.1	0.3	0.4	0.6	1.7	1.5
Fire-prone						
5. NW USA	0.1	0.3	0.4	0.6	NS	2.7
6. NW Canada	0.1	0.4	0.3	NS	NS	NS
7. Siberia	0.2	0.6	0.5	1.0	3.6	NS
8. Russia	0.1	0.3	0.3	0.4	0.7	0.7
9. Central America	0.1	0.3	0.4	0.3	1.0	0.6
10. S America	0.4	1.0	1.0	1.3	3.7	3.2
11. SAm Transport	0.2	0.5	0.8	0.3	NS	0.8
12. Central Africa	0.1	0.2	0.3	0.4	NS	1.2
13. Sthrn Africa	0.1	0.3	0.5	0.3	NS	0.7
14. SAf Transport	0.1	NS	0.4	NS	NS	NS
15. Maritime SEA	0.4	1.0	1.3	1.0	2.3	3.4
16. NW Australia	0.3	0.7	0.7	0.4	NS	1.1
17. E Australia	0.2	0.4	0.6	0.4	1.1	1.0
Background						
18. NH (0 to 60)	0.2	0.3	0.5	Inconclusive due to land/ocean and mix of regions		
19. SH (-60 to 0)	0.2	0.4	0.5			

1495 *Cardinal directions are abbreviated (e.g. Northeast = NE), SAm = South America, SAf = Southern Africa,
 1496 NS = Autocorrelation is not significant for p=0.01
 1497

1498

1499 A4 Summary of uncertainties 2002-2008

1500 A comparison between uncertainties and the WLS standard error for 2002-2018 trends is shown
 1501 in Table A4.1. Systematic uncertainties are described in one direction and random uncertainty is

1502 bi-directional. The uncertainties reported here are of opposite sign to the slopes calculated in
1503 Appendix A1.1 and A2. Although in some cases uncertainties are determined significant relative
1504 to their respective standard errors, all uncertainties are small compared to the standard error in
1505 the slope from the main text. Overall, the impact of these uncertainties on the trends found in the
1506 main text does not alter our main findings and conclusions.

1507

1508

1509 Table A4.1: Summary of uncertainties in the 2002-2018 trend analysis compared with WLS
 1510 standard error in the slope. All values are shown in percent per year. Green backgrounds are
 1511 significant.

	Sampling uncertainty		MOPITT sensitivity (systematic)	Std err from WLS	Approximated Std err with autocorrelation
	systematic	random			
Industrial					
1. NE China	-0.031	±0.005	-0.145	±0.3	±0.1
2. N India	+0.02	±0.003	-0.04	±0.2	±0.1
3. Europe	+0.001	±0.003	+0.047	±0.1	±0.1
4. E USA	-0.0003	±0.004	+0.032	±0.1	±0.1
Fire-prone					
5. NW USA	-0.001	±0.004	+0.079	±0.2	±0.1
6. NW Canada	+0.0028	±0.004	+0.0403	±0.1	±0.1
7. Siberia	+0.012	±0.006	+0.007	±0.1	±0.2
8. Russia	+0.012	±0.001	+0.065	±0.1	±0.1
9. Cent. America	-0.005	±0.001	-0.018	±0.1	±0.1
10. S America	-0.02	±0.002	-0.05	±0.2	±0.3
11. SAm Tspt BB	-0.001	±0.002	+0.013	±0.2	±0.2
12. Central Africa	+0.016	±0.001	-0.013	±0.2	±0.1
13. Southern Africa	-0.002	±0.002	+0.04	±0.3	±0.1
14. SAf Tspt	+0.01	±0.002	+0.008	±0.2	±0.1
15. Maritime SEA	-0.02	±0.003	-0.135	±0.2	±0.4
16. NW Australia	-0.011	±0.001	-0.004	±0.1	±0.3
17. E Australia	-0.006	±0.001	+0.001	±0.2	±0.2
Background					
18. NH (0 to 60)	+0.001	±0.0004	+0.01	±0.3	±0.2
19. SH (-60 to 0)	-0.001	±0.0005	+0.01	±0.3	±0.2

1512

1513

1514 **Appendix B. Other impacts on trend analysis**

1515 We investigate the robustness of trend analysis to using different methods, accounting for the
1516 seasonal cycle in different ways, using different trend methodologies, as well as the impact of
1517 outliers.

1518 **B1 Selection of trend analysis methodology**

1519 Noise is anything that deviates the data from the model (the linear trend), and consequently
1520 increases uncertainty in trend analysis. The seasonal cycle in CO data therefore adds noise to the
1521 trend analysis. There are several methods one can use to remove the impact of seasonality on
1522 trend analysis. We investigate four methods of accounting for seasonality.

1523 Method 1: use year average values in trend calculations.

1524 Method 2: calculate the 12-month moving average. Because seasonality occurs during a
1525 12-month period, any shorter or longer time period (not divisible by 12) would introduce
1526 some seasonal information.

1527 Method 3: subtract the whole dataset month average values.

1528 Method 4: remove the seasonal cycle using a harmonic fit.

1529 We also assess the use of Theil-Sen on year-average values. The Theil-Sen method is robust to
1530 outliers, but is sensitive to cyclic data, therefore we use yearly averages of the monthly anomaly
1531 data.

1532

1533 All methods calculate consistent trend signs and magnitudes within one standard error, apart
1534 from the WLS on running averages for South America. Regions that show difficulty for
1535 interpreting significant trends (Southern Africa) are also generally consistent. In the main text,
1536 we choose to use method 2 before applying WLS. Retaining month anomaly values helps to

1537 assess the monthly contributions to interannual variability (e.g. Fig. 3c and 3d).

1538

1539 Table B1.1: Summary of weighted least-squares different methods of accounting for seasonality.

1540 Theil Sen trends are also shown for the full time series. Blue backgrounds denote negative trends

1541 and yellow background denote no trend for WLS analysis. Orange background indicates $p > 0.05$

1542 for Theil-Sen (non-significant).

	Theil-Sen (p) on year average	Method 1: WLS Trend on year average (\pm standard error)	Method 2: WLS Trend on Runave	Method 3: WLS Trend on Anomaly (using mean annual cycle)	Method 4: WLS Trend on Anomaly (using harmonics)
	2002-2018	Full July 2002- June 2018: % per year (\pm standard error)			
Industrial					
1. NE China	-1.20 (2.2e-05)	-1.16 (0.3)	-1.22 (0.3)	-1.18 (0.3)	-1.18 (0.3)
2. N India	-0.19 (0.036)	-0.27 (0.1)	-0.26 (0.2)	-0.28 (0.2)	-0.28 (0.2)
3. Europe	-0.77 (3.2e-05)	-0.79 (0.2)	-0.78 (0.1)	-0.89 (0.1)	-0.88 (0.1)
4. E USA	-0.78 (1.5e-05)	-0.79 (0.2)	-0.84 (0.1)	-0.85 (0.1)	-0.84 (0.1)
Fire-prone					
5. NW USA	-0.71 (3.4e-04)	-0.80 (0.2)	-0.74 (0.2)	-0.85 (0.2)	-0.83 (0.2)
6. NW Canada	-0.59 (4.6e-04)	-0.58 (0.2)	-0.63 (0.1)	-0.60 (0.1)	-0.59 (0.1)
7. Siberia	-0.67 (1.5e-03)	-0.57 (0.2)	-0.61 (0.1)	-0.59 (0.1)	-0.58 (0.1)
8. Russia	-0.72 (1.0e-05)	-0.77 (0.2)	-0.77 (0.1)	-0.80 (0.1)	-0.79 (0.1)
9. Cent. America	-0.49 (2.0e-03)	-0.52 (0.2)	-0.48 (0.1)	-0.46 (0.1)	-0.46 (0.1)
10. S America	-0.70 (0.053)	-0.53 (0.4)	-0.70 (0.2) *	-0.31 (0.2)	-0.30 (0.2)
11. SAm Tspt BB	-0.64 (5.8e-03)	-0.53 (0.2)	-0.55 (0.2)	-0.39 (0.2)	-0.38 (0.2)
12. Central Africa	-0.23 (0.015)	-0.25 (0.1)	-0.23 (0.2)	-0.22 (0.2)	-0.22 (0.2)
13. Southern Africa	-0.26 (0.11)	-0.21 (0.2)	-0.20 (0.3)	-0.17 (0.3)	-0.17 (0.3)
14. SAf Tspt	-0.04 (0.90)	-0.08 (0.2)	0.04 (0.2)	-0.07 (0.2)	-0.07 (0.2)
15. Maritime SEA	-0.69 (0.029)	-0.71 (0.3)	-0.54 (0.2)	-0.51 (0.2)	-0.50 (0.2)
16. NW Australia	-0.49 (0.053)	-0.32 (0.3)	-0.37 (0.1)	-0.25 (0.1)	-0.25 (0.1)
17. E Australia	-0.44 (0.015)	-0.45 (0.2)	-0.42 (0.2)	-0.32 (0.2)	-0.32 (0.2)
Background					
18. NH (0 to 60)	-0.57 (4.6e-04)	-0.59 (0.1)	-0.54 (0.3)	-0.57 (0.3)	-0.56 (0.3)
19. SH (-60 to 0)	-0.47 (7.4e-03)	-0.47 (0.1)	-0.39 (0.3)	-0.35 (0.3)	-0.35 (0.3)

1543 *Significantly different trend result outside 1σ

1544

1545

1546 **B2 Impact of outliers on trend analysis**

1547 WLS trend analysis is less impacted by outliers than ordinary least squares because variability
1548 associated with outliers de-weights the outlier contribution to trend analysis. However, we wish
1549 to quantify the impact of the large El Niño in 2015 on trend analysis. Figures 3c and 3d show the
1550 hemispheric impact of the 2015 fires in Maritime SEA. The large contribution to atmospheric
1551 CO loading from this event remained in the atmosphere for over 2 months (Field et al., 2016).
1552 Resulting high values could have skewed our results towards less negative trends. Consequently,
1553 we investigate the impact of removing X_{CO} data from July 2015 to June 2016, and recalculate
1554 trends. The comparison between trends calculated with and without Maritime SEA fire influence
1555 in 2015 is shown in Table B2.1.

1556

1557 When removing the MSEA event from analysis, trends become consistently more negative. The
1558 shorter period experiences more impact on trends than the longer period. Largest differences are
1559 seen around the SH fire-prone regions. However, most of the trends are not significantly different
1560 from what was calculated in the main text, relative to one standard error. Furthermore, trend
1561 changes do not alter our conclusions from the main text. We still find the slowdown in the CO
1562 trend such that the earlier record has a stronger trend than either the later record or long-term
1563 record.

1564

1565 We were also interested in the large dip in 2008-2009 that might particularly influence the trends
1566 in our early sub-time period (Fig. 3c), so we removed February 2008 to January 2010 and
1567 recalculated trends (not shown). While we found some substantial differences in trend
1568 magnitudes for some regions, the overall message remained that the earlier period experienced
1569 more negative trends in CO compared to the later period or the whole time period.

1570

1571 Table B2.1: Summary of WLS trends in the anomaly X_{CO} from the 19 regions with standard
 1572 error, shown for different time periods. The original record values are the same as found in Table
 1573 2. Trends without 201507-201606 removes the extended influence from the large fires in
 1574 Maritime SEA during the burning season of 2015. Green background colors indicate differences
 1575 outside one standard error.

WLS Trend on Runave % per year (+/- standard error)					
		Original	Without 201507-201606	Original	Without 201507-201606
		Full July 2002-June 2018		2nd half July 2010-June 2018	
Industrial					
1.	NE China	-1.18 (0.3)	-1.26 (0.3)	-1.02 (0.7)	-1.14 (0.7)
2.	N India	-0.28 (0.2)	-0.34 (0.2)	-0.17 (0.5)	-0.29 (0.5)
3.	Europe	-0.89 (0.1)	-1.00 (0.1)	-0.47 (0.3)	-0.67 (0.3)
4.	E USA	-0.85 (0.1)	-0.98 (0.1)	-0.73 (0.3)	-0.95 (0.3)
Fire-prone					
5.	NW USA	-0.85 (0.2)	-0.95 (0.2)	-0.67 (0.4)	-0.85 (0.4)
6.	NW Canada	-0.60 (0.1)	-0.67 (0.1)	-0.51 (0.3)	-0.64 (0.3)
7.	Siberia	-0.59 (0.1)	-0.64 (0.1)	-0.32 (0.4)	-0.40 (0.4)
8.	Russia	-0.80 (0.1)	-0.88 (0.1)	-0.66 (0.3)	-0.81 (0.3)
9.	Cent. America	-0.46 (0.1)	-0.58 (0.1)	-0.23 (0.4)	-0.46 (0.4)
10.	S America	-0.31 (0.2)	-0.40 (0.2)	0.02 (0.6)	-0.16 (0.6)
11.	SAm Tspt BB	-0.39 (0.2)	-0.48 (0.2)	-0.03 (0.5)	-0.24 (0.5)
12.	Central Africa	-0.22 (0.2)	-0.27 (0.2)	-0.12 (0.5)	-0.21 (0.5)
13.	Southern Africa	-0.17 (0.3)	-0.29 (0.3)	-0.09 (0.7)	-0.34 (0.7)
14.	SAf Tspt	-0.07 (0.2)	-0.18 (0.2)	0.14 (0.6)	-0.08 (0.6)
15.	Maritime SEA	-0.51 (0.2)	-0.63 (0.2)	-0.14 (0.5)	-0.34 (0.5)
16.	NW Australia	-0.25 (0.1)	-0.34 (0.1)	0.03 (0.4)	-0.15 (0.4)
17.	E Australia	-0.32 (0.2)	-0.42 (0.2)	0.16 (0.5)	-0.01 (0.5)
Background					
18.	NH (0 to 60)	-0.57 (0.3)	-0.67 (0.3)	-0.43 (0.8)	-0.63 (0.8)
19.	SH (-60 to 0)	-0.35 (0.3)	-0.46 (0.4)	-0.1 (1)	-0.3 (1)

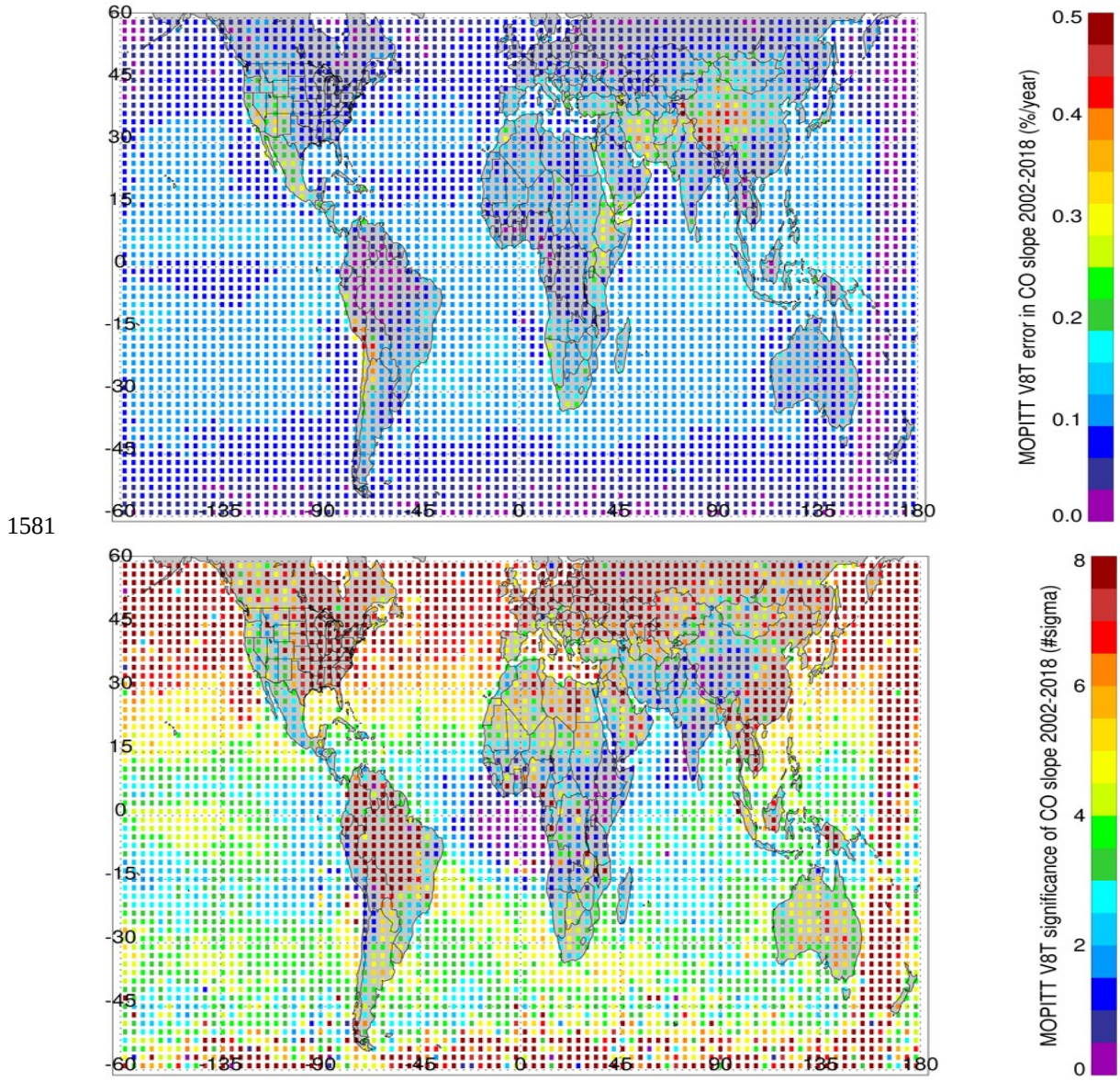
1576

1577

1578

1579 **Supplementary Material**

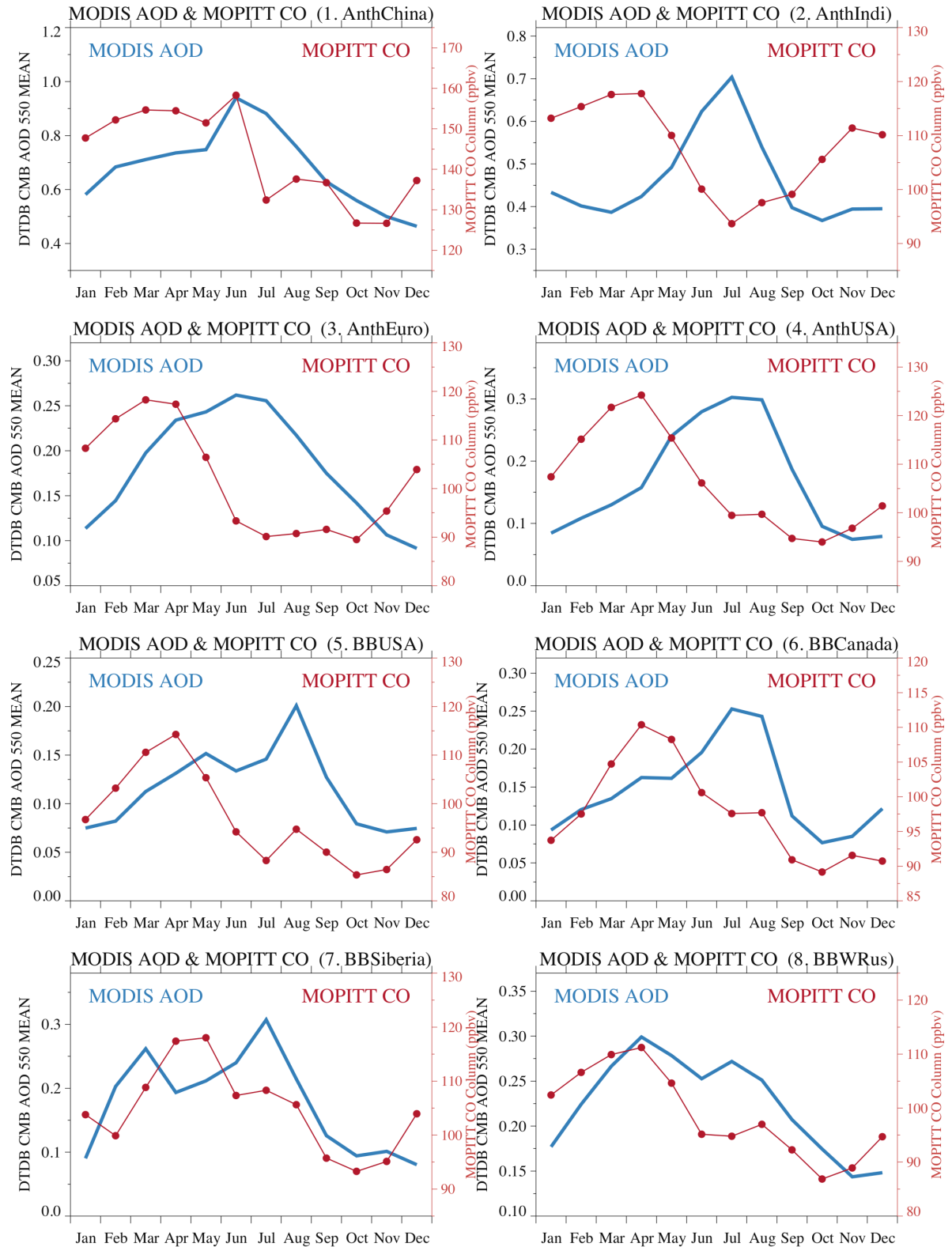
1580

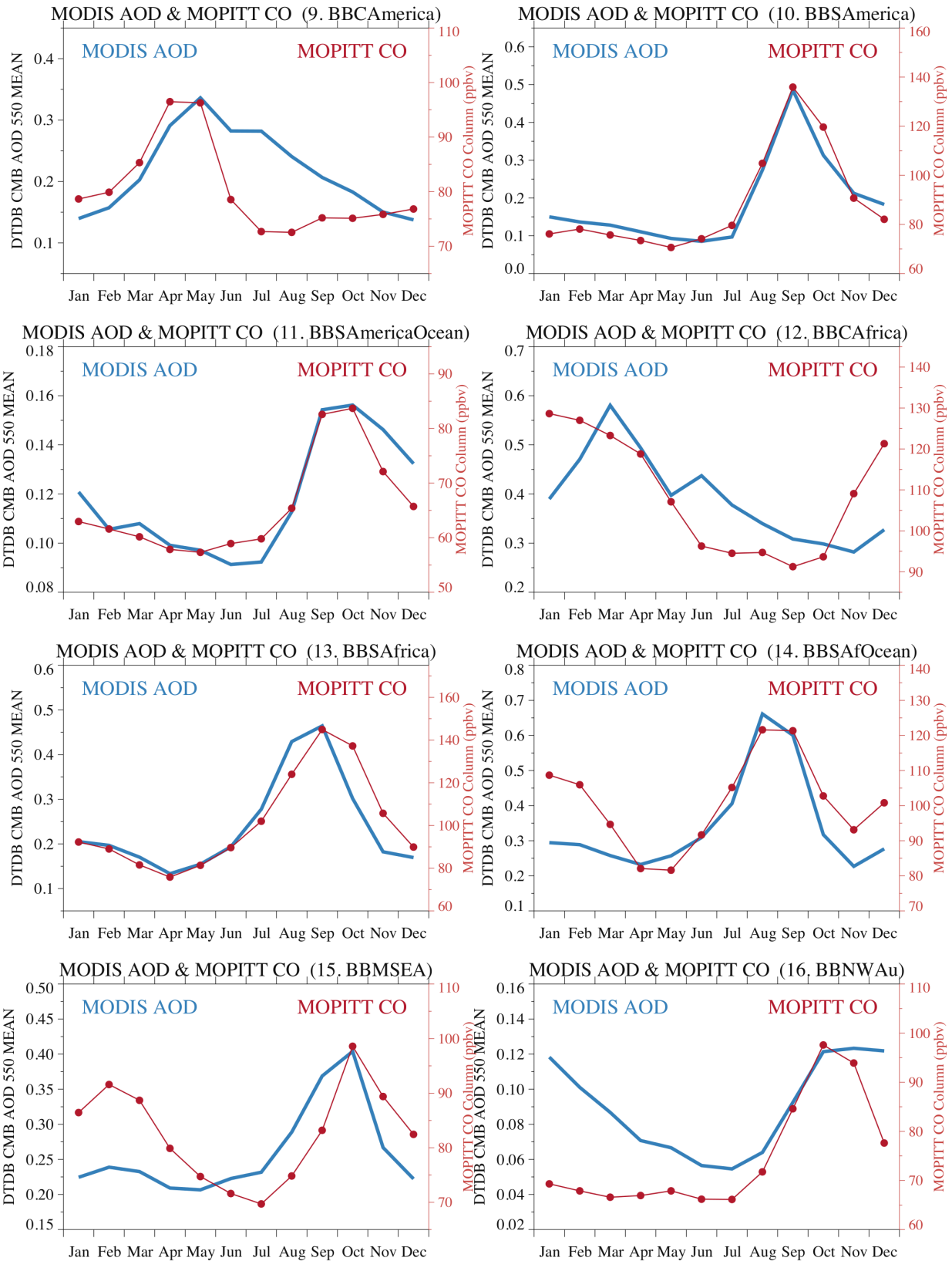


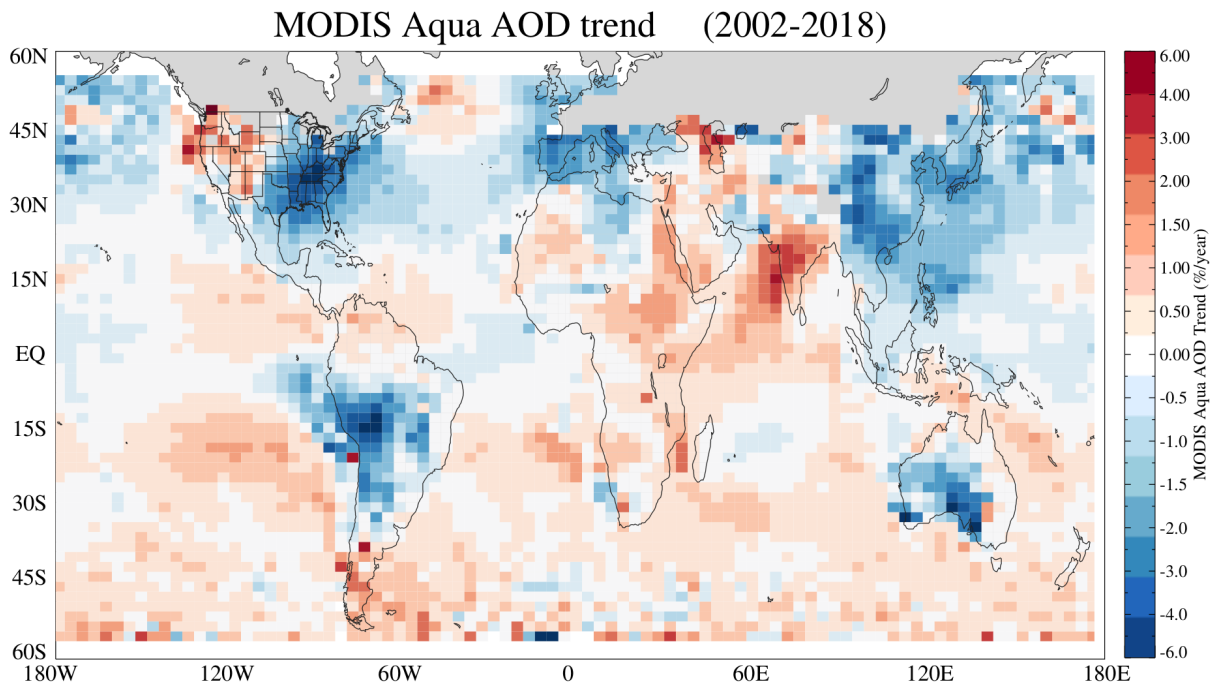
1581

1582

1583 Fig C1: Trend standard error (top) and significance - calculated trend relative to std err (bottom).







1586

1587 Fig C2: Trends in AOD from Aqua/MODIS between 2002 and 2018, gridded to 2°x4°.

1588

1589

1590

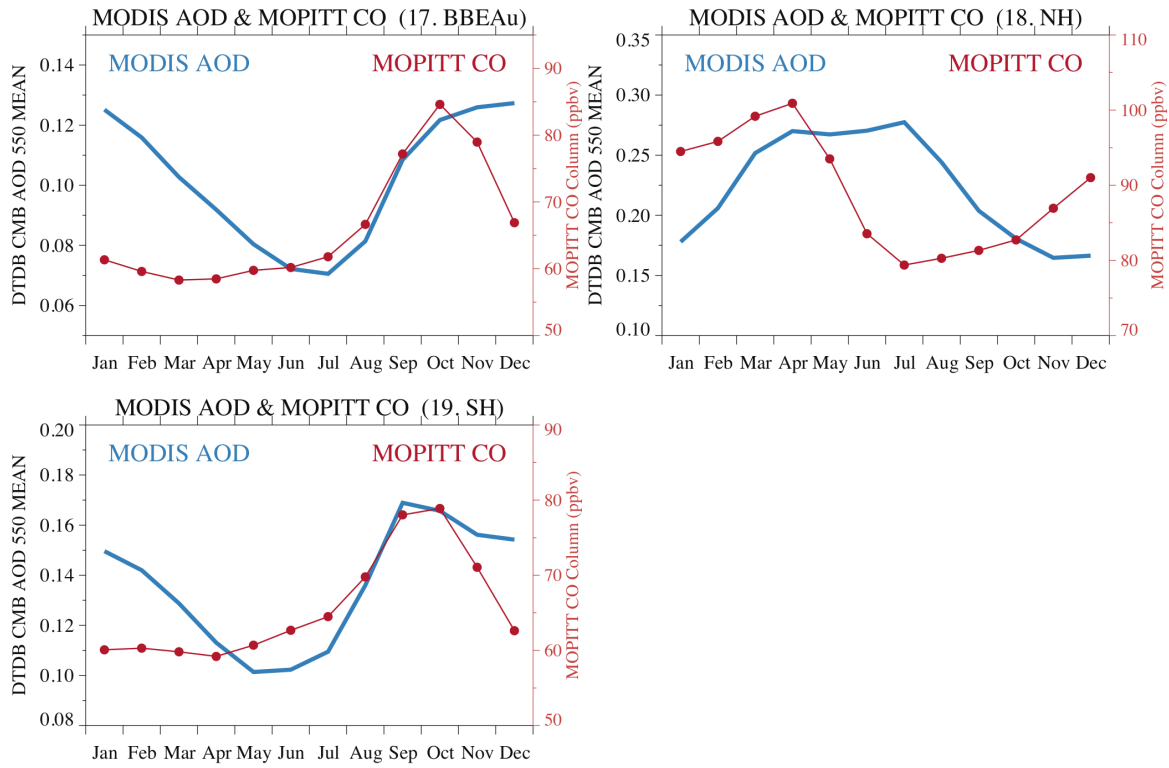
1591

1592

1593

1594

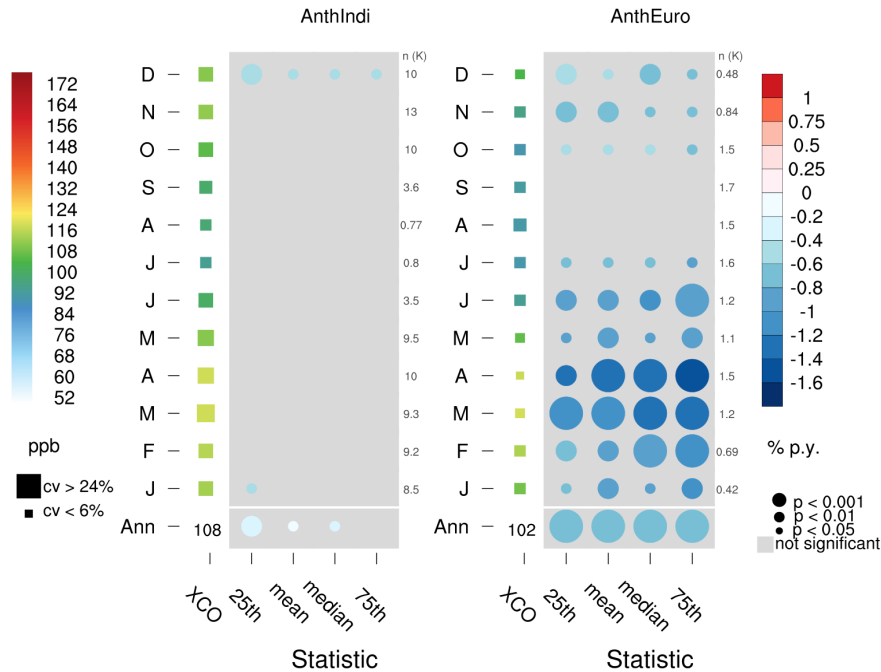
1595



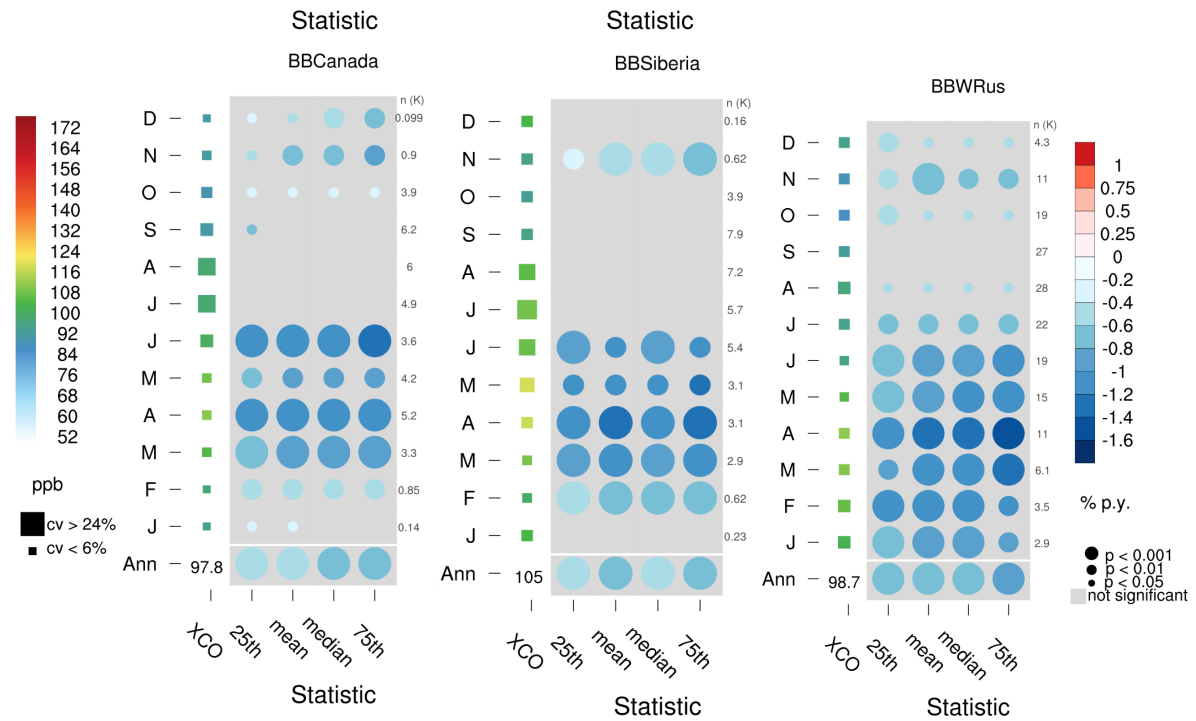
1596 Fig C3: Dataset average annual cycles in month average X_{CO} (red) and AOD (blue) for the
 1597 different regions. Region numbers correspond with regions in Fig. 2 and names in Table 2.

1598

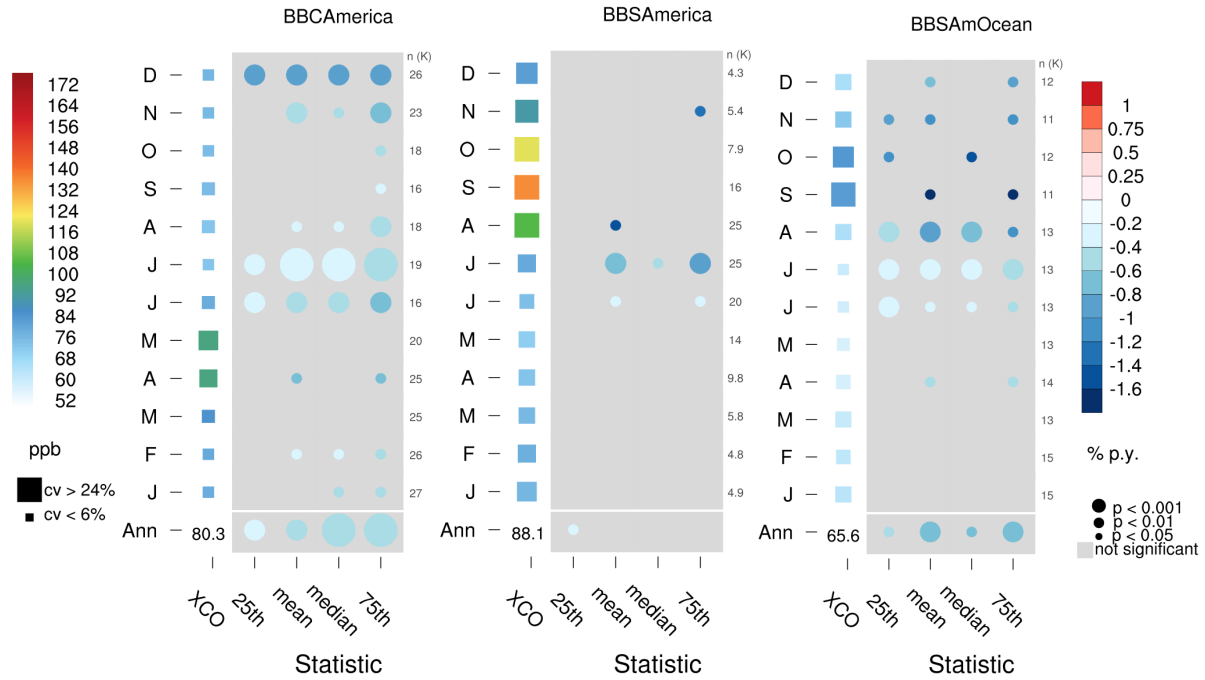
1599



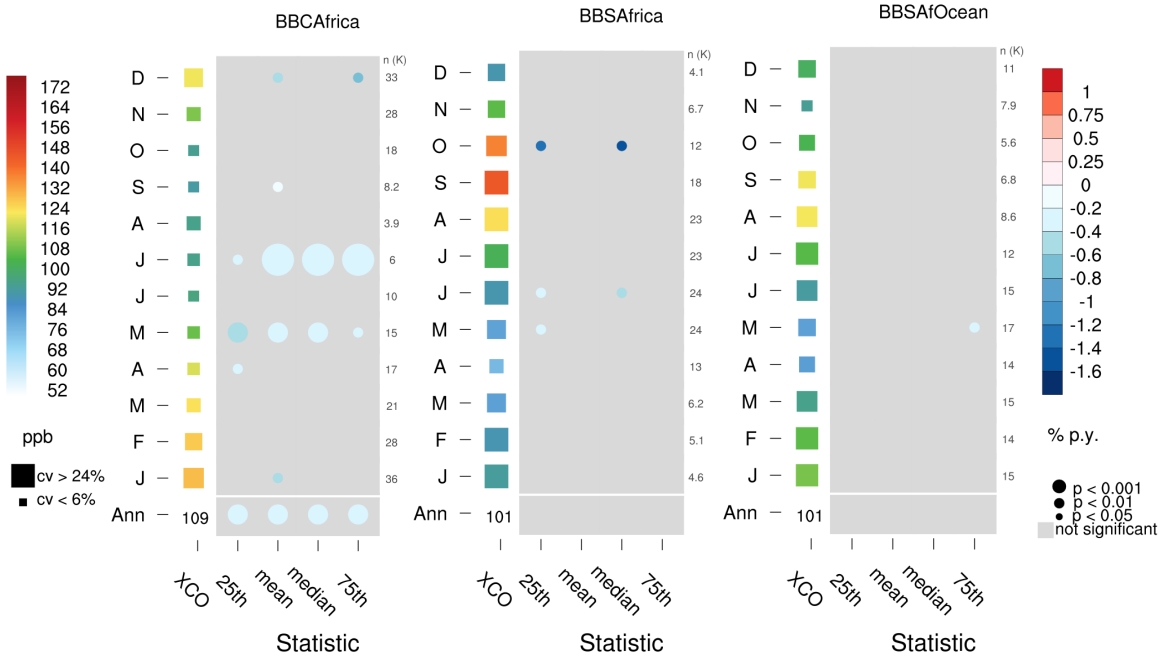
1600



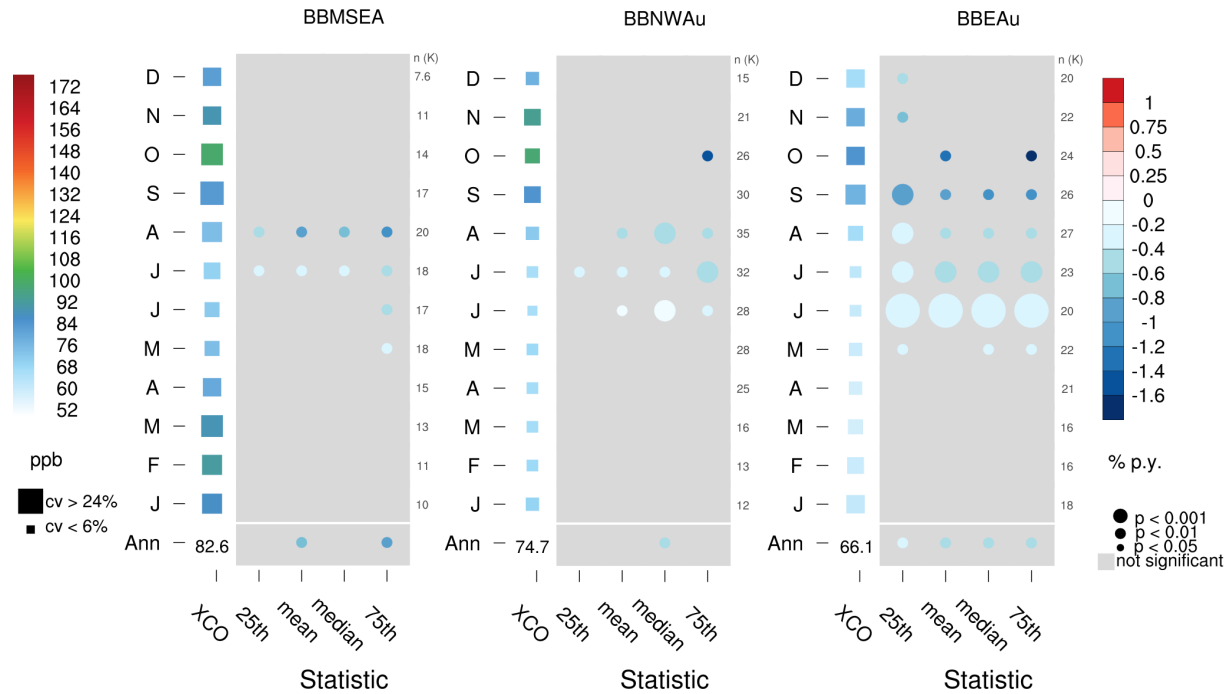
1601



1602



1603



1604
1605

1606 Fig C4: Gridded arrays of quantile trend analysis for monthly data for different regions. Trends
 1607 are shown as circles colored by percent per year, which is calculated relative to the regional
 1608 mean column average VMR. The Mann-Kendall p-value is indicated by the size of the circle.
 1609 Trends in annual mean values are shown for comparison in the bottom row. Month average
 1610 column average VMR along with the coefficient of variation are displayed as colored squares on
 1611 the LHS. The mean number of retrievals (n) within a month are displayed on the RHS, in
 1612 amounts of thousands (K).